

Coniferous needle-leaves, shoots and canopies: a remote sensing approach

Lucía Yáñez Rausell

Thesis committee

Promotor

Prof. Dr sc. nat. M.E. Schaepman
Professor of Remote Sensing, University of Zurich, Switzerland
Professor of Geo-information Science and Remote Sensing
Wageningen University

Co-promotors

Dr Z. Malenovský
Research Associate, School of Biological Sciences
University of Wollongong, Australia
Adjunct Researcher, School of Land and Food
University of Tasmania, Australia

Dr J.G.P.W. Clevers
Associate Professor, Laboratory of Geo-information Science and Remote Sensing
Wageningen University

Other members

Prof. Dr P. Struik, Wageningen University
Prof. Dr M. Krol, Wageningen University
Prof. Dr W. Verhoef, University of Twente, The Netherlands
Dr J.Verrelst, University of Valencia, Spain

This research was conducted under the auspices of the C.T. de Wit Graduate School
of Production Ecology & Resource Conservation (PE&RC)

Coniferous needle-leaves, shoots and canopies: a remote sensing approach

Lucía Yáñez Rausell

Thesis

submitted in fulfilment of the requirements for the degree of doctor
at Wageningen University
by the authority of the Rector Magnificus
Prof. Dr M.J. Kropff,
in the presence of the
Thesis Committee appointed by the Academic Board
to be defended in public
on Wednesday 14 May 2014
at 11 a.m. in the Aula.

Lucía Yáñez Rausell
Coniferous needle-leaves, shoots and canopies: a remote sensing approach
154 pages

PhD thesis, Wageningen University, Wageningen, NL (2014)
With references, with summaries in Dutch, English and Spanish

ISBN 978-94-6173-868-4

Table of contents

	Page	
Chapter 1	Introduction	1
Chapter 2	Minimizing measurement uncertainties of coniferous needle-leaf optical properties, part I: methodological review	19
Chapter 3	Minimizing measurement uncertainties of coniferous needle-leaf optical properties, part II: experimental set-up and error analysis	33
Chapter 4	A note on upscaling coniferous needle spectra to shoot spectral albedo	71
Chapter 5	Estimation of spruce needle-leaf chlorophyll content based on DART and PARAS canopy reflectance models	87
Chapter 6	Synthesis	115
	References	131
	Summary / Samenvatting / Resumen	139
	Acknowledgements	148
	List of publications	150
	Short biography	152
	Education certificate	153

Chapter 1

Introduction

1.1 Coniferous forests dynamics and optical remote sensing

Forest ecosystems represent ~30% of the global land surface (Sabine 2004) and they have a recognized importance in the regulation of Earth's climate through interaction processes with the atmosphere such as energy and water exchange and carbon storage (Bonan 2008). Coniferous forests, spread over the boreal and temperate domains, represent ~43% of the global forest extension (Hansen et al. 2010). Due to climate change and rising human pressure on these ecosystems, currently several key parameters that control forest dynamics are changing and they are expected to continue changing in the coming years (IPCC 2007). Recent studies on forest cover loss showed that from 2000-2012 a total of 2.3 million km² of forest were lost due to disturbance, mainly in the tropical and boreal climatic domains (Hansen et al. 2013). This has implications for the carbon storage, water balance, species composition, phenology, productivity, location, pests and fire dynamics of forests (FAO 2010). In order to better understand and forecast potential responses to these changes, continuous monitoring and modelling of forest ecosystem processes is crucial. In this respect, optical remote sensing (RS) provides powerful methods for the estimation of essential climate variables (ECV's) (Claverie et al. 2013; Main-Knorn et al. 2013; Wright et al. 2014) in support of the work of the United Nations Framework Convention on Climate Change (UNFCCC) and the Intergovernmental Panel on Climate Change (IPCC).

Amongst the advantages of RS are its applications for a broad range of terrain conditions including areas of difficult access (e.g., remote boreal or alpine forests) and the broad range of temporal and spatial resolutions when compared with conventional field-based techniques (Hansen et al. 2008; Sexton et al. 2013). RS is a unique method for repetitive observations at global scale (Baret et al. 2013; Myneni et al. 2002; Zhu et al. 2013) and a cost-effective and suitable technology for global forest monitoring (Hansen et al. 2013; Hansen et al. 2010). Nevertheless, proper interpretation of the RS data requires precise understanding of the underlying mechanisms generating the RS signal (Knyazikhin et al. 2013). In this regard, coniferous forests represent challenging targets for RS methods, mainly due to coniferous-specific structural features (e.g. narrow needle leaves, shoot clumping) whose effect on the RS signal is recognized (Rochdi et al. 2006; Smolander and Stenberg 2003) yet not completely understood (see for example the review on

this topic from Stenberg et al. (2008)). Given the ecological importance of coniferous forest ecosystems (Bonan 2008) and the unique potential that RS offers for its global monitoring (Hansen et al. 2013), improvement on the RS-based methods applied to coniferous forests is necessary. This thesis contributes to improving the interpretation of the remotely sensed optical signal reflected from coniferous canopies by focusing on specific gaps identified in the RS methods at different scales of the coniferous canopies. In this chapter we introduce how the solar radiation interacts with the forest canopy and its elements shaping the remotely sensed optical signal. The most common approaches used to mathematically describe the photon transfer through the canopy are then presented. Next, we give a general overview of specific features governing the radiation budget in coniferous forest stands. Subsequently, we introduce a specific approach whose formulation is based on those mechanisms of light-canopy interactions (Myneni and Ross 1991). Finally, we present the objectives and research questions addressed in this thesis.

1.2 Light-forest canopy interactions

Regulation of Earth's climate by forest ecosystems is done through biogeochemical processes such as carbon storage and biophysical processes such as water, energy, and momentum exchange with the atmosphere (Bonan 2008). Among these complex forest-atmosphere interactions, the amount of solar radiation absorbed at the Earth's surface and represented by the surface albedo (Schaepman-Strub et al. 2006) is a key parameter to understand climate services of forests (Bonan 2008). In forested areas surface energy fluxes are mainly driven by the chemical and structural properties of the forest canopy (i.e. optically active surfaces such as the foliage, branches, trunks, etc.) and understory vegetation (Myneni et al. 1995). These properties determine how incoming solar radiation is absorbed or scattered within the canopy and therefore define the spectral and angular characteristics of the radiation being reflected back to the atmosphere. Optical sensors (e.g. on an airborne platform or satellite) record this reflected radiation, usually between 400 and 2400 nm of the electromagnetic spectrum, providing valuable quantitative information related to the Earth's energy fluxes. The principle behind optical RS is to provide a link between this reflected signal and the specific chemical and structural properties of the forest canopy that have contributed to the processes shaping the signal. These properties are represented by vegetation

parameters such as leaf area index, chlorophyll or water content, which are used as indicators of the mentioned energy processes. For example, foliar chlorophyll molecules are known to absorb solar radiation in the blue and red part of the electromagnetic spectrum (Chen et al. 2010). This phenomenon results in spectral absorption features of the forest reflectance function that can be exploited by RS methods to detect and quantify the leaf chlorophyll *a* and *b* content (*C_{ab}*) (e.g. Blackburn (2007)). However, an increase in the concentration of foliar absorbing constituents does not necessarily imply a decrease of the reflected signal (due to an increase of the absorption) since other simultaneous processes driven by other factors, e.g. scattering driven by canopy structure, can dominate the spectral signal and mask the mentioned absorption features (Knyazikhin et al. 2013).

Thus, a proper translation of the RS measured spectral signal into the parameters of interest (in this case *C_{ab}*) relies on the understanding and definition of the absorption, transmission and reflectance processes and related scattering processes in atmosphere and canopy in order to separate their mixed effects (Knyazikhin et al. 2013).

1.3 Modelling interactions of light within the forest canopy

Three main approaches are used in RS to model the interactions of solar radiation with the forest canopy: 1) empirical, 2) physically-based, and 3) hybrid. These modelling approaches are the basis either for predicting the measured RS optical signal based on a specific set of canopy parameters, i.e. the forward problem (Liang 2004), or for estimating canopy parameters from the signal observed in a given configuration, i.e. the inverse problem (Liang 2004). In the latter case, the parameter of interest being estimated is normally referred to as variable.

In the empirical approach the link between parameters and RS signal is based on statistical models calibrated over empirical spectral data. Models are computationally fast, but dependent on specific site and acquisition conditions. Most widely used empirical models are the vegetation indices where individual spectral bands are combined to enhance sensitivity to a specific canopy characteristic (Gamon et al. 1992; Haboudane et al. 2002; Zarco-Tejada et al. 2013).

Physical approaches are based on physical laws governing the light-canopy processes of absorption and scattering. They are not site- or acquisition conditions specific, and therefore they are considered more robust and

adaptable than the empirical ones. The interaction of solar radiation with the canopy is described by means of the radiative transfer (RT) equation (Myneni and Ross 1991), which is mathematically implemented in canopy reflectance models, also known as RT models. These models simulate the bi-directional reflectance factor (BRF) or the albedo of the canopy (Schaepman-Strub et al. 2006) based on physical parameters; however, they differ in the way these parameters are defined. For example, the canopy description can be based on a horizontally homogeneous and infinite medium with random canopy elements (turbid models), on the combination of basic geometric shapes (geometric-optical models), on the mix of both (hybrid models) or on a 3-dimensional representation where a detailed simulation of the trajectory and interactions of photons is performed (ray-tracing models) (Goel 1988). Depending on the level of detail their parameterization can be highly complex requiring many inputs and power-intensive computations. In addition, the ill-posed problem during inversion (Baret and Buis 2008; Combal et al. 2003), i.e. yielding a non-unique solution, is another disadvantage of these models.

Finally, the hybrid approach consists of any sort of combination of the previous ones. Hybrid approaches generally combine the advantages of both previous approaches offering a good trade-off between realism and need of simplification (Pinty and Verstraete 1992), representing a suitable option for complex heterogeneous canopies such as the coniferous stands. Common examples applied in such canopies are the RT hybrid models, e.g. turbid medium and geometric-optical models (Laurent et al. 2011b), the use of empirical relationships implemented within physically-based forward modelling (Smolander and Stenberg 2003, 2005), or the use of forward RT modelling combined with an inversion based on artificial neural networks (Malenovský et al. 2013) or an empirical inversion model (Hernández-Clemente et al. 2012). Hybrid models were therefore used throughout this thesis.

Models designed to be applied at scales smaller than the canopy also exist, e.g. leaf-level empirically- (Cheng et al. 2011; Colombo et al. 2008) or physically-based models (Baranoski 2006; Jacquemoud and Baret 1990); or (coniferous) shoot-level empirical (Mottus and Rautiainen 2013) or physically-based ones (Rochdi et al. 2006). At these smaller scales not only the influence of confounding factors like the complex canopy structure is considerably reduced but also the overall number of parameters influencing the signal is smaller. Thus, in most cases these models have better prediction capabilities than canopy ones, specially leaf models (Demarez and Gastellu-

Etchegorry 2000) and therefore they are commonly used coupled to canopy models. The coupling of RT models at different levels is a common strategy used to alleviate the under-determination faced during the inversion of canopy RT models. This under-determination is caused by the limited information content of the radiometric signal when compared to the high number of unknowns (both variables and parameters) influencing the canopy reflectance. For example, introducing the spectral properties of the leaf into a canopy model represents a large number of inputs, i.e. leaf reflectance and transmittance for each wavelength. Using a leaf RT model having only a few input parameters instead, e.g. the PROSPECT model (Jacquemoud and Baret 1990), reduces the number of free variables during model inversion (Baret and Buis 2008). This lowers the risk of under-determined inversion problems because the number of estimated variables is closer to the dimensionality of the data (Laurent et al. 2011b).

Additionally, other methods such as spectral transformations used to eliminate effects of other variables and standardise real observations (i.e. remove noise and unwanted residual effects of data calibration processes) are also applied, e.g. derivatives (Clevers et al. 2008), wavelet decomposition (Banskota et al. 2013; Huang and Blackburn 2011) or continuum removal (Malenovský et al. 2013).

1.3.1 Canopy radiative transfer

A numerical solution of the RT equations requires parameterization of the composition and optical properties of the media in question (Myneni et al. 1995), i.e. a description of:

- (i) the canopy structure, i.e. the spatial distribution of scattering elements and gaps influencing the extinction (interaction) of radiation in the canopy,
- (ii) the canopy spectral and angular properties, and
- (iii) the boundary conditions.

1.3.1.1. Canopy structure

Definition of the canopy structure in the RT requires describing at least the leaf density and orientation (Baret and Buis 2008). Leaf density can be represented by the leaf area index (LAI), meaning the one-sided green leaf area per unit ground area (Watson 1947). Sometimes the branch area index (BAI), representing the non-foliar canopy elements, is also defined. In addition, a description of the aggregative nature of vegetation canopies that

produces foliar mutual shading and therefore leads to miscalculations in the radiation interception is recommended (Chen et al. 2012). This effect is especially important in coniferous forests, where foliage clumping appears at several canopy levels (see Section 1.4). It can be represented by the *clumping index* (Chen et al. 2005; Nilson 1971). The geometry factor called *G-function* (Ross 1981) explains the role of leaf orientation. This factor is defined as the mean projection of unit foliage area (projected on the horizontal or on a plane perpendicular to the direct light beam) and describes the efficiency of light interception by a canopy. It is normally computed by integrating the leaf angle distribution (LAD) over all directions (upper hemisphere), where the LAD represents the probability density of the distribution of the leaf normals (Liang 2004). Finally, the size of the leaves relative to canopy height is also required to define the canopy structure in the RT equation (Baret and Buis 2008).

1.3.1.2. Canopy spectral and angular properties

The spectral properties of the leaves (or other canopy elements) refer to their reflectance, transmittance and absorption, which vary depending on the wavelength. The angular properties describe the directionality of the radiation scattered, i.e., reflected and transmitted. The probability distribution of this scattered radiation is described by the element scattering phase function (Myneni et al. 1995).

In forest canopies the main absorbing elements are the leaves whose spectral properties are mainly determined by the leaf surface, the internal structure and the leaf biochemistry (and the leaf size - essentially thickness, for a given LAI). Leaf reflectance and transmittance are normally measured through integrating spheres (more precisely, the directional-hemispherical reflectance and transmittance factors, (Schaepman-Strub et al. 2006). The leaf scattering phase function is normally presented through simple models describing specular reflection at the leaf surface and diffuse scattering in the leaf interior (Marshak 1989).

The scattering properties of a canopy are anisotropic (i.e. they are non-Lambertian scatterers) and therefore the spectral and angular properties of the incoming solar radiation influence the canopy RT and have to be defined. For the same reason also sensor properties are required. An example of such anisotropy is the well-known hot spot effect (e.g., Nilson and Kuusk, 1989). The anisotropic reflectance properties of a canopy, including the dependency on the incoming radiation and sensor viewing angles, are mathematically described by the bidirectional reflectance distribution function (BRDF)

(Nicodemus 1965). Most canopy RT models simulate the canopy bidirectional reflectance factor (BRF), i.e. the scattered radiant flux represented by the canopy BRDF normalized to the radiant flux reflected into the identical beam geometry by an ideal (lossless) and diffuse (Lambertian) standard surface, irradiated under the same conditions (Schaeppman-Strub et al. 2006).

1.3.1.3. Boundary conditions

The boundary conditions refer to the above-, below- and beside-canopy environment, namely the atmosphere defining the incoming radiation at the top-of-canopy, the canopy background (soil, understory vegetation) and canopy surroundings contributing to the canopy signal, respectively (Myneni et al. 1995).

1.3.2 Field measurements for model calibration and validation

Modelling the forest canopy spectral signal (forward mode) and estimating canopy variables from RS data (inversion) involves calibration of the input parameters and the validation of the estimated output, respectively (Liang 2004). In both cases the use of field-measured datasets is required.

Before the model is fully developed, its testing requires a comprehensive dataset of reference field data in order to ensure a reliable approximation of reality and a proper performance. In addition, the use of *a priori* information based on field data is a way to reduce the variable space by avoiding unrealistic combinations of variables, which helps to limit the ill-posed problem of the inversion (Combal et al. 2003).

The acquisition of accurate field datasets is demanding in terms of time, cost and man-power (e.g. LOPEX campaign (Hosgood et al. 1995)). Thus, datasets of statistically representative and independent reference field data with known accuracy are in many cases unavailable. This lack has encouraged incorrect assumptions (e.g. for leaf angle distribution (Pisek et al. 2013)) or the use of inaccurate and/or obsolete archives (i.e. forest inventories, spectral datasets of common plant species) that may lead to significant errors in the interpretation of RS data and that constrain the use of the full potential of RS.

Coniferous species represent a good example of the mentioned problems regarding acquisition of accurate ground truth datasets. For example, empirical measurements, especially spectral, represent a technical challenge and a multidimensional problem (Mesarch et al. 1999; Möttus et al. 2012). Conventional devices for measuring leaf optical properties cannot be directly applied to coniferous needle leaves, due to their small size and narrow shape

(Daughtry et al. 1989; Mesarch et al. 1999). Despite the importance of accurate ground truth datasets, there is not a standard measuring technique adapted for coniferous needle leaves and only few studies so far attempted to investigate and quantify related measurement errors. Thus, acquisition of reliable and accurate leaf optical datasets for coniferous species is a gap for which further investigation is needed. In addition, other structural features that are characteristic of coniferous forests, such as the clumping of needles into shoots, are known to play a major role in canopy RT (Section 1.4). These features make coniferous stands a complex structural environment, and as such, the acquisition of spectral empirical data to support model development and RS interpretations are scarce, e.g. measurement of shoots scattering properties (Section 1.4.1.2). The main features characterising these issues and the implications on RT modelling are described in Section 1.4.

1.4 Specific features of coniferous forest canopies: needle-leaves and shoots

Coniferous canopies are known to differ from broadleaf forests by specific structural features that have a significant impact on the total canopy bidirectional reflectance factor (BRF), e.g. narrow tree crown shapes (Rautiainen et al. 2004). The most striking features are at the small-scale, namely, the narrow leaves (needles) and especially their clumping into shoots. Needles have different properties compared to flat broad leaves (inner and external structure) that affect the leaf BRF (Dawson et al. 1998). The needle clumping at the shoots produces mutual shading and the tendency to trap incoming photons (inside the shoots) triggering within (and between) shoot multiple scattering (Norman and Jarvis 1975) that increases the probability of photon absorption. In fact, multiple scattering at shoot level is claimed to be the driver that makes coniferous forests darker in the near infra-red region when compared with broadleaf stands (Rautiainen and Stenberg 2005). Thus, a proper mathematical description of the scattering properties of these structural units is crucial for the canopy RT definition (Rochdi et al. 2006; Smolander and Stenberg 2003). Yet, their impact on the canopy scattering is not fully understood and acquisition of supporting empirical data that might improve this knowledge is problematic (Section 1.3.4). The scattering processes derived from these specific features have not been properly implemented in the available RT models (Stenberg et al. 2008). In addition, concepts related to within-crown scales used in canopy RT formulations (i.e. structural and

spectral properties of leaves and leaf clumps) have originally been defined for flat broad-leaf species. Description of the required reformulation of such concepts for coniferous species is following (Section 1.4.1).

1.4.1 RT model reformulations required for coniferous canopies

1.4.1.1. Non-flat needle-leaves

Concerning the structural parameters, LAI was originally defined for leaves assumed to be flat (see Section 1.3.1.1). For non-flat leaves such as conifer needles, the counterpart to one-sided leaf area is the hemi-surface or half-of-total leaf (needle) area (Chen and Black 1992; Lang 1991). This includes the use of conversion factors to account for the non-flat needle cross-sections (see Homolová et al. (2013)).

Regarding leaf optical and angular properties, needles have varying geometrical cross-section shapes with several facets, they can be covered by wax, and their inner layers are forming a set of dense irregular spherical microstructures rather than the flat regularly layered structure of a typical bifacial broad leaf (Dawson et al. 1998). This influences both the specular reflection at the leaf surface and the diffuse scattering in the leaf interior and therefore affects the leaf scattering phase function and its modelling. An RT model specifically created for needle-leaves called LIBERTY (Dawson et al. 1998; Di Vittorio 2009) is available. However, it requires many inputs and does not necessarily perform better than non-needle specific leaf models (Moorthy et al. 2008) such as the extensively used PROSPECT leaf model (Jacquemoud and Baret 1990). In fact, the simplicity and robustness of PROSPECT has encouraged its use over the needle-specific model (Croft et al. 2013; Hernández-Clemente et al. 2012; Laurent et al. 2011a; Zarco-Tejada et al. 2004; Zhang et al. 2008a) and put forward alternative adaptations to coniferous needles (Malenovský et al. 2006a; Zhang et al. 2008b). Overall, one of the crucial problems related to the limited description of needle-leaf structural and spectral properties relates to the difficulty of acquiring empirical data. The small and narrow shape of needles represents a technical constraint to the available measuring devices such as integrating spheres (Mesarch et al. 1999) or leaf spectrogoniophotometers (Combes et al. 2007). The lack of empirical measurements has enforced modelling assumptions with a potentially negative impact on the interpretation of remote sensing data of coniferous forests, as for instance the needle reflectance being assumed to be equal to

the needle transmittance (Möttus 2007; Smolander and Stenberg 2003). Thus, improving monitoring of coniferous forests based on RS methods requires further investigation of this scientific gap related to the spectral measurements of coniferous leaves.

1.4.1.2. Shoots

The crucial problem derived from the clumped structure of the shoots is the mutual shading of the needles and its effect on both the structural and the optical parameters. The G-function (a geometry factor defining the leaf orientation relative to the incoming beam) was originally defined for flat leaves as the mean ratio of projected to one-sided leaf area (Nilson 1971), where 'projected leaf area' refers to the sum of the shadow areas cast by leaves on a plane perpendicular to the beam direction. For coniferous species, not only the mean projection of planar leaf area has to be derived considering needle shape (as explained), but also overlapping of needles in the shoot decreases the extinction coefficient, i.e. the interaction cross section area of the shoot is smaller than the one from all needles in the shoot (Stenberg 2006).

The suggested solution has been to use the shoot as the basic structural element, as it has long been done in models of canopy light interception and photosynthesis (Cescatti 1997; Nilson and Ross 1997; Oker-blom and Kellomaki 1983). In terms of RT modelling this involves: 1) describing the canopy structure based on the spatial and angular distribution of shoots, and 2) replacing the geometrical and spectral properties of leaves by those from shoots.

For the first part adaptations have been developed. To define shoot orientation, the same approach as defined for needles can be used (Stenberg 1996b). Also, a concept analogous to the G-function, but corrected for the needle mutual shading, was defined through the so-called STAR structural parameter (Oker-Blom and Smolander 1988). STAR is defined as the ratio of shoot silhouette (silhouette area averaged over all directions) to total needle area. Nevertheless, its definition requires extensive empirical measurements for the species-specific shoot silhouette calculations in all directions (Oker-Blom and Smolander 1988; Stenberg et al. 2001).

The major problem, however, is related to the geometrical and spectral properties of the shoot, since empirical measurements and models describing the scattering properties of shoots are very limited (Möttus et al. 2012; Nilson and Ross 1997; Rochdi et al. 2006; Ross et al. 1994; Smolander and Stenberg

2003). This lack of shoot spectral data is motivated by the complexity of the measurements (multidimensionality) and the technical limitations of currently available measuring devices (Möttus et al. 2012).

Despite the lack of a proper mathematical description of the shoots scattering properties, the canopy structural heterogeneity of coniferous forests could be characterized through a more realistic description of the macroscopic canopy structures, e.g. incorporating shoot models (Möttus et al. 2012; Rochdi et al. 2006; Smolander and Stenberg 2003) or building 3D forest scenes at a finer spatial resolution (Malenovský et al. 2013). Nevertheless, this increases the number of input parameters and/or the computational intensity required. Thus, accurate but simpler approaches to parameterize the structural complexity of coniferous forests while accounting for the shoot-level scattering processes would be highly useful to improve application of RS in such type of forests. One such approach is presented in Section 1.5.

1.5 Photon recollision probability theory applied in coniferous forests

An alternative to the complex description of the scattering properties of the within-crown foliage clumps in the RT has been introduced through the spectral invariants theory (Panferov et al. 2001). The theory states that the radiation budget in a canopy (bounded underneath by a black surface) can be parameterized using only spectrally invariant parameters that depend on canopy structure. The idea behind this is that while scattering and absorption processes are wavelength dependent, the probabilities of photons interacting with the canopy elements (leaves, branches, twigs, etc) are not, but they rather depend on the canopy structure given the large size of these elements compared to the wavelength of solar radiation. This way, the theory provides a link between the absorption and scattering properties at leaf and canopy levels through the definition of some key parameters representing the most essential structural features. Moreover, due to the scaling properties of the spectral invariants, this link can be applied to canopy hierarchical levels other than the leaf and canopy (e.g. leaf internals to leaf (Lewis and Disney 2007) or needle-leaves to shoots (Smolander and Stenberg 2003, 2005)).

One such spectral invariant structural parameter is the *recollision probability* or “p-parameter” defined as the probability that a photon scattered from a leaf in the canopy will interact within the canopy again

(Smolander and Stenberg 2003). Through p and the leaf scattering coefficient (ω_L) at a specific wavelength (λ) it is possible to determine the canopy absorption (α_c) and scattering (ω_c) at that wavelength (Huang et al. 2007; Knyazikhin et al. 2011). This link can be expressed through the following non-linear relationship:

$$\omega_c(\lambda) = \frac{\omega_L(\lambda) - p\omega_L(\lambda)}{1 - p\omega_L(\lambda)} \quad (1.1).$$

The p -parameter increases with increasing complexity of canopy architecture, which translates into a non-linear decrease of ω_c (Equation 1.1); therefore p is a measure of the canopy clumping. It is not a directly measurable parameter, but it can be related to (or derived from) available (measurable) canopy structural data. For example, if the relationship between p and LAI is known, the spectral signature of the canopy can be predicted in terms of LAI (Rautiainen et al. 2009; Stenberg et al. 2008), or the LAI estimated based on measured canopy reflectance (Heiskanen et al. 2011). At shoot level, a shoot adapted p -parameter, i.e. “recollision probability within a shoot” (p_{sh}), has also been defined in terms of the measurable structural parameter STAR (Smolander and Stenberg 2003). In fact, Smolander and Stenberg (2003, 2005) were the first to demonstrate theoretically the scaling properties of the p -parameter. They used p_{sh} in Equation 1.1 instead of the p -parameter and computed a shoot scattering coefficient ω_{sh} instead of canopy scattering ω_c . To support the theory, ray tracing simulations were performed for the model of shoot and canopy structure.

The p -theory still needs to be combined with other physically-based reflectance modelling concepts in RS applications. The reasons, as described by Stenberg et al. (2008), are: 1) it only describes canopy scattering, so a separate modelling of background reflectance is needed, and 2) it cannot describe the angular distribution of scattered radiation. A good example of such combination is found in the ‘family’ of PARAS models (Rautiainen and Stenberg 2005), which has already been applied in coniferous forest environments (Manninen and Stenberg 2009; Rautiainen et al. 2007; Stenberg et al. 2013). In general, these studies focused on studying structural properties of coniferous forests. Thus, further investigation on the potential of this approach for other applications, such as estimation of biochemical variables, is still missing.

1.6 Objectives and research questions

Despite the global ecological relevance of coniferous tree species, several unsolved knowledge gaps have been recognized in applications of RS methods to coniferous forest ecosystems. The main objective of this thesis is to bridge the scaling gaps in the interpretation of the remotely sensed optical signal reflected from spatially heterogeneous and structurally complex coniferous canopies. This thesis is addressing three main hierarchical structural levels of a coniferous forest stand in an attempt to resolve some of the problematic issues presented in the introduction: (i) individual needle leaves, (ii) shoots (i.e., needle clumps), and (iii) forest stand canopies.

The main focus at needle level is to improve knowledge about needle optical properties (OPs), which suffer from inconsistencies in spectral measurement techniques of narrow needle-shaped and non-flat (multi-faceted) leaves. Although OPs of coniferous leaves are extensively used in empirical and physical RS approaches (i.e. as inputs or as validation data), there is only a limited number of not fully standardized techniques available for measuring coniferous leaves. The first focus of this thesis is, therefore, to review the shortcomings and uncertainties of such methods in order to identify application limits and potential improvements. The need for a theoretical review of the measurement techniques resulted in the first research question investigated in this thesis (Question A).

The outcomes of the review opened a space for creation of a more standardized measuring protocol, for which measurement uncertainties and errors had to be identified, quantified and preferably removed or minimized. Three main factors, whose impact on the measured needle OPs was unclear according to the literature review, were subjected to a detailed analysis. This analysis was a base for the second research question investigated in this thesis (Question B).

At shoot level, needle optical and angular properties are quickly transformed due to the needle clumping within a shoot. Recognizing a significant impact of shoot geometry and structure on multiple light scattering within the canopy, simplified approaches for upscaling the needle spectral signatures to the level of shoots and further to the canopy level are required. Such methods are studied in this thesis for these two spatial scales. (Smolander and Stenberg 2003, 2005) proposed an approach that is upscaling needle albedo to shoot albedo based on the photon recollision probability. Although being theoretically well established, this method has never been empirically verified. Thus, the motivation for the next research question

investigated in this thesis (Question C) was an experimental verification of the needle-to-shoot upscaling approach using the p-parameter.

Finally, accurate modelling of radiative transfer through structurally complex coniferous canopies requires realistic and ecologically correct representations of the forest stands, which in general implies a large number of input parameters and computationally demanding algorithms. An alternative method, that models canopy reflectance using a needle single scattering albedo and a simplified definition of the forest canopy structure, is the photon recollision probability based radiative transfer. The performance of such a simplified approach for estimation of the leaf chlorophyll content from satellite imaging spectroscopy data is investigated and compared to the computationally more demanding approach based on a detailed 3D structural description of a forest as the last task of this thesis (Question D).

In summary, this thesis investigates the following research questions:

- A. What are the shortcomings and uncertainties in measurement methods of optical properties (OPs) of narrow leaves?
- B. What is the influence of the sample holder, the needle cross-section shape and the mutual distance between the needles on the measured leaf reflectance (R) and transmittance (T) factors?
- C. Is it possible to compute shoot albedo (directional-spherical reflectance factor) through the p-theory approach by using only one structural parameter: the spherically averaged shoot silhouette to total needle area ratio (STAR)?
- D. How different is the leaf chlorophyll content of a Norway spruce stand estimated from satellite imaging spectroscopy data using a simple p-theory based approach from the one estimated using a detailed and computationally more demanding 3D canopy RT model?

1.7 Outline

This thesis consists of four thematic chapters, each investigating one of the above research questions. The chapters are based on articles published or submitted for publication in peer-reviewed scientific journals.

Chapter 2 (Question A) presents a review on the state of the art and recent developments in measuring optical properties of narrow leaves. In this chapter we focus on methodological shortcomings and uncertainties, with special attention to non-flat non-bifacial coniferous needle-leaves (e.g. needles of

Norway spruce). We conclude by recommending a set of potential improvements based on the existing methods.

Chapter 3 (Question B) proposes an experimental set-up optimizing established needle-leaf OPs measurement approaches by systematically minimizing their uncertainties. We focus on analyzing the influence of three factors of these needle-leaf OPs measurement approaches: the sample holder effect on the measured signal, the influence of the needle cross-section shape, and the mutual distance between the needles composing a sample. The approach is based on the method of Mesarch et al. (1999), presented in chapter 2.

Chapter 4 (Question C) demonstrates a validation of the theoretical relationship between the photon recollision probability and the STAR structural parameter presented by Smolander and Stenberg (2003, 2005). Here we used empirical optical measurements of Scots pine needles carried out in an integrating sphere and of Scots pine shoots measured using a spectroradiometer mounted on a goniometer.

Chapter 5 (Question D) explores the applicability of the p-theory for the leaf chlorophyll content estimation. The p-theory coded in the canopy model PARAS (Rautiainen and Stenberg 2005) is applied to simulate a BRF of an immature Norway spruce stand using structural and optical information collected over a study area located in Bily-Kriz, Beskydy Mountains (Czech Republic). PARAS leaf chlorophyll content estimates, retrieved by means of chlorophyll sensitive spectral indices (Malenovský et al. 2013), are compared with estimates derived from canopy BRF simulated in the DART model (Gastellu-Etchegorry et al. 2004).

Chapter 6 presents a synthesis and a general discussion together with suggestions for further research.

Chapter 2

Minimizing measurement uncertainties of coniferous needle-leaf optical properties, part I: methodological review

This chapter is based on:

Yáñez-Rausell, L., Schaepman, M.E., Clevers, J.G.P.W., & Malenovský, Z. (2014). Minimizing measurement uncertainties of coniferous needle-leaf optical properties, part I: methodological review. *IEEE Journal of Selected Topics in Applied Earth Observations and Remote Sensing*, 7, 399-405
DOI: 10.1109/JSTARS.2013.2272890

Abstract

Optical properties (OPs) of non-flat narrow plant leaves, i.e. coniferous needles, are extensively used by the remote sensing community, in particular for calibration and validation of radiative transfer models at leaf and canopy level. Optical measurements of such small living elements are, however, a technical challenge and only few studies attempted so far to investigate and quantify related measurement errors. In this paper we review current methods and developments measuring optical properties of narrow leaves. We discuss measurement shortcomings and knowledge gaps related to a particular case of non-flat nonbifacial coniferous needle leaves, e.g., needles of Norway spruce (*Picea abies* (L.) Karst.).

Keywords

Needles; optical properties; reflectance; transmittance; integrating sphere; leaf; conifers; gap fraction

2.1 Introduction

Absorption of visible and infrared light in plant leaves is an essential measurement for better understanding and modeling the photosynthetic process and energy balance that regulates global gas exchange with the atmosphere and consequently global terrestrial primary productivity (Medlyn 1998). Since leaves are the primary photosynthesizing organs, measurement of their optical properties (OPs) (i.e., absorption (A) complemented by the leaf reflectance (R) and transmittance (T)) is a crucial part of this puzzle. Direct measurement of the in-vivo optical absorption properties is still practically impossible (Eng and Baranoski 2007), thus, efforts on measuring leaf OPs have been directed towards quantifying leaf R and T , from which A is derived through the following relationship: $1=A+R+T$. Despite an extensive history in measuring the directional-hemispherical (terminology following Schaepman-Strub et al. (2006)) R and T of plant leaves (Jacquemoud and Ustin 2001), most of the methods have been designed for broad leaves. Measurement of narrow and small size leaves, as for instance coniferous needles or grasses, which represent a significant fraction of natural terrestrial ecosystems (Melillo et al. 1993), is still a technical challenge. Even though OPs of coniferous needles are extensively used by the remote sensing community (Di Vittorio 2009; Feret et al. 2008; Hilker et al. 2008; Kuusk et al. 2009; Kuusk et al. 2010) only limited knowledge about their measurement related errors is available (Mesarch et al. 1999). As a result of this, measurements with unknown accuracy and reliability are used for example for calibration and validation of radiative transfer models simulating reflectance factors of coniferous canopies (Kuusk et al. 2008). The lack of needle OPs measurements and unknown measurement uncertainties have enforced modeling assumptions with a potentially negative impact on interpretation of remote sensing data of coniferous forests, as for instance the needle T being assumed to be equal to zero (Disney et al. 2006), or equal to the needle R (Möttus 2007). This clearly demonstrates a need for a more robust and efficient measurement technique of narrow-leaf OPs.

In this paper we review the state of the art and recent developments in measurement methods for narrow leaf optical properties. We focus on methodological shortcomings and uncertainties, with special attention to non-flat nonbifacial coniferous needle-leaves (e.g., needles of Norway spruce). We conclude by recommending a set of potential improvements based on the

existing methods. We continue to propose an experimental set-up for optimizing established needle-leaf OPs measurement approaches by systematically minimizing their uncertainties in a second part (Chapter 3).

2.2 Needle-leaf optical properties

2.2.1 Photon interactions with a needle-leaf

Photon interactions with a leaf result in a combination of scattering and absorption processes, which are driven by the spectral character and spatial distribution of the incoming collimated and diffuse light (Brodersen and Vogelmann 2010; Gorton et al. 2010) and by the leaf orientation and internal anatomy (Grant 1987; Richter and Fukshansky 1996a, b; Ustin et al. 2001). These attributes determine the degree of attenuation of the light flux passing through foliar tissues (Vogelmann 1993) and the spectral and spatial distribution of the outgoing photon (Bousquet et al. 2005; Combes et al. 2007; Knyazikhin et al. 2013). The irregular shape and orientation of the leaf cells, and also an uneven distribution of absorbers within the foliar tissue (Rabinowitch 1951) makes the leaf a complex optical scattering microenvironment causing for instance sieve and detour effects (Baranoski and Eng 2007). Despite this complexity, light propagation within bifacial broad leaves has been successfully simulated (Baranoski and Rokne 2004; Jacquemoud and Ustin 2001; Ustin et al. 2001), also using leaf radiative transfer (RT) models (Jacquemoud and Baret 1990). The leaf model PROSPECT approximates a bifacial leaf as an infinitely extending plate with distinct multiple layers of cells (Figure 2.1b). In reality the inner layers of pigmented mesophyll cells are covered by epidermal layers, which are protected by outer cuticle layers (Woolley 1971). When the light of a specific wavelength hits the leaf surface, a portion of the incoming photons is scattered outward by the waxy cuticle (Grant 1987) and the complementary portion is transmitted through the leaf's surface layer into the mesophyll tissue. There, the interfaces between air spaces and cell walls cause multiple internal reflections and refractions of the light rays (Woolley 1973). Multiple scattering redirects the light rays in multiple directions. Some photons encounter absorbers and are absorbed; some are scattered in an "upwards" direction, forming, together with the external surface scattering, the leaf R ; and some are scattered out of the leaf in a "downwards" direction resulting in the leaf T .

RT models simulating light-leaf interactions in narrow needle leaves, such as in LIBERTY (Dawson et al. 1998), are scarce and less accurate due to the higher geometrical complexity. First, the cross-section of coniferous needles is hardly similar to a plate configuration (Figure 2.1a), but presents varying geometrical shapes with several facets (Figure 2.1c). When compared to the broadleaf cross-section, these facets increase the number of possible incident angles of the interacting photons. Second, the inner layers are forming a set of dense irregular spherical microstructures rather than the flat regularly layered structure of a typical bifacial broad leaf (Dawson et al. 1998) (Figure 2.1d).

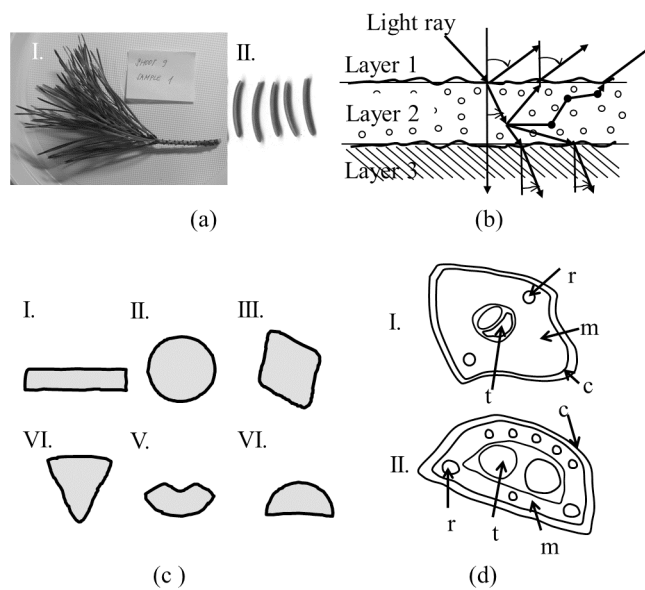


Figure 2.1 (a) *Pinus nigra* shoot (I) and *Picea abies* needles detached from shoot (II); (b) geometry of the light interactions within a typical broad leaf (adapted from Hanrahan et al. (1993)); (c) overview of cross-sectional shapes of conifer needles (adapted from Jordan et al. (1993) and a broad leaf (representing the majority of deciduous species): (I) flat leaf; (II) *Pinus monophylla* (Torr. & F&m.); (III) *Picea asperata* Master; (IV) *Pinus cembra* L.; (V) *Abies nordmanniana* Spach; (VI) *Pinus sylvestris* L.; (d) sketch (modified from Di Guardo et al. (2003) of cross-sections of (I) spruce (*Picea abies*) and (II) pine (*Pinus nigra*) needle (r=resin channel; t=transfer channel; m=mesophyllum; c=cuticle).

2.2.2 Conventional broad-leaf spectral measurements

Conventional measurement of plant leaf OPs consists of directional-hemispherical R and T measurements performed with an integrating sphere coupled to a spectroradiometer (Gorton et al. 2010; Woolley 1971). The leaf measuring integrating sphere, coated inside by a highly reflective material (e.g., barium sulphate), has several dedicated ports, where a collimated light source and the leaf sample can be placed during the measurements. The light beam is illuminating the leaf adaxial or abaxial side, which is covering the sample port (Figure 2.2a). A portion of the incoming photons reaching the leaf surface is scattered (reflected/transmitted) in all directions from/through the leaf. The illuminated area is smaller than the sample port diameter, ensuring that the beam only interacts with leaf tissue. The integrating sphere is collecting and integrating the signal of scattered photons through the whole hemisphere, which is subsequently recorded by a spectroradiometer connected to the sphere with optical fibers.

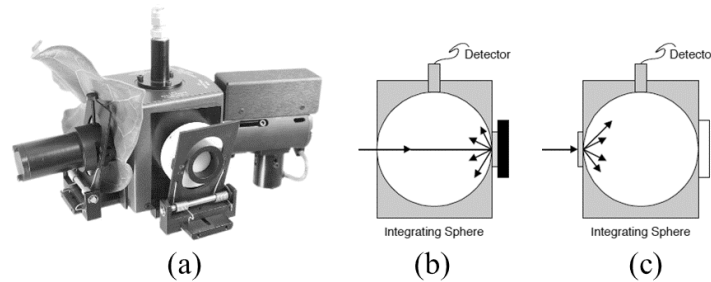


Figure 2.2 (a) Example of a commercial integrating sphere designed for measuring broad leaves (ASD 190 RTS-3ZC) (ASD 2008); (b) Directional hemispherical measurements of leaf reflectance; and (c) Transmittance measurements (adapted from Jacquemoud and Ustin (2001)).

T measurement requires placing the leaf at an entry port of the sphere and illuminating it with direct collimated light from the external side of the leaf. The light enters the integrating sphere through the leaf (Figure 2.2c), which means that the signal recorded by the sensor inside the sphere is the portion of light transmitted through leaf tissue. To measure R , a leaf is also mounted in a sphere entry port, but being illuminated by a collimated light placed in a

port opposite to the sample (Figure 2.2b). This way the collimated light beam passes through the sphere and interacts with the sample from the interior side resulting in a signal reflected back into the sphere. A correction for stray light is required for R measurements. Also correction of the so-called 'single-beam substitution error' must be considered to avoid producing lower R and higher T records occurring when the sample substitutes the portion of the sphere previously occupied by reference material of 100% reflectance (Labsphere Inc). Finally, A can be calculated from the R and T measurements through $A= 1-(R+T)$, where 1 is the total amount of light illuminating the sample leaf, and R , T and A are complementary fractional quantities.

2.2.3 Spectral measurements adapted for needle-leaves

R and T measurements of narrow leaves require a specific adaptation of the conventional single beam integrating sphere measurement techniques due to the leaf size smaller than the illumination light beam. Reduction of the illuminated area to the dimensions of a single narrow needle would result in a too low signal-to-noise and would introduce potential errors of sample misplacements (Daughtry et al. 1989). Placing the light beam-width-limiting slits at the entry port of the integrating sphere induces diffractive effects and does not allow for T measurements (Noble and Crowe 2007). The only solution to increase the illuminated surface of very narrow leaves is to measure simultaneously a set of leaves collected from the same location (i.e. shoot). This approach requires an efficient and reproducible way of placing needle sets within the sampling port of an integrating sphere, ensuring that the R and T are recorded from the same sample leaf area in a time span short enough to prevent the biological degradation of detached leaves. This idea was implemented in three different approaches as described as follows.

The first approach, introduced by Hosgood et al. (1995) within the LOPEX project, consists of measuring an infinite R of needles contained in a glass cuvette positioned at the sample port of an integrating sphere. These R spectra were subsequently corrected for the effect of the cuvette.

As opposed to the above, the other two approaches substitute the cuvette by a flat sample holder that presents only a single layer of needles at the entry port of an integrating sphere. These needles are placed side-by-side at an even distance and fixed between two holder plates, which are tightened and positioned at the sample port (Figure 2.3d). However, different sample holders and subsequent required corrections are applied in both approaches.

The second approach by Harron (2000) (based on Harron and Miller (1995)) is used in several studies of coniferous species (Hernandez-Clemente et al. 2011; Moorthy et al. 2008; Moorthy et al. 2003; Zarco-Tejada et al. 2004; Zhang et al. 2008b). They employ a sample holder made of two black anodized plates with narrow hollow slots. The needles placed inside the slots are closing them completely ensuring that the light can only pass through the leaf tissue (Figure 2.3c).

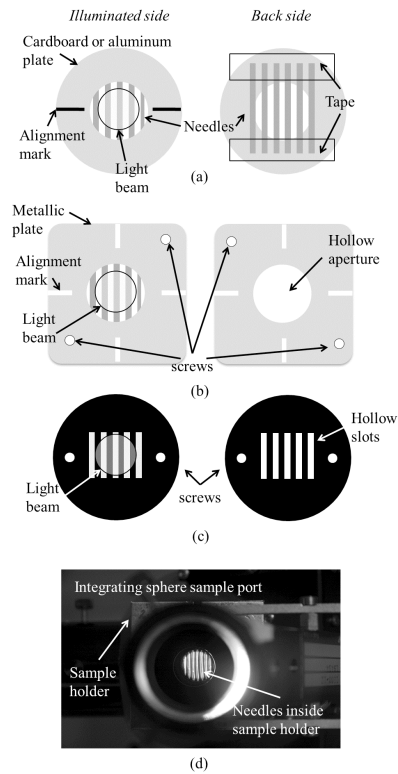


Figure 2.3 Example of needle-leaf sample holders: (a) sample holder used in Daughtry et al. (1989) and Mesarch et al. (1999) (Thickness is approximately half of the needle thickness ≈ 0.7 mm); (b) sample holder used by Malenovský et al. (2006a), which is an adaptation of Mesarch et al. (1999) (Approximate holder thickness ≈ 1 mm); (c) sample holder from Harron (2000) and Harron and Miller (1995) (Approximate thickness ≈ 1.5 mm). In all cases, the needle sample holders are placed in the same position as the broad leaf sample in Figure 2.2; (d) Sample holder placed at the sample port of the integrating sphere (Malenovský et al. 2006a).

The approach requires a correction removing the spectral contribution of the holder itself, which is also illuminated during the measurements. A similar approach, but applicable only to leaves of at least 5 mm in width (which is considerably wider than needles of most coniferous species), was proposed by Noble and Crowe (2007).

In the third approach by Daughtry et al. (1989) and further improved by Mesarch et al. (1999) the sample holder has a hollow central aperture bigger than the illuminated area. The needles presented at this aperture are separated by air gaps in-between them (Figures 2.3a and b). Therefore, an accurate removal of the air gap fraction (GF) between the needles is needed to correct the recorded R and T signal (Middleton et al. 1996; Middleton et al. 1997a; Middleton et al. 1998).

2.3 Benefits and shortcomings of needle-leaf OPs methods

Hosgood et al. (1995) used for the OPs measurements non-portable devices requiring reallocation of the foliar material from field to the laboratory. The use of portable devices is more efficient and provides higher flexibility and lower transportation costs especially during measuring campaigns taking place at remote locations. Moreover, the possibility to acquire OPs in-situ ensures that the measurements are done in a time frame short enough to prevent biological degradation of the leaf samples. Apart from this, no detailed information was found about the positioning of the needles inside the cuvettes, how their position in relation to the light source was affecting the recorded signal or if the signal was averaged based on the specific number of needles measured in each sample. Due to the highly varying size and shape of the needles inside the cuvette, these issues are expected to affect multiple scattering processes within the cuvette. A standardized and reproducible way of positioning the needles is crucial to ensure that R and T are recorded from the same sample area. Finally, a direct T measurement cannot be achieved with this technique.

The approach by Harron (2000) is highly systematic and based on portable measuring devices, but a major drawback is the narrow needle slots of the sample holder. As they are fixed in width and length, the sample holders are species-specific, which requires manufacturing many sample holders with different slot sizes. Moreover, twisted and/or strongly arced needles (e.g., Norway spruce needles) are not properly filling the slots, enforcing measurements of straight needles with a certain width only. Finally, since the

holder presents only the needle core (typically the thickest part) to the sphere, the T measurement might potentially be underestimated (Mesarch et al. 1999).

The Daughtry et al. approach (Daughtry et al. 1989) is using portable equipment (Mesarch et al. 1999), it is not species specific, and it does not require manufacturing a highly advanced sample holder as those used in Harron (2000). However, its weak point is the necessity to retrieve the area of air spaces between the measured needles, also termed gap fraction (GF). Authors suggested that the GF correction factor can be estimated as the ratio of the transmission recorded from a mat of evenly spaced needles painted in black to a 100% transmission measurement (i.e. empty sample port) at 680 nm. The even distance between needles of approximately one-needle width results in a GF of about 0.5. Unfortunately, the requirement to paint the needles in black color is time consuming, and more importantly, the $GF = 0.5$ appeared to underestimate T and overestimate R . A strong reduction of the gap size by using more needles still caused a certain overestimation of the R values, which was attributed to multiple scattering occurring between adjacent needles. Therefore, a modified approach by calculating GF directly through the acquisition of a sample digital image and the subsequent digital extraction of its gap area was proposed by Mesarch et al. (1999). On one hand, this reduced the number of measurements required and further eliminated the needle painting. On the other hand, it added the need to use an imaging system; however, economically feasible adaptations have already been developed (Malenovský et al. 2006a). The method can be applied to narrow leaves of several plant species including grasses (Ramsey III and Rangoonwala 2004) and all sorts of coniferous needles (Acem et al. 2010; Malenovský et al. 2006a; Middleton et al. 1997b).

2.4 Methodological Uncertainties in OPs measurements

Recognizing the above universality requirements, we focus on Mesarch et al. (1999) and use this method as a basis for our recommendations to improve its methodological approach and to minimize the uncertainties of this technique.

The initial Mesarch et al. (1999) method can be summarized with the following five sequential measurement steps: (a) needles are placed in a sample holder with evenly spaced air gaps in between them; (b) the sample R and T signals are recorded using a spectroradiometer coupled with an integrating optical sphere; (c) a digital image of the masked sample holder aperture is acquired (the mask for the central aperture reproduces the size and

position of the light beam illuminating the sphere sample port); (d) the GF of the sample is retrieved using computer-based image processing; (e) the measured spectra and GF are introduced in Equation 2.1 and 2.2 to compute the spectrally dependent directional-hemispherical R (R_{needle}) and T (T_{needle}) of needles as follows:

$$R_{needle} = \frac{R_{TOTAL}}{(1 - GF)} \quad (2.1),$$

and

$$T_{needle} = [T_{TOTAL} - R_w GF] \frac{1}{(1 - GF)} \quad (2.2),$$

where R_{needle} is the R of individual needles, T_{needle} is the T of individual needles, and R_w is the R of the integrating sphere wall (assumed to be close to 100%). Consequently, the R_{TOTAL} and T_{TOTAL} are computed as:

$$R_{TOTAL} = \frac{R_{needle+gaps} - STR}{REF - STR} \quad (2.3),$$

and

$$T_{TOTAL} = \frac{T_{needles+gaps}}{REF - STR} \quad (2.4),$$

where $R_{needles+gaps}$ is the radiation reflected from the sample, including the photons lost through the air gaps; $T_{needles+gaps}$ is the radiation transmitted through the sample, including the photons passing through the air gaps; STR is the stray light radiation and REF is the reference reflectance of a white panel.

To validate the method and to test the effect of the air gaps on the final signal, Mesarch et al. (1999) proposed the concept of using the so-called true GF. They extracted the GF from Equation 2.2, as the true GF that the sample should have in order to estimate the recorded signal for T_{needle} :

$$TrueGF = [T_{TOTAL} - T_{needle}] \frac{1}{1 - T_{needle}} \quad (2.5).$$

They measured the OPs of an optically stable material (a film paper) to simulate broad leaves and narrow needle leaves (i.e. the film paper was cut in narrow strips). Since the OPs are inherent to the material irrespective to their shape and size, they substituted T_{needle} in Equation 2.5 by the T of a broad leaf assuming $T_{needle}=T_{broad-leaf}$. Subsequently they analyzed samples with GF ranging between 0.05 and 0.6 and computed the deviation of the digital GF from the true GF as the error attributable to their approach. Their results showed inherent errors connected to the GF image analysis. A relative error up to 40% was attributed to insufficient camera resolution and misalignment of the mask for the sample illumination beam. When identifying the optimal gap size they found errors being larger in samples having large GFs (0.3-0.6) than in samples of small GFs (0.05-0.15). The large-sized GFs were affecting the T signal more negatively than the R signal. They also measured OPs of flat mesquite leaflets and found them to vary in the same way as the OPs obtained from the film paper measurements. Contrary to this, measurements conducted with fir needles, i.e. leaves having a non-flat cross section, showed an increase in R with decreasing GF. Authors attributed this phenomenon to multiple scattering effects occurring between measured needles (Daughtry et al. 1989). The non-flat cross-section (e.g., circular or rhomboidal) of the evenly spaced needle layer forming the sample allows the collimated light rays to hit the needle surface in a direction different from the normal to the sample front plane. This increases the probability of photons being scattered sidewise and interacting with the neighboring needles, especially if needles are placed too close to each other (i.e. in case of small GF). The scattered light can consequently escape from or be introduced into the integrating sphere during the R and T measurements, subtracting or adding a certain amount of photons to the recorded optical signals. According to published results (Mesarch et al. 1999), authors managed to optimize the method for flat narrow leaves, but not for non-flat needle-shaped leaves, which are in general represented by most of the coniferous species.

Three more problematic issues can be additionally identified from these results, opening space for a methodological revision. First, although this method does not allow for any direct interaction between the illumination beam and the sample holder, it might potentially suffer from an indirect influence of the holder presence (e.g., second order interaction with sample scattered light), as the holder of significant thickness is placed at the sample port of an integrating sphere. The multiple scattering enhanced by the non-flat

cross section of the needles can potentially redirect some of the photons towards the sample holder plates. The increase of the optical path length from the light source to the sample surface and presence of holder edges can induce extra photon recollisions resulting in an unwanted but nonnegligible additional absorption (Merzlyak et al. 2002).

Secondly, the identified deviation from the true GF was attributed to the complex inherent error of the technique as a whole. No sensitivity analysis of the GF to the specific factors involved in the image acquisition and digital image processing (e.g., threshold selection criteria applied for separating the air-needle interface during the digital GF estimation) has been performed.

Finally, the samples are expected to fit in a range of optimal GF values; however, the calculation of GF prior to the measurement is not straightforward or visually feasible. The GF, defined as the ratio of the total gap area between needles to the total measurement area, needs to be measured from irregularly shaped areas. This will have a significant and practical impact on timing and arrangement of a field campaign. On the one hand, there might be extra time needed to calculate the desired GF during sample preparation, when the leaves are already cut and attached to a sample holder. This elongation may cause further biological degradation of the sample before the OPs measurement is finished. On the other hand, if the samples are measured without knowing their GF value, a significant number of OPs might potentially be discarded after the processing due to an unacceptable high uncertainty caused by too large or too small GFs. This further delay, including also potential additional physiological investigations (e.g., carbon assimilation or water potential measurements) that are usually performed in parallel to OPs measurements (Middleton et al. 1997b), can lead to a substantial reduction of overall usable data.

2.5 Conclusion

Progress has been achieved in systematically measuring OPs over the past decades. However, when considering the global ecological relevance of coniferous species with predominantly non-flat needle-shaped leaves, progress is considered relatively slow. When analyzing OPs measurement approaches used in literature, we were able to group them into three predominantly used approaches. These were those suggested by Hosgood et al. (1995), Harron (2000), and Daughtry et al. (1989) (with improvements by Mesarch et al. (1999)).

Revisiting the limitations of *Mesarch's* method revealed further potential for improvements. Given the increasing importance of scaling based approaches (Möttus et al. 2012; Rautiainen et al. 2012; Schaepman et al. 2009) in combination with the ecological importance of ecosystems dominated by non-flat needle-shaped leaves (FAO 2010), improvements to the error-prone Mesarch et al. (1999) method are over-due.

2.6 Outlook

To further reduce parts of the above uncertainties addressed, we propose an experimental set-up improving the original method of Mesarch et al. (1999). Our experiment has three main objectives: 1) to investigate the potential of indirect influence of the sample holder presence on the measured leaf R and T , 2) to evaluate the errors introduced by image acquisition and processing settings applied to compute the sample GF, and 3) to investigate the possible occurrence of multiple scattering induced by the non-flat profile of the conifer needles, focusing on: a) the influence of the needle cross-section shape and b) the particular distance between the needles in the sample, instead of in the GF size itself. A detailed methodological description and final outcomes of this experiment are presented in Chapter 3.

Chapter 3

Minimizing measurement uncertainties of coniferous needle-leaf optical properties, part II: experimental set-up and error analysis

This chapter is based on:

Yáñez-Rausell, L., Malenovský, Z., Clevers, J.G.P.W., & Schaepman, M.E., (2014). Minimizing measurement uncertainties of coniferous needle-leaf optical properties, part II: experimental set-up and error analysis. *IEEE Journal of Selected Topics in Applied Earth Observations and Remote Sensing*, 7, 406-420
DOI: 10.1109/JSTARS.2013.2292817

Abstract

We present uncertainties associated with the measurement of coniferous needle-leaf optical properties (OPs) with an integrating sphere using an optimized gap-fraction (GF) correction method, where GF refers to the air gaps appearing between the needles of a measured sample. We used an optically stable artificial material simulating needle leaves to investigate the potential effects of: 1) the sample holder carrying the needles during measurements and 2) multiple scattering in between the measured needles. Our optimization of integrating sphere port configurations using the sample holder showed an underestimation of the needle transmittance signal of at least 2% in flat needles and 4% in nonflat needles. If the needles have a nonflat cross section, multiple scattering of the photons during the GF measurement led to a GF overestimation. In addition, the multiple scattering of photons during the optical measurements caused less accurate performance of the GF-correction algorithms, which are based on the assumption of linear relationship between the nonGF-corrected signal and increasing GF, resulting in transmittance overestimation of nonflat needle samples. Overall, the final deviation achieved after optimizing the method is about 1% in reflectance and 6% in transmittance if the needles are flat, and if they are nonflat, the error increases to 4%–6% in reflectance and 10%–12% in transmittance. These results suggest that formulae for measurements and computation of coniferous needle OPs require modification that includes also the phenomenon of multiple scattering between the measured needles.

Keywords

Conifers; gap fraction (GF); integrating sphere; leaf; needles; optical properties (OPs), reflectance, transmittance.

3.1 Introduction

Recent methods for measuring the narrow leaf optical properties (OPs), with special attention on nonflat non-bifacial coniferous needle leaves (e.g., Norway spruce needles), have been reviewed (Yáñez-Rausell et al. 2014b). Based on the outcomes of this review, we propose an experimental setup optimizing the “Mesarch et al.”’s needle-leaf OPs measurement approach (Mesarch et al. 1999). The proposed experiment addresses the following objectives: 1) to investigate a potential influence of the sample holder’s presence on the measured leaf reflectance (R) and transmittance (T) and 2) to investigate the effect of varying gap fraction (GF) and multiple scattering between neighbor needles, focusing on: a) the influence of the needle cross-section shape and b) the distance between the needles in the sample. In case of a needle cross-section influence, we hypothesize that higher occurrence of small illumination incident angles, caused by a circular or rhomboidal needle cross-section shape, increases multiple scattering between the measured needles. In other words, the photons hitting the needle surface in a direction different from the normal to the needle surface have higher probability to interact with needles in their near neighbourhood (Mesarch et al. 1999). Simultaneously, we hypothesize that an increasing distance between the needle sample elements (larger air gaps) decreases the probability of multiple scattering in between them (Mesarch et al. 1999).

After analyzing the experimental results, we outline the recommendations for the best practice ensuring reliable measurements of coniferous needle OPs.

3.2 Materials

3.2.1 Artificial needle leaves

To carry out our analyses, we used artificial needle leaves of 1-mm width that were cut-off from two types of materials of known R and T . Contrary to real leaves, both materials were optically stable over time, i.e., temporally nondegrading (at least during the experiments) ensuring that measured R and T of the same material would result in similar material uncertainty. Also, assuming that the R and T were inherent properties of the material itself, the OPs obtained from the artificial needle samples were fully comparable with OPs measured on uncut “broad-leaf-like” pieces of the same material. This

study focuses on the estimation of errors from the measuring technique; thus, not reproducing exactly the spectral signatures of real needles is not affecting the conclusions of this study.

The first selected material was a green-colored plastic (0.1-mm thick) with OPs similar to the photographic film used by Mesarch et al. (1999). This material simulated what we call “flat narrow leaves” (e.g., geometrical shape similar to grass, mesquite leaflets, etc.). The second material was a green silicon mat (1.0-mm thick) that simulated what we call “nonflat narrow needle leaves” (i.e., leaves of many coniferous species). The silicon was chosen due to a suitable transmittance (up to 50% below 800 nm) and a thickness comparable to the real coniferous needles, e.g., Norway spruce (*Picea abies* (L.) Karst.) needles. “Broad-leaf-like” pieces of each material (uncut) were measured and used as a reference.

3.2.2 Measurement protocol for narrow-leaf OPs

For our analysis, we followed the five steps as summarized in the Mesarch et al.’s approach (Mesarch et al. 1999) for measuring narrow-leaf R and T . The OPs were measured using a spectroradiometer (ASD Field- Spec 3) coupled with a portable single-beam ASD leaf-integrating sphere (ASD 190 RTS-3ZC; Figure 3.1b).

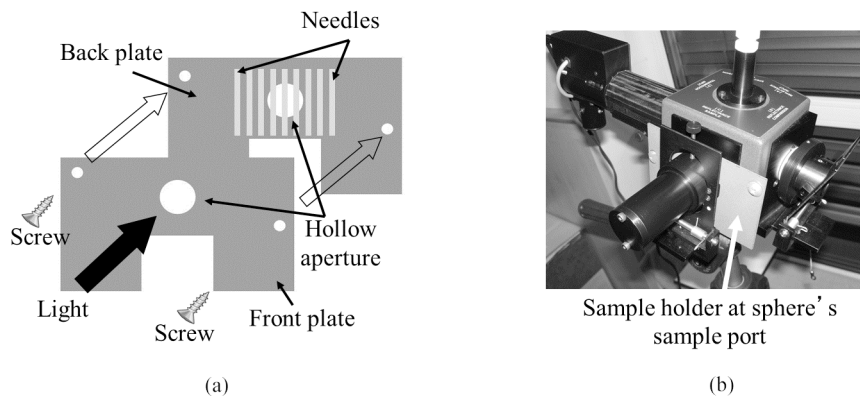


Figure 3.1 (a) Sample holder with a sample and (b) integrating sphere (ASD 190 RTS-3ZC) used for the measurements with the sample holder machined to perfectly fit the sample ports.

During the measurements, the flat plastic and silicon needles were placed in a sample holder similar to the one described in Malenovský et al. (2006a) that was specially machined to fit the integrating sphere. The holder consists of two 1-mm-thick optically flat (black-painted) metallic plates and a central aperture larger than the sample port (16.5 mm in diameter) (Figure 3.1a). The holder shape fits firmly to the sphere sample ports, ensuring consistent OPs measurements from both sides (Figures 3.1a and b).

A laser pointer located above the sphere light source assembly ensured no misplacement of the lamp assembly during measurements. To prevent residual light leaks, the integrating sphere was covered with a black, low-reflecting cloth during all optical measurements. A light tunnel of the length equal to the diameter of the ASD-integrating sphere was introduced for T measurements to ensure that the same sample area of comparable size is being illuminated and measured during both R and T readings. Masks mimicking the shape and size of the sample illumination area were built from a black-painted paper. Digital images of the masked sample holder aperture (i.e., the area presenting the needles during the optical measurements) were acquired with a double-lamp scanner (EPSON Perfection TM 4490 PHOTO) and stored in an 8-bit gray-scale format. During the sample scanning, masks were precisely aligned and fixed to the sample holder plates, and these were positioned using references previously marked on the scanner window in order to minimize misplacements. All these steps contributed to the optimization of the optical measurements and scanning protocol and improved repeatability. We used the images to estimate the sample GF, defined as the ratio of the total gap area between the needles to the total measurement area. The total number of gap pixels in the masked image was calculated by applying a “white-pixel-threshold” to discriminate gap pixels from needle pixels (Mesarch et al. 1999) using the image processing software GIMP 2.6, GNU. We will refer to this computed GF as $Digital_{GF}$. The measurement area, i.e., size of the illuminating beam, was slightly different in R and T modes (9 and 7 mm in diameter, respectively), which required one R and one T mask and resulted in two $Digital_{GF}$ values per sample.

The measured spectra and $Digital_{GF}$ were introduced in the GF-correction formulae (Mesarch et al. 1999) to compute the individual-needle-leaf directional-hemispherical R_{needle} (Equation 3.1) and T_{needle} (Equation 3.2) per sample per spectral waveband as in

$$R_{needle} = \frac{R_{TOTAL}}{1 - GF} \quad (3.1),$$

and

$$T_{needle} = \frac{(T_{TOTAL} - R_w \cdot GF)}{1 - GF} \quad (3.2),$$

where R_{needle} is the R of individual needles, T_{needle} is the T through individual needles, and R_w is the R of the integrating sphere wall (assumed to be close to 1, i.e., 100%). The R_{TOTAL} and T_{TOTAL} variables are the samples R and T , respectively, computed as the recorded total reflected and transmitted radiation, including the photons lost or added by the air gaps, but corrected for the stray light and normalized to the reflectance of a white reference panel (cf., Appendix I).

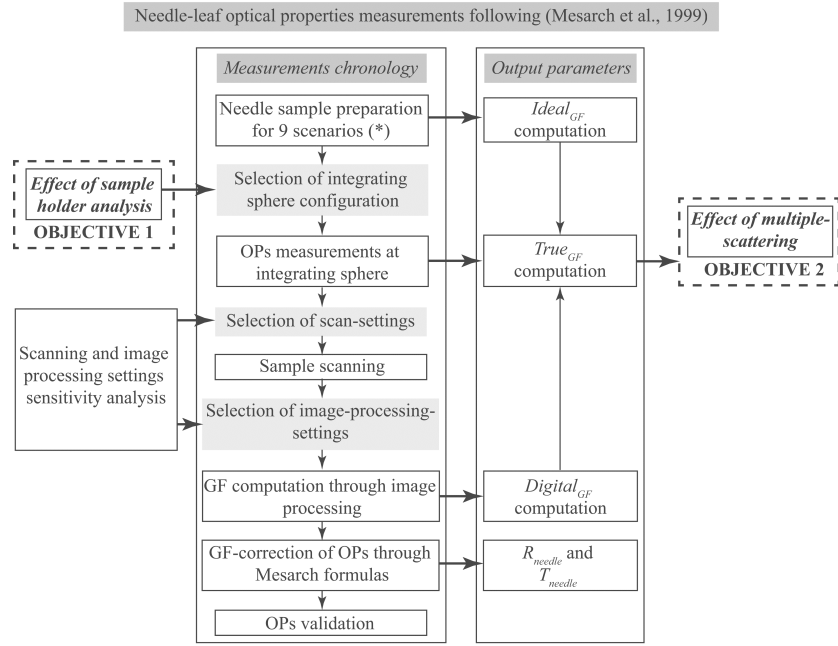


Figure 3.2 Experimental setup: (*) these scenarios refer to the nine needle-sample scenarios (F1, F2, F3, S1, S2, S3, Rh1, Rh2, and Rh3) built to analyze the “effect of multiple scattering” (Section 3.2.4). The scenarios were built by combining three cross-section types (flat- F , squared- S , or rhomboidal- Rh) and three air-gap distances, (index= 0.5 mm (e.g., F1), 2=1.0 mm, and 3=1.5 mm). Best outputs from the “effect of sample holder” analysis (Section 3.2.3), $R_{uncutSH}$ and $T_{uncutSH}$, are used as references for the “OPs validation” of the GF-corrected- needle-OPs computed per scenario (R_{needle} and T_{needle} ; Section 3.2.5). Best outputs from the “scan-and image-processing settings sensitivity analysis” (Appendix II) are used as final scanning and processing settings for the “sample scanning” and “GF computation through image processing” for all samples of the nine needle-sample scenarios.

A summary of the experimental setup followed to achieve our objectives is presented in Figure 3.2. For simplicity, from now on, we will refer to Mesarch et al. (1999) as *Mesarch*, to avoid repeating continuously the same reference.

3.2.3 Effect of the sample holder

Prior to the needle-leaf OPs measurements, we measured the reference R ($R_{reference}$) and T ($T_{reference}$) signal of 10 samples of uncut pieces from both artificial materials: flat plastic and silicon. The sample sizes were bigger than the measurement area (i.e., size of the illuminating beam; Figure 3.3a and d) and for simplicity we will refer to them as to broad-leaf samples. Their OPs were measured without the special sample holder, following the standard leaf measurement protocol recommended by the integrating sphere manufacturer.

To test the effect of the sample holder, each broad-leaf sample was subsequently placed between the sample holder plates (SH) and then its R ($R_{uncutSH}$) and T ($T_{uncutSH}$) were measured using four sample holder scenarios. These scenarios consisted of modified configurations of the integrating sphere ports (Table 3.1). In the first scenario the sample holder was used only for holding the sample at the sample port. In the three remaining scenarios, however, the stray light (*STR*) or “white reference” (*REF*) measurements also involved placing the sample holder at the corresponding port, i.e., an empty sample holder was placed at the sample port or in front of the white reference while acquiring *STR* or *REF* measurements (Table 3.1 and Appendix I).

The root mean square errors per scenario from the resulting averaged $R_{uncutSH}$ and $T_{uncutSH}$ were then computed for each material by using:

$$RMSE_{sp_{SH}}(i) = \sqrt{\frac{\sum_{\lambda=1}^m (sp_{uncutSH}(\lambda, i) - sp_{reference}(\lambda))^2}{m}} \quad (3.3),$$

where $sp_{uncutSH}(\lambda, i)$ is the mean $R_{uncutSH}$ or $T_{uncutSH}$ of 10 samples per scenario at wavelength λ for one of the two materials, i refers to the sample holder scenario number ($i=1, \dots, 4$), and $sp_{reference}(\lambda)$ is the corresponding mean $R_{reference}$ or $T_{reference}$ of 10 samples at the same wavelength λ and for the same material. The wavelength λ varies from 450 to 1700 nm. The spectral range below 450 and above 1700 nm was removed due to an insufficient signal-to-noise ratio caused by the spectroradiometer and integrating sphere.

Finally, for each material, the scenario corresponding to the minimal error was selected as the optimal measuring setup and used for OPs measurements of needle samples.

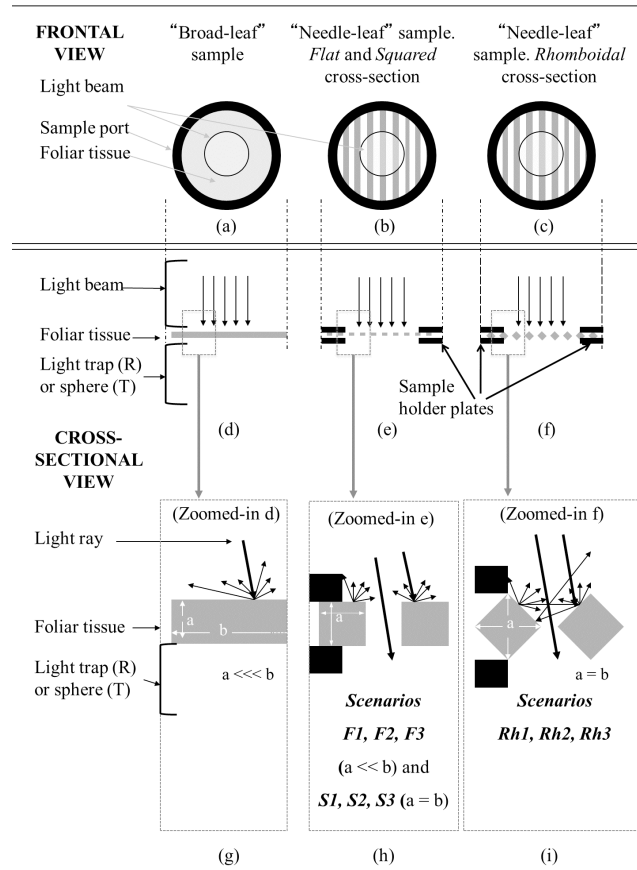


Figure 3.3 Frontal and cross-sectional view of the each sample type when placed at the integrating sphere port: the “broad-leaf” samples from both materials [(a), (d), (g)] and the nine standard-needle-sample scenarios: *F1*, *F2*, and *F3* (flat cross-section needles); *S1*, *S2*, and *S3* (squared cross-section needles); and *Rh1*, *Rh2*, and *Rh3* (rhomboidal cross-section needles). Distance between needles is illustrative. Thickness “a” (h) in *F1*, *F2*, *F3* is much smaller than the length “b” while it is equal to b in *S1*, *S2*, and *S3*. If the sample is placed at the integrating sphere in *R* mode, the light beam is hitting one side of the sample while the light trap is at the other side of the sample; if the sample is placed in *T* mode, the light beam is hitting one side of the sample while the sphere is at the other side of the sample. In (a)–(c), the sample holder is not visible, since the central aperture is bigger than the sphere port. The illuminated area is always smaller than the area of the sample. The arrows represent the incoming light rays and their multiple scattering at the surfaces. Volume scattering (inside the sample) is not shown.

Table 3.1 Sphere configurations per sample holder scenario. L, integrating sphere external light source; W, white reference; S, sample; O, empty port (with light trap); P, white plug; +SH, sample holder is used, e.g., in “S+SH” the sample holder is holding the sample; in “W+SH” the sample holder plate is between the port and the white reference. Ports A–E correspond to the ASD integrating sphere ports (ASD 190 RTS-3ZC). Scenario 1 is the starting scenario and the one used by Mesarch et al. (1999). In Scenario 2, we only add a sample holder plate to the W (i.e., sample holder plate between the sphere and the W). Scenarios 3 and 4 (not shown) correspond to the same setup as Scenarios 1 and 2, respectively, but adding an empty sample holder at the corresponding empty port during the *STR* signal measurements in both *R* (Refl. mode) and in *T* (Trans. mode). Refer to Appendix I for details about these configurations.

Scenario	Quantity	Sphere plugs configuration per port				
		Port A	Port B	Port C	Port D	Port E
1	R _{SAMPLE}	L	W	S+SH	P	P
	STR _{Refl.mode}	L	W	O	P	P
	REF _{Refl.mode}	L	S+SH	W	P	P
	T _{SAMPLE}	P	W	O	L+S+SH	P
	STR _{Trans.mode}	P	O	W	L	P
	REF _{Trans.mode}	P	W	S+SH	L	P
2	R _{SAMPLE}	L	W+SH	S+SH	P	P
	STR _{Refl.mode}	L	W+SH	O	P	P
	REF _{Refl.mode}	L	S+SH	W+SH	P	P
	T _{SAMPLE}	P	W	O	L+S+SH	P
	STR _{Trans.mode}	P	O	W	L	P
	REF _{Trans.mode}	P	W+SH	S+SH	L	P

3.2.4 Effect of the multiple scattering between neighbor needles

To test the two hypotheses concerning the impact of multiple scattering of light, we built nine needle-sample scenarios with artificial needles. A needle sample is composed of several needles built from a specific needle cross-section type, which are placed parallel to each other at a specific distance inside the sample holder plates. The scenarios, called *F1*, *F2*, *F3*, *S1*, *S2*, *S3*, *Rh1*, *Rh2*, and *Rh3*, were built by combining the three cross-section types (flat-*F*, squared-*S*, or rhomboidal-*Rh*) and three air-gap distances [index *l*=0.5 mm (e.g., *F1*), 2=1.0 mm, and 3=1.5 mm]. The flat cross section (*F*) corresponds to flat plastic needles (Figures 3.3b, e, and h), the squared cross section (*S*) corresponds to silicon needles positioned inside the sample holder with two needle sides lying on the sample holder plates and parallel to them (Figures 3.3b, e, and h), and the rhomboidal cross section (*Rh*)

corresponds to silicon needles positioned inside the sample holder with no needle sides parallel to the sample holder plates (Figures 3.3c, f, and i). Two sewing needles (commercial steel dressmaker pins of size no. 12, 19 mm in length and 0.5 mm in diameter) were pushed through the upper and lower ends of each artificial needle to ensure the desired alignment of silicon needles in the sample. Achieving the aimed gap distances between the sample needles required positioning them very carefully using previously marked references on the sample holder plates. However, manual handling of the small needle elements is extremely difficult and small misplacements are practically unavoidable. Consequently, the real achieved gap distances between needles in a sample can differ slightly from the theoretical values aimed for each scenario (0.5, 1.0, or 1.5 mm). We will refer to this error as the best-effort-handling deviation (*BEHD*). Also, the selection of the gap distances was driven by the *BEHD*, as it was not feasible to place needles at a distance smaller than half their width with a sufficient accuracy. After several trials, the smallest gap distance considered was 0.5 mm, i.e., half the needle width (the half-width of *Rh* cross-section needle is slightly larger, being equal to 0.7 mm). Our hypothesis regarding the *BEHD* is that it increases for the same needle cross-section scenario (*F*, *S*, or *Rh*) with decreasing gap distance (starting from 1.5–1.0 to 0.5 mm) and due to the handling difficulty it is bigger for *Rh* than for *F* and *S* for the same gap-distance scenarios. We opted for building our analysis on the gap distance between the needles instead on the GF size used by *Mesarch* because computing the sample GF (i.e., the ratio of the total gap area between the needles to the total measurement area) is, first, not visually straightforward (i.e., requires computing the area of polygon-shaped air gaps intersected by a circular light beam (Figures 3.3b and c) and second, sample-dependent (each needle size is different when using *in-vivo* coniferous needles). This means that, once the needles are detached from the shoot and placed inside the sample holder, several trial and error realignments and GF-computations per sample are needed to approximate the desired GF. For real needles, where the foliar tissue degradation starts several minutes after detachment from the shoot, this adjustment procedure might result in degraded biochemistry and structure (Lichtenthaler 1987).

We prepared 10 samples for each of the nine scenarios and measured their OPs reproducing the best sample-holder scenario resulting from the sample holder effect analysis. In all cases, the spectral range below 450 and above 1700 nm was again removed because of large noise.

After the OPs measurements, three GF values were computed for each R and T mode: $Ideal_{GF}$, $Digital_{GF}$, and $True_{GF}$. The $Ideal_{GF}R$ and $Ideal_{GF}T$ are theoretical GFs computed per scenario by using simple trigonometry based on the known size of the illuminated area (represented by the R or T mask), the needles, and the air-gaps corresponding to each scenario. Due to the $BEHD$, the real sample GF differs slightly from the $Ideal_{GF}$. To compute the $Digital_{GF}R$ and $Digital_{GF}T$, each sample was masked, scanned, and digitally processed (Section 3.2.2). We identified the optimal scan settings [resolution (r), brightness (b) and contrast (c)] and the “white-pixel-threshold” value (t), required to discriminate the air gap and needle pixels in the digital image (cf., Appendix II).

Finally, based on *Mesarch's* definition of the “true” GF, we computed the $True_{GF}T$ per sample of each scenario. This computation consists in substituting the GF-corrected T spectrum of an individual needle, T_{needle} (Equation 3.2), by its corresponding broad-leaf “true” (“nongap”) T spectrum, and in extracting the GF value from the equation. The T_{needle} is assumed to be equal to $T_{uncutSH}$ since, after the GF correction, both quantities should represent the inherent OP of the measured material (Mesarch et al. 1999). This way the $True_{GF}T$ can be extracted through

$$True_{GF}T(\lambda) = \frac{T_{TOTAL}(\lambda) - T_{uncutSH}(\lambda)}{1 - T_{uncutSH}(\lambda)} \quad (3.4).$$

The same strategy is applied in case of R to compute the $True_{GF}R$. The GF is extracted from *Mesarch's* R_{needle} formula (Equation 3.1) as

$$True_{GF}R(\lambda) = \frac{R_{TOTAL}(\lambda) - R_{uncutSH}(\lambda)}{R_{uncutSH}(\lambda)} \quad (3.5).$$

To neutralize the sample holder's effect affecting T_{needle} , in Equation 3.4, we used the $T_{uncutSH}$ resulting from the best sample holder scenario (Section 3.2.3) instead of the broad-leaf $T_{reference}$. Using T spectra measured under the same sample holder scenario ensures that the reference is equally affected by the same holder's effect. The same applies for $R_{uncutSH}$ in Equation 3.5. Since the thickness of a rhomboidal needle is not exactly the same as the thickness of a flat silicon *broad-leaf* (“nongap”) sample, the concept of $True_{GF}$ applied to the rhomboidal cross-section samples might be slightly biased. Mean

volumes of a squared cross-section needle sample and a rhomboidal one are, however, equivalent, and thus we assume that absorption of a rhomboidal needle (A_{needle}) is comparable to the absorption of a flat silicon broad-leaf one ($A_{uncutSH}$), especially at wavelengths with prevailing light scattering and low absorbance. According to Mesarch et al. (1999), the three-dimensional profile of nonflat needle cross-section (e.g., circular, semicircular, or rhomboidal) increases the probability of photon multiple scattering between the measured elements especially if the needles are close to each other (i.e., at small gap distance). The scattered light can escape from or be introduced into the integrating sphere during measurements, subtracting or adding a certain amount of photons to the recorded optical signals. This effect is not taken into account in *Mesarch's* formulae (cf., Equation 3.1 and 3.2), since the fraction of incoming light passing through the sample air gaps, for which the signal has to be corrected, is calculated based on a two-dimensional solution [i.e., the gap size was computed by subtracting the sample needle-projected area from the total measured (illuminated) area]. Therefore, one can expect the multiple scattering effects to influence the $True_{GF}$ values computed from *Mesarch's* formulae. If the needle transmittance computed using the GF correction is overestimated, then by using Equation 3.2 and 3.4 the relationship $T_{needle} > T_{uncutSH}$ can be expressed as

$$\frac{T_{TOTAL}(\lambda) - GF}{1 - GF} > \frac{T_{TOTAL}(\lambda) - True_{GF}T(\lambda)}{1 - True_{GF}T(\lambda)} \quad (3.6),$$

where GF refers to the “real” sample GF. Thus the “real” sample GF is smaller than $True_{GF}T$. The opposite occurs if T_{needle} is underestimated, i.e., the “real” sample GF is larger than the computed $True_{GF}T$. Following the same rationale, if the needle reflectance computed using the GF correction is overestimated, i.e., $R_{needle} > R_{uncutSH}$, the “real” sample GF is, based on Equation 3.1 and 3.5, larger than $True_{GF}R$. The contrary applies if R_{needle} is underestimated.

Our hypotheses related to the effects of multiple scattering on *Mesarch's* method focused on the influence of two factors: 1) the needle cross-section shape and 2) the distance between the needles in the sample. Regarding 1), we expect that for the same gap distance (e.g., $F2$, $S2$, and $Rh2$), the deviation caused by the multiple scattering effects will increase from flat (F) to squared (S) to rhomboidal (Rh) cross-section types, due to differences in the light incident angles and in the volume scattering occurring in nonflat cross-section

scenarios S and Rh (Figures 3.3h and i), i.e., the subsurface scattering inside the needles (Baranoski and Rokne 2004). Concerning 2), we hypothesize that for the same cross-section scenarios (e.g., $S1$, $S2$, and $S3$) the deviation caused by the multiple scattering effects will increase with decreasing gap distance (from 1.5–1.0 to 0.5 mm). This is based on the assumption that photons hitting a needle at angles different from the normal to the needle surface are more likely to re-interact with neighbor needles (e.g., Rh cross-section, Figure 3.3i compared to F cross section, Figure 3.3h), especially if the needles are closer to each other as in small gap-distance scenarios. To test these hypotheses, we computed the deviation $Digital_{GF}$ and the $True_{GF}$ from the theoretical $Ideal_{GF}$ using

$$RMSE_{gf_{DI}}(i) = \sqrt{\frac{\sum_{s=1}^n (Digital_{GF}(s,i) - Ideal_{GF}(i))^2}{n}} \quad (3.7),$$

and

$$RMSE_{gf_{TI}}(i) = \sqrt{\frac{\sum_{\lambda=1}^m \sum_{s=1}^n (True_{GF}(\lambda,s,i) - Ideal_{GF}(i))^2}{m \cdot n}} \quad (3.8),$$

where s refers to the sample number ($s=1, \dots, 10$), i to the scenario number ($i=1, \dots, 9$) and λ to the particular wavelength (varying from 450 to 1700 nm). The different cross-section shapes and distances between needles are expected to affect the sharpness of the needle edges in the scanned digital image and subsequently the output $Digital_{GF}$ computed from this image. Therefore, Equation 3.7 deals with the effect of the light scattered during the sample scanning. The $Digital_{GF}$ values used in Equation 3.7 corresponded to the optimized scanning and processing settings resulting from the sensitivity analysis (Appendix II). Equation 3.8 focuses on the effect of the needles' multiple scattering during the sample spectral measurements. Ideally, the $True_{GF}$ value should be equal to the "real" sample GF. However, as explained above, factors 1) and 2) are expected to influence the scattering behavior of the incoming photons and cause over-/under-estimation of the $True_{GF}$ values extracted from *Mesarch's* formulae (cf., Equation 3.1 and 3.2). Both

$RMSE_{gf_{DI}}$ and $RMSE_{gf_{TI}}$ are affected by the *BEHD*. Despite the *BEHD*, the theoretical $Ideal_{GF}$, which is computed from the fixed dimension of the artificial needle element and air gaps established per scenario, is the closest reference to the “real” sample GF available. Additionally to the RMSE computations, a paired Student *t*-test on the probability level $\alpha=0.05$ was applied to test significant difference between $Ideal_{GF}$, $Digital_{GF}$ and $True_{GF}$ per scenario (i.e., difference between *R* and *T* mode) and also between the scenarios.

Since dimensions of “real” needle leaves vary, GF correction of “real” narrow leaves measured with *Mesarch’s* method can rely only on the $Digital_{GF}$ values. Thus, to test our hypotheses, we also computed the $True_{GF}$ deviation from the corresponding $Digital_{GF}$ for both *R* and *T*

$$RMSE_{gf_{TD}}(i) = \sqrt{\frac{\sum_{\lambda=1}^m \sum_{s=1}^n (True_{GF}(\lambda, s, i) - Digital_{GF}(s, i))^2}{m \cdot n}} \quad (3.9).$$

Equation 3.9 gathers both effects considered in Equation 3.7 and 3.8 and neutralizes the *BEHD*, as the *BEHD* of the same sample does not change.

Finally, we expect that the amount of photons affected by the multiple scattering during the *R* measurements is the same as during the *T* measurements for a given sample, because the needle elements are not re-aligned between both measurements. Flipping the sample holder when switching from the *R* to the *T* measurement mode ensures that the same side of the sample is always facing the light source. This, however, does not mean that the multiple scattering has the same over-/under-estimating effect on the final *R* and *T* spectra (Mesarch et al. 1999).

3.2.5 Validation of OPs after GF correction

The individual needle-leaf directional-hemispherical *R* (R_{needle}) and *T* (T_{needle}) (for terminology see Schaepman-Strub et al. (2006)) per sample per spectral waveband was computed using *Mesarch’s* formulae for GF correction (Equation 3.1 and 3.2). The $Digital_{GF}$ used for the correction are the values corresponding to the optimized scanning and processing settings. The resulting R_{needle} and T_{needle} spectra were compared to the corresponding reference through

$$RMSE_{sp_{needle}}(i,ref) = \sqrt{\frac{\sum_{\lambda=1}^m \sum_{s=1}^n (sp_{needle}(\lambda,s,i) - sp_{broadleaf}(\lambda,i,ref))^2}{m \cdot n}} \quad (3.10).$$

where sp_{needle} is the R_{needle} or T_{needle} , $sp_{broadleaf}$ is the average broad-leaf reference, i is scenario number ($i=1, \dots, 9$), s is the sample number ($s=1, \dots, 10$), and λ is the wavelength in the range 450–1700 nm. The $sp_{broadleaf}$ depends on the *broad-leaf* reference type (*ref*): 1) the broad-leaf R or T for the best sample holder scenario ($R_{uncutSH}$ or $T_{uncutSH}$); or 2) the broad-leaf R or T measured without sample holder ($R_{reference}$ or $T_{reference}$). In 2), the RMSE in Equation 3.10 comprised all potential error sources in the method including the sample holder effect, the $Digital_{GF}$ estimation effect after optimizing the scanning and image processing settings, and the multiple scattering effect between the neighbor needles. In 1), the reference $sp_{broadleaf}$ and the needle spectra sp_{needle} suffer from the same potential sample-holder effects and thus this effect is not included in the output RMSE. Statistical difference between R_{needle} or T_{needle} and the corresponding $sp_{broadleaf}$ was tested through a paired Student t -test on the probability level $\alpha=0.05$.

In addition, we computed sp_{needle} ignoring the GF correction, i.e., using the standard formulae suggested by the sphere manufacturer for broad (uncut) leaves. The sp_{needle} is, therefore, the signal before the GF correction, i.e., the sample R_{TOTAL} in (Equation 3.1) and T_{TOTAL} in (Equation 3.2) formed by both the needle elements and the air gaps and normalized to the white reference panel. The relationship between these nonGF-corrected reflectance and transmittance signals and the sample GF is expected to be linear, given no error in estimation of GF and no interactions between sample elements and incident beam (Mesarch et al. 1999). However, our multiple scattering hypothesis assumes that light interactions between the needle elements should affect this relationship in a nonlinear way. To verify this expectation, a function fitting analysis was applied per cross-section scenario to assess the nature of the relationship.

3.3 Results and discussion

3.3.1 Effect of the sample holder

First, the effect of introducing a special sample holder for narrow leaves is presented in terms of RMSE based on Equation 3.3. The results showed that,

although the sample holder was never hit by direct light, it caused a signal underestimation at almost all the wavelengths along the selected range, especially for T as illustrated in Figure 3.4. Scenario 2 produced the minimum deviation from the corresponding reference signal (Table 3.2). Thus, if compared to the standard sample holder setup (Scenario 1), adding a sample holder in front of the white reference while acquiring the REF measurements (Table 3.1, Scenario 2) decreases the T error to a value of 2% in flat material and 4% in silicon. Error differences between both materials can be attributed to their different OPs and thickness. Scenarios 3 and 4 produced an error per material equal to the one in Scenarios 1 and 2, respectively (results not shown), revealing that an empty sample holder added at the corresponding empty port during the stray light measurements (Table 3.1, Scenarios 3 and 4) has neither effect on R nor on T . This shows that no light leaks in the measuring system were introduced by the use of a sample holder.

The fact that there is no direct reflection from the sample holder contaminating the signal suggests that the driving force of this error is probably the distance of the sample to the integrating sphere's inner surface caused by the sample holder use. According to Merzlyak et al. (2002), due to the external integrating sphere ports, the outer wall of the sphere is a few millimeters away from the reflecting inner wall and thus a fraction of the transmitted light fails to strike the integrating surface due to absorption around the port edge producing a systematic underestimation of T . When using a sample holder, this effect is likely to increase due to the increased distance. These absorbed photons might explain the underestimation of both R and T in our results, especially in Scenario 1 (Figure 3.4). In Scenario 2, the same absorption affects the measured reference signal to which the recorded R and T signal is normalized, compensating this effect to some extent. Exceptionally, T of the flat plastic material is overestimated up to 10% above 1100 nm.

In our experiment, the 1-mm thickness of the sample holder was selected after several tests done with different thicknesses of the same metallic plates. The sample holder thickness of 1 mm was the minimum thickness possible to prevent the plates from bending slightly when adjusting them to firmly hold real needles of Norway spruce (*P. abies* (L.) Karst.). With thinner plates, we experienced that when screwing the plates to trap the needles in between them (Figure 3.1a) and prevent misplacements during the measurements, the plates were slightly bending and therefore affecting the position of the illuminated area of the sample and increasing the distance to the sphere's inner wall. Thus, we do not recommend to use thinner plates for needles as thick as 1 mm;

however, if the purpose is to measure thinner narrow leaves (e.g., grass) it might be possible to reduce the error by decreasing the thickness of the plates.

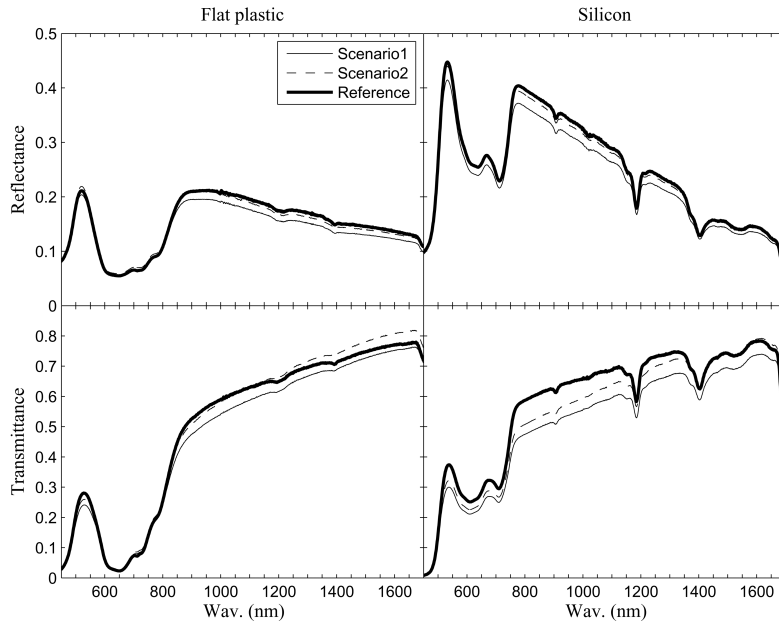


Figure 3.4 Average reflectance and transmittance measurements (fractional quantities 0–1) from broad-leaf flat plastic samples (left graphs) and silicon (right graphs), measured by positioning of the sample holders corresponding to Scenario 1, Scenario 2, and without sample holder used (“Reference”).

We did not test corrections for the absorption effects suggested by Merzlyak et al. (2002), which are based on the assumption of negligible absorption of real broad leaves in the NIR. In addition, it was shown that the effect is not systematic (Gorton et al. 2010). In needle samples, the multiple scattering caused by the nonflat nature of the needles might cause a portion of the light to be scattered directly onto the edge of the sample port, producing a different response in the absorption than the broad leaves. This is especially interesting when the cross-sectional shape of the needles would result in low scattering angles, which is reported to increase the mentioned effect (Nilsson et al. 2011). In Nilsson et al. (2011), a diffuser between the sample and the integrating sphere was used during T measurements to minimize this apparent absorption problem in low-angle scattering samples. The results showed an

improvement on the accuracy of transmittance in glass samples but to the best of our knowledge the technique has never been applied to real leaves.

For the objective of this paper, we recommend to use the sample holder setup of Scenario 2 in order to compensate for the sample holder effect when using a single-beam integrating sphere with external sample ports as the one used in our experiment.

Table 3.2 RMSE of *broad-leaf* measured signal per sample holder scenario. These are results from Equation 3.3. The results from Scenarios 3 and 4 are equal to Scenarios 1 and 2, respectively.

Symbol	Flat plastic uncut broad-leaf samples		Silicon uncut broad-leaf samples	
	Scenario 1	Scenario 2	Scenario 1	Scenario 2
RMSE R_{uncutSH}	0.01	0.01	0.02	0.01
RMSE T_{uncutSH}	0.03	0.02	0.07	0.04

3.3.2 Effect of the multiple scattering between neighbor needles

The multiple-scattering hypotheses regarding the influence of the needle cross-section shape and the distance between the needles are testing two steps of our measuring method: the first is the sample scanning required for the $Digital_{GF}$ estimation ($RMSE_{gf_{DI}}$, Equation 3.7), and the second is the sample optical measurements ($RMSE_{gf_{TI}}$, Equation 3.8).

Results from $RMSE_{gf_{DI}}$ (Figure 3.5a, left graph) showed that samples with rhomboidal cross-section needles (Rh) have higher errors in their $Digital_{GF}$ than flat (F) and squared scenarios (S) regardless of the gap distance: 10% average error in Rh versus 2%–3% in F and S . The highest error among the rhomboidal cross-section scenarios appeared at the shortest distances ($RhI=0.5$ mm), whereas no pattern on the error variation with gap distance is found in the flat or squared cross-section types. The $Digital_{GF}$ estimation from the digital scanned images is based on applying a threshold to discriminate the needle pixels from the air gap pixels. Thus, the accuracy, at which the needle-air edges are estimated, determines the quality of the $Digital_{GF}$ output. This accuracy is determined by the selected combination of scanning and processing settings. The optimization efforts in Appendix II showed that the optimal settings can improve yet not eliminate the difference between the $Digital_{GF}$ and the theoretical reference ($Ideal_{GF}$). Majority of per-scenario comparisons between $Digital_{GF}$ and $Ideal_{GF}$ values did not show any

statistically significant differences ($P < 0.05$). The only exceptions were the rhomboidal cross-section scenarios: *Rh1* and *Rh2* in reflectance and *Rh1* and *Rh3* in transmittance measurements. These four scenarios, having significant differences between $Digital_{GF}$ and $Ideal_{GF}$ values, correspond with the two largest reflectance and transmittance $RMSE_{gf_{DI}}$ values, respectively. Comparison of the scenarios in Figure 3.5b revealed that $Ideal_{GF}$ of the rhomboidal cross-section scenarios (*Rh*) were on average about 8% lower than in the other cross-section scenarios (*F* and *S*), where the values were equal. This was expected, since the flat (*F*) and squared (*S*) cross-section needles have the same needle projected area and logically the same $Ideal_{GF}$ for the same measurement area; in the rhomboidal needle scenarios, the needle projected area is larger, and therefore the fraction of gaps and the $Ideal_{GF}$ are smaller. The $Digital_{GF}$ variation did not follow the same trend. For the flat (*F*) and squared (*S*) cross-section scenarios, $Digital_{GF}$ values remained almost similar to the $Ideal_{GF}$ with a 1% difference (Figure 3.5b), attributed to measuring errors (e.g., *BEHD*). $Digital_{GF}$ of the rhomboidal cross-section scenarios were 4% lower than in the other cross-section scenarios (*F* and *S*), except for the smallest gap distance scenario ($Rh1=0.5$ mm) where it was 4% higher. This explains the higher $RMSE_{gf_{DI}}$ (Equation 3.7) occurring at the rhomboidal cross-section needle scenarios and suggests that the cross section of the needle elements modulates the scanner light in a way that cannot be compensated by optimizing the scanning or image processing settings. The small differences shown between flat and squared cross-section scenarios imply that differences in the OPs of the material used to simulate the needles (flat plastic *versus* the silicon) are not as important as the cross section. The incident light direction during the scanning of rhomboidal cross-section needles is different from the normal to the needle surface producing a longer photon path and inducing more interactions of the photons between neighboring needles. Consequently, the rhomboidal needles appear in the scanned image optically thinner than in reality, which results in a less accurate estimation of their projected needle area. The second error source contributing to the higher $RMSE_{gf_{DI}}$ of the rhomboidal cross-section needle scenarios is the *BEHD*, which we expected to be more pronounced in the smallest gap distance scenario ($Rh1=0.5$ mm).

In summary, we observed that: 1) the hypothesis regarding the needle cross-section influence is true for the rhomboidal cases and 2) the hypothesis regarding the needle air gaps is true only if combined with the rhomboidal cross section. For the other scenarios, effective scanning and processing

settings were found through the optimization (Appendix II). Best results were achieved for the smallest distance, except for rhomboidal cross section, where 0.5 mm represents less than half-the-needle width. This indicates that the distance smaller than half-the-needle width potentially reinforces the multiple scattering effects between needles. Finally, the difference between $Digital_{GF}$ in reflectance and transmittance per scenario showed no statistically significant difference ($P < 0.05$), except for the $F1$ scenario, where the bias is attributed to measuring errors.

$RMSE_{gf_{TI}}$ (Equation 3.8) provides results related to the multiple scattering during the spectral measurements performed in the integrating sphere. Different cross-section shapes and distances between the needles induce different scattering behaviors of the interacting photons, which are expected to result in discrepancies between the $True_{GF}$ and the $Ideal_{GF}$ values. Additionally, the $BEHD$ is expected to contribute to the overall error, especially in the nonflat cross-section and/or small gap distance scenarios. Likely, the applicability of $True_{GF}$ to the rhomboidal cross-section samples is limited by the fact that the thickness of their cross section is not constant. Compared to the needle with 1-mm thick squared cross section, thickness in the rhomboidal needle is 1.41 mm for the central part and decreasing toward the edges. The volume determining the optical thickness of both silicon needle types is, however, equivalent. We assume that a higher absorption rate in the central part of a rhomboidal needle is compensated by a lower absorption at thinner edges. Moreover, for wavelengths where absorption is low and scattering dominates the measured signal, difference in thickness is less important than difference in cross-section shape ruling the scattering. Scattering (i.e., albedo W_{needle}) between 500 and 1700 nm is on average higher than needle absorption (A_{needle}). The concept of $True_{GF}$ is, therefore, considered as applicable in this wavelength range also for the rhomboidal cross-section scenarios.

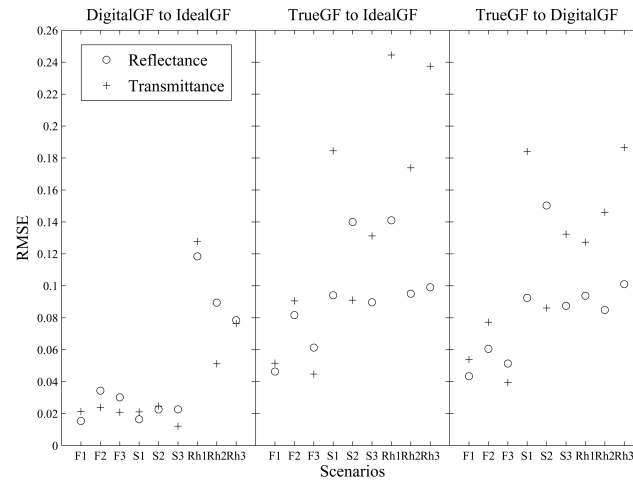
Comparison of $True_{GF}$ against $Ideal_{GF}$ values showed a statistically significant difference for all scenarios ($P < 0.05$) except the transmittance of rhomboidal cross-section $Rh1$. When comparing the cross-section scenarios of the same gap distance (e.g., $F2$, $S2$, and $Rh2$), the error generally increased from flat to squared to rhomboidal cross section (Figure 3.5a, middle graph), which supports our hypothesis 1). This trend is produced by the $True_{GF}$ values, which, especially in transmittance, tend to increase from F to S to Rh in most cases (Figure 3.5b). The $S2$ error in reflectance, which is higher than $Rh2$, and also equal errors of $F2$ and $S2$ in transmittance are not following this general

trend. These exceptions are caused by the $Ideal_{GF}$ value, which, being by definition equal in F and S , is distorting the trend. The $True_{GF}$ variation explicitly indicates the existence of the multiple scattering effects due to the cross-section shape, especially when comparing F and S cases. If there is no influence from the multiple scattering, $True_{GF}$ values of F and S cases should be theoretically similar, as it occurs with the $Ideal_{GF}$. The results, however, show that $True_{GF}$ is not defined only by the geometry of the sample, but also by the scattering processes triggered by this geometry during the optical measurements. Concerning the second hypothesis about the gap distance, error tendency in the F cross-section scenarios differs from the nonflat (S and Rh) ones. In the flat scenarios, the error does not follow the expected trend of increasing error with decreasing needle gap distance. The highest deviation (9%) occurs at gap distances of 1 mm ($F2$), while more similar values occur for $F1$ and $F3$ cases. As expected, the highest errors of the nonflat scenarios appear at the narrowest gap distances ($S1$ and $Rh1$; 0.5 mm), except in reflectance of the S cases where error behavior is similar to the one found for F scenarios. We can, therefore, conclude that the best results are achieved with the smallest distance of 0.5 mm in flat cross-section scenarios, while the opposite occurs in the nonflat cases, where the error is generally higher for Rh needles, especially in transmittance. Since 0.5 mm in Rh cross-section scenarios is less than half-the-needle width, the multiple scattering of photons seems to be reinforced by a too small distance between the needles. In addition, the error variation between the reflectance and transmittance is of 1% for the same flat cross-section scenarios, whereas, in the nonflat cases, the transmittance error values are much higher than the reflectance errors: 5% higher for the squared cross-section scenarios (S) and 10% for rhomboidal (Rh). These results imply that the cross-section effect appeared to have a greater influence than the gap distances tested in this study, especially for transmittance measurements (average variation of the error due to the cross section is about 14% compared to the 3% variation due to the gap distance).

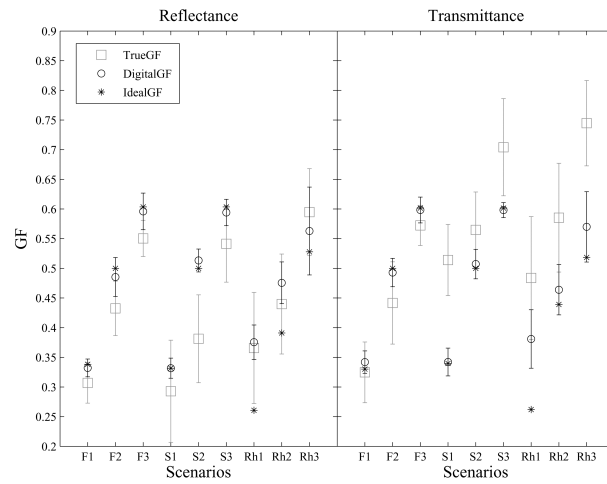
If we look at the difference between the $True_{GF}$ and $Ideal_{GF}$ values per scenario (Table 3.3), we observe a systematic overestimation of the needle transmittance happening in the nonflat cross-section scenarios. The fact that the GF-corrected T_{needle} , computed using the most accurate GF available (i.e., $Ideal_{GF} \pm BEHD$), did not reproduce the “nongap” reference ($T_{uncutSH}$) indicates that the multiple scattering between nonflat needles contributes to the transmittance signal recorded in the integrating sphere.

Table 3.3 Influence of needle cross-section shape on the GF-correction formulae performance. (*) The standard deviation range (error bars in Figure 3.5b) overlaps with value $Ideal_{GF}$ value.

Cross-section scenario	Relationship (Figure 5.3b)				GF-correction output
	Reflectance (R)		Transmittance (T)		
Flat (F)	$True_{GF} < Ideal_{GF}$	$R_{needle} \geq R_{uncutSH}$	$True_{GF} \leq Ideal_{GF}$	$T_{needle} \leq T_{uncutSH}$	R overestimated T underestimated (*)
Squared (S)	$True_{GF} \leq Ideal_{GF}$	$R_{needle} \geq R_{uncutSH}$	$True_{GF} > Ideal_{GF}$	$T_{needle} > T_{uncutSH}$	R and T overestimated
Rhomboidal (Rh)	$True_{GF} \geq Ideal_{GF}$	$R_{needle} \leq R_{uncutSH}$	$True_{GF} > Ideal_{GF}$	$T_{needle} > T_{uncutSH}$	R underestimated (*) T overestimated



(a)



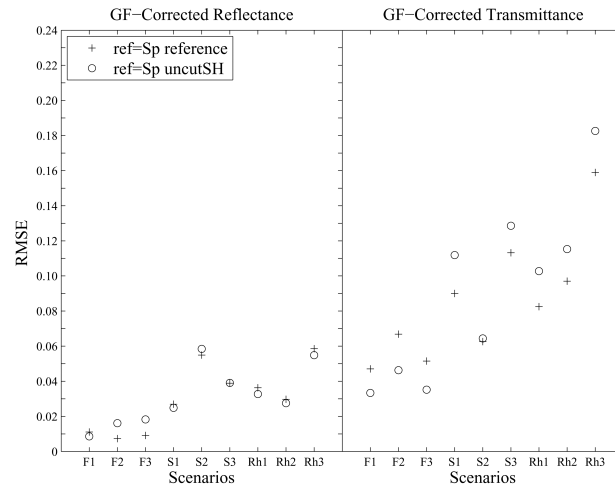
(b)

Figure 3.5 (a) RMSE computed between: 1) $Digital_{GF}$ of the best scanning and image processing settings and corresponding $Ideal_{GF}$ ($RMSE_{gf_{DI}}$, Equation 3.7; left graph); 2) $True_{GF}$ and corresponding $Ideal_{GF}$ ($RMSE_{gf_{TI}}$, Equation 3.8; middle graph); and 3) $True_{GF}$ and corresponding $Digital_{GF}$ ($RMSE_{gf_{TD}}$, Equation 3.9; right graph). RMSE is computed for the wavelength range 450–1700 nm. Labels $F1$, $F2$, $F3$, $S1$, $S2$, $S3$, $Rh1$, $Rh2$, and $Rh3$ on x-axis correspond to the *standard-needle-sample* scenarios. Part (b) presents the average GF values (\pm standard deviation) per needle-sample scenario for reflectance (left graph) and transmittance (right graph).

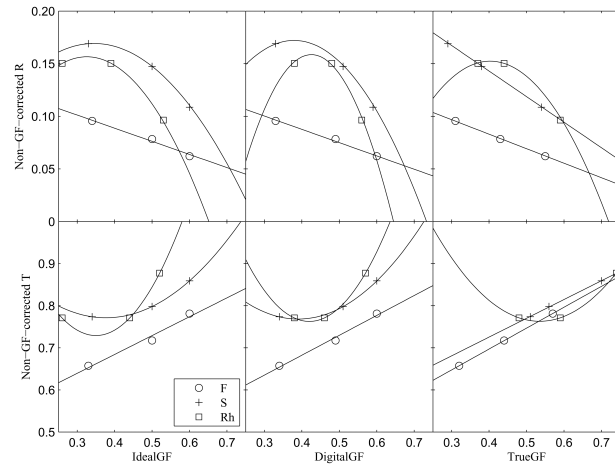
The results of $RMSE_{gf_{TD}}$ (Equation 3.9) in Figure 3.5a (right graph) show a pattern that is similar to $RMSE_{gf_{TI}}$, especially in the flat (F) and squared cross-section scenarios (S). This suggests that the $BEHD$, which is not present in $RMSE_{gf_{TD}}$, does not have a crucial effect on our $Ideal_{GF}$ values. A higher influence of the $BEHD$ and also of the light scattering effect during the sample scanning can be seen in the rhomboidal cross-section (Rh) scenarios, where $RMSE_{gf_{TD}}$ was reduced with respect to $RMSE_{gf_{TI}}$, especially for the smallest gap distances ($Rh1$). When comparing $True_{GF}$ and $Digital_{GF}$ values per scenario, a statistically significant difference ($P < 0.05$) was found for most cases, except $F1$, $Rh1$, and $Rh3$ in reflectance and $Rh1$ in transmittance. High overlap of variation ranges (i.e., mean \pm standard deviation; Figure 3.5b) can explain the similarities found in these cases between $Digital_{GF}$ and $True_{GF}$. Finally, Figure 3.5b illustrated a good agreement between the $Digital_{GF}$ and the $True_{GF}$ reflectance values, whereas the transmittance $True_{GF}$ values are on average 12% higher than the $Digital_{GF}$ estimations, which are caused mainly by the above-discussed contribution from the multiple scattering during the optical measurements.

3.3.3 Validation of OPs after GF correction

Mean individual needle-leaf directional-hemispherical R_{needle} and T_{needle} per spectral waveband computed using *Mesarch's* formulae for GF correction (Equation 3.1 and 3.2) were compared to the two available corresponding references (average of 10 samples): 1) the broad-leaf R or T for the best sample holder scenario ($R_{uncutSH}$ or $T_{uncutSH}$); and 2) the broad-leaf R or T measured without sample holder ($R_{reference}$ or $T_{reference}$). The results from case 1) (Figure 3.6a) show that the error in transmittance was on average 3% higher than in reflectance for the flat cross-section scenarios (F) and 7%–10% for the nonflat (S and Rh) scenarios. Statistical analysis revealed no significant difference ($P < 0.05$) between R_{needle} and $R_{uncutSH}$ (except for $F2$, $F3$, $S2$, and $Rh2$), whereas the difference between T_{needle} and $T_{uncutSH}$ was significant (except for $F1$, $F2$, and $F3$). As expected, for the same gap distance, error tended to increase in the direction flat-squared-rhomboidal cross sections. Among the same cross-sections and opposite to the expected trend, the error tended to increase from the smallest gap distance (gap scenario $l=0.5$ mm) to the widest (gap scenario $3=1.5$ mm), especially for the nonflat (S and Rh) cases. As already stated in Section 3.3.2, this suggests that half-the-needle width, i.e., 0.5 mm, might be the optimal distance-between-needles at which signal is still negligibly affected by multiple scattering induced by too-close neighbour needles. Conversely, the one-and-half-needle width of 1.5 mm is to be considered as too big.



(a)



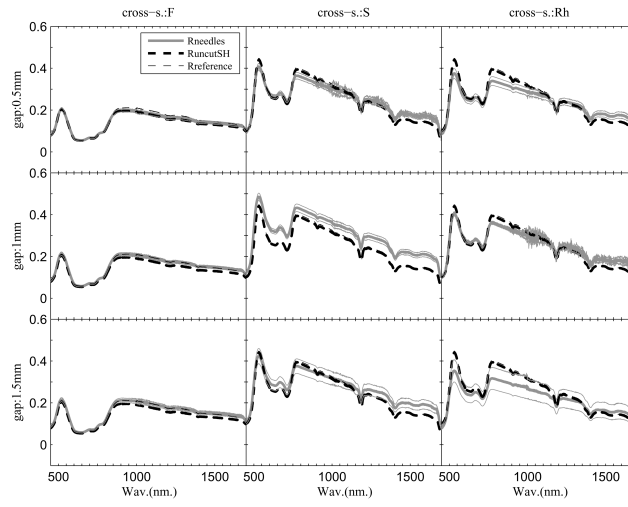
(b)

Figure 3.6 (a) RMSE in Equation 3.10 computed for GF-corrected reflectance (R_{needle} ; left graph) and transmittance of individual needles (T_{needle} ; right graph) toward two corresponding reference spectra: 1) reference $R_{reference}$ or $T_{reference}$, i.e., R or T spectral signal of the *broad-leaf* measured with no sample holder (“ref=sp_{reference}”); and 2) reference $R_{uncutSH}$ or $T_{uncutSH}$, i.e., R or T spectral signal spectral signal of the *broad-leaf* (uncut) measured in the best sample holder scenario (“ref=sp_{uncutSH}”). The labels $F1$, $F2$, $F3$, $S1$, $S2$, $S3$, $Rh1$, $Rh2$, and $Rh3$ in the x-axis represent the nine *standard-needle-sample* scenarios. (b) Curve fitting of nonGF-corrected reflectance and transmittance (y-axes) versus GF values (x-axes) per scenario (F , flat cross-section; S , squared cross-section; and Rh , rhomboidal cross-section). R^2 results from fitting are presented in Table 3.4.

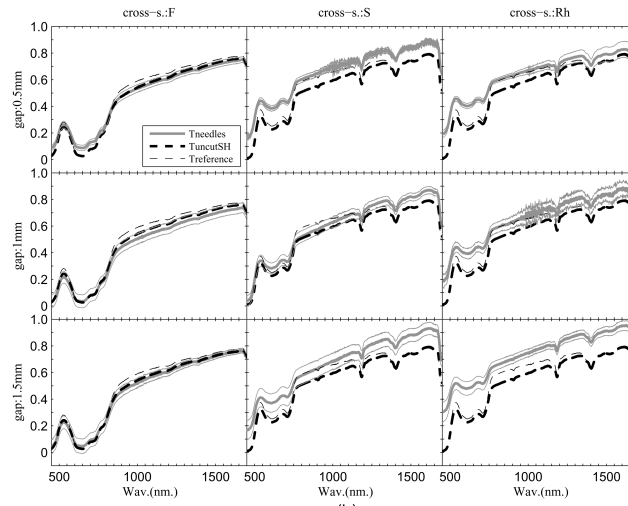
Nevertheless, although, the results in Section 3.3.2 showed that GF errors in rhomboidal cross section (where 0.5 mm represents less than half-the-needle width) were higher than in other cross sections, this effect is not as obvious in the GF-corrected signal. One possible reason is that the difference between half-width for rhomboidal needles (0.7 mm) and 0.5 mm is so small that while the GF values are sensitive to it, the spectra after GF correction are not. Exceptionally, the values at gap-distance scenario 2 (1 mm) did not follow the previous pattern and differed per cross-section case. No apparent reason could be found for this exception; therefore, more measurements with a wider range of distance scenarios are recommended for future analyses. Finally, the error variation associated with increasing gap tended to be smaller than the error variation associated with cross section (about 1% smaller in reflectance and 5% in transmittance). Thus, and in line with the results shown in Section 3.3.2, cross-section effect appeared to have a greater influence than the gap distances tested in this study.

These results can be explained by analyzing the GF-corrected needle signal shown in Figure 3.7. The GF-corrected R_{needle} signal tends to be overestimated in the flat and squared cross section but underestimated in the rhomboidal, and conversely, T_{needle} is underestimated in the flat whereas overestimated in the nonflat cases. These results per scenario are in line with the ones shown in Table 3.3. In addition, the higher deviation from the reference occurring in the nonflat cross-section scenarios, especially in transmittance, is obvious. The underestimation of T_{needle} in the flat needles was expected since Mesarch et al. (1999) reported it after their analysis performed on flat “film-strips” needles. This suggests that even though we optimized the GF estimation for this type of needles, the method is still producing an inherent measurement error. The overestimation of T_{needle} in nonflat needles indicates that the increase in recorded signal due to the multiple scattering is such that even the overcorrection originating from the *Mesarch*'s formulae is not able to compensate for it.

In case 2), the error values in reflectance are the same as in case 1) [except 1% decrease on the flat cross-section cases at 1 mm (*F2*) and 1.5 mm gap distances (*F3*)]. In transmittance, a systematic 2% error increase occurring in the flat cross-section scenarios contrasted with an approximate 2% error decrease in the nonflat cross-section scenarios (Figure 3.6a). The error increase in the flat cross-section scenarios can be attributed to the effect of the sample holder (2%; Table 3.2), since this effect is included in case 2). However, in the nonflat cross-section scenarios, the sample holder effect (4%; Table 3.2) does not induce an increase in the error compared to case 1) but a decrease, therefore, improves the total error.



(a)



(b)

Figure 3.7 Average directional-hemispherical reflectance (a) and transmittance (b) spectra from: 1) individual needle leaves, computed after the GF-correction through *Mesarch's* formulae (R_{needle} (Equation 3.1)) and T_{needle} (Equation 3.2)); 2) from the broad-leaf measured according to the best sample holder scenario ($R_{uncutSH}$ or $T_{uncutSH}$); and 3) from the broad-leaf measured without sample holder ($R_{reference}$ and $T_{reference}$).

Overall, the final error achieved after optimizing *Mesarch's* method is about 1% in reflectance and 5%–7% in transmittance if the needles are flat. The error increases up to 3%–5% in reflectance and 9%–12% in transmittance for squared cross-section needles (*S*) and up to 4%–6% in reflectance and 9%–17% in transmittance for rhomboidal cross-section needles (*Rh*).

Finally, a function fitting analysis was applied per cross-section scenario to assess if the relationship between nonGF-corrected OPs (i.e., R_{TOTAL} and T_{TOTAL}) and the sample GF is linear (Mesarch et al. 1999). The flat cross-section (*F*) scenario follows the expected linear relationship, whereas in the nonflat cross-section cases (*S* and *Rh*), the relationship is closer to a polynomial function of second degree, especially for the *Rh* case (Table 3.4 and Figure 3.6b). The nonlinear relationship between nonGF-corrected signal and GF supports our hypothesis about the interaction between needles in the nonflat cases. Consequently, irrespective from the various method errors (i.e., optical measurements and GF estimation through scanning and digital image processing), *Mesarch's* algorithms have a lower accuracy for nonflat cross-section needles, because the multiple scattering effects are not taken into account. Nevertheless, more measurements, testing other gap distances, and perhaps ray tracing computer simulations are needed to solidify this finding.

Table 3.4 Function fitting analysis of R_{TOTAL} and T_{TOTAL} versus GF. Linear: $y(x)=ax+b$. Pol. 2: corresponds to polynomial of second degree: $y(x)=ax^2+bx+c$.

Cross-section	Fitted model		R ² for fitting y versus x	
<i>F</i>	Linear	$x=I_{ideal_{GF}}$	0.99	0.97
	Pol. 2		1	1
	Linear	$x=D_{igital_{GF}}$	0.99	0.99
	Pol. 2		1	1
	Linear	$x=T_{rue_{GF}}$	1	1
	Pol. 2		1	1
<i>S</i>	Linear	$x=I_{ideal_{GF}}$	0.91	0.87
	Pol. 2		1	1
	Linear	$x=D_{igital_{GF}}$	0.86	0.83
	Pol. 2		1	1
	Linear	$x=T_{rue_{GF}}$	1	1
	Pol. 2		1	1
<i>Rh</i>	Linear	$x=I_{ideal_{GF}}$	0.77	0.54
	Pol. 2		1	1
	Linear	$x=D_{igital_{GF}}$	0.69	0.82
	Pol. 2		1	1
	Linear	$x=T_{rue_{GF}}$	0.90	0.82
	Pol. 2		1	1

3.4 Conclusion

In this study, we performed comprehensive uncertainty analyses of the method developed by *Mesarch* for measuring coniferous needle-leaf OPs. Our study focused on the following measurement aspects: 1) the effect of a sample holder used to support the needles during the measurements, and 2) the effect of the multiple scattering in between the measured artificial needle leaves.

Analysis of the sample holder effect showed an average underestimation of the needle transmittance signal of 2% in flat needles and 4% in non-flat needles [based on the RMSE according to Equation 3.3]. The results on the sensitivity of the digitally estimated GF to the image acquisition and image processing settings showed that optimization of these settings reduced the deviation considerably, producing a negligible error. However, in spite of using the most optimal settings, multiple scattering between artificial needles was still affecting the digital GF estimation, resulting in average errors of only 2%–3% in samples with flat and squared cross-section needles, but of about 10% in samples with rhomboidal cross-section needles.

The last case showed a clear overestimation of the digital GF, especially when the needles were as close to each other as 0.5 mm, which is for needles of rhomboidal cross section less than half-the-needle width. This indicates that half-the-needle width is a threshold at which the multiple scattering between the needles is reinforced and biases the measurement.

The results of our sensitivity analysis scenarios suggest that the needle cross-section might have a stronger negative effect on the needle-leaf OPs than the needle gap distance. The multiple scattering between artificial needles also affected the signal recorded during the optical measurements, causing higher deviations of nonflat needle samples, particularly in transmittance.

The needle transmittance corrected for the GF using *Mesarch's* formulae was about 10%–20% higher than the “nongap” (broad-leaf) reference. In addition, the relationship between the nonGF-corrected signal and GF is nonlinear in rhomboidal cross-section needles. This suggests that the rhomboidal cross section induces multiple interactions of the incoming light with sample needles, which is distorting the expected linear relationship otherwise observed in flat needles (*Mesarch et al. 1999*).

For this reason, *Mesarch's* formulae, based on the assumption of a linear GF correction, are inaccurate in computing the OPs of nonflat needles. Overall, the final error achieved after optimizing the image scanning and processing settings was about 1% in reflectance and 5%–7% in transmittance

for flat needles. The error increased up to 3%–5% in reflectance and 9%–12% in transmittance for squared cross-section needles, and even up to 4%–6% in reflectance and 9%–17% in transmittance for rhomboidal cross-section needles.

In general, more accurate OPs can be achieved when the distance between measured needles is about half the needle width (i.e., 0.5 or 0.7 mm in our cases). The results of this study pointed out that approaches designed to measure more comprehensively OPs of nonflat coniferous needle samples should take into account multiple scattering between the measured leaves as currently done in radiative transfer modeling.

Appendix I

Technical details about the sample holder configurations are presented in Figure 3.8. Computation of R_{TOTAL} in Equation 3.1 and T_{TOTAL} in Equation 3.2 was done through the algorithms recommended by the sphere manufacturers:

$$R_{TOTAL}(\lambda) = \left(\frac{R_{sample}(\lambda) - STR_{RefI\text{mode}}(\lambda)}{REF_{RefI\text{mode}}(\lambda) - STR_{RefI\text{mode}}(\lambda)} \right) \cdot R_r(\lambda) \quad (3.11),$$

and

$$T_{TOTAL}(\lambda) = \left(\frac{T_{sample}(\lambda) - STR_{Trans\text{mode}}(\lambda)}{REF_{Trans\text{mode}}(\lambda) - STR_{Trans\text{mode}}(\lambda)} \right) \cdot R_r(\lambda) \quad (3.12),$$

where $R_r(\lambda)$ is the reflectance of the calibrated reference standard at wavelength λ and the other inputs are explained in Table 3.1. Each measured input represented an average of 100 spectral scans.

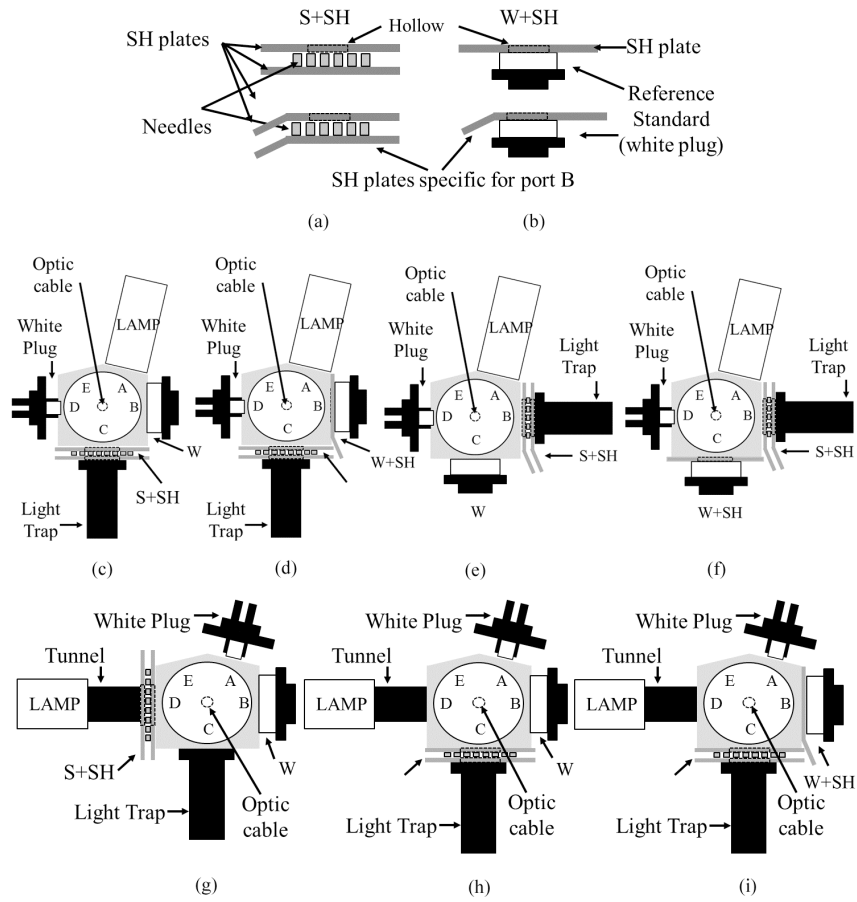


Figure 3.8 Examples of sample holder configurations: (a) top view of “S+SH” described in Table 3.1 (two sample holder plates and the needles in between); (b) top-view of “W+SH” (Table 3.1); (c)–(f) show a top view of the ASD integrating sphere for reflectance mode configurations: (c) R_{sample} (Table 3.1) for Scenario 1; (d) R_{sample} (Table 3.1) for Scenario 2; (e) $REF_{Ref.mode}$ (Table 3.1) for Scenario 1; (f) $REF_{Ref.mode}$ (Table 3.1) for Scenario 2; (g)–(i) show a top view of the ASD integrating sphere for transmittance mode configurations: (g) T_{sample} (Table 3.1) for Scenario 1 and 2; (h) $REF_{Trans.mode}$ (Table 3.1) for Scenario 1; (i) $REF_{Trans.mode}$ (Table 3.1) for Scenario 2. Port E has the white plug in all configurations (not shown).

Appendix II

Optimization of scanning and processing settings for digital GF estimation

The $Digital_{GF}$ is defined as the ratio of the number of air gap pixels inside the measured (i.e., illuminated) area of a needle sample to the total number of pixels inside the measurement area (number of needle pixels + gap pixels, represented by the empty scanned mask). Computation of the $Digital_{GF}$ required masking and scanning each needle sample and subsequently processing the digital output image. The total number of air-gap pixels in the digital image was calculated by applying a “white-pixel-threshold” to discriminate gap pixels from needle pixels (Mesarch et al. 1999). The optimal scanning settings (resolution (r), brightness (b) and contrast (c)) and the “white-pixel-threshold” values (t) were identified by conducting two sensitivity analyses. For the first one, we built three *1-needle-sample* scenarios, one per needle cross-section shape available in our study (i.e., flat- F , squared- S , and rhomboidal- Rh). Each sample (5 per scenario) was composed of only 1 needle element, which was carefully placed inside the sample holder at a known distance from the center of the holder aperture. We scanned each masked (1-needle) sample applying 300 *scan-settings* scenarios defined by the varying scan r - b - c combination (Table 3.5, first sensitivity analysis). All scans were saved as 8-bit-gray scale digital images and each of them subsequently processed to estimate the $Digital_{GF}$. The processing was performed for each scan, according to 49 *image-processing* scenarios, where the “white-pixel-threshold” (t) was varying between 5.1 and 249.9 (corresponding to values within the range of an 8-bit-gray scale digital image -0 to 256- selected in 2% steps). $Ideal_{GF}$ and $Digital_{GF}$ were computed per *1-needle-sample* scenario from each scan. The sensitivity of the $Digital_{GF}$ to the scanning and image-processing settings was analyzed with Equation 3.13 for all r - b - c - t combinations by varying one of the four parameters at a time and fixing the others at their minimum, median and maximum value:

$$\varepsilon T(s,i,r,b,c,t) = \left| \frac{Digital_{GF}T(s,i,r,b,c,t) - Ideal_{GF}T(i)}{Ideal_{GF}T(i)} \right| \quad (3.13),$$

where $Digital_{GF}T(s,i,r,b,c,t)$ is the GF estimated for the standard-needle-sample scenario i ($i=1,\dots,9$), from the digital image of sample s ($s=1,\dots,5$), which was scanned and processed with the T mask for scan-settings scenario r - b - c (r - b - $c=1,\dots,300$) and image-processing scenario t ($t=1,\dots,49$); the $Ideal_{GF}T(i)$ is the corresponding $Ideal_{GF}T$ for the same i . No significant differences are expected

between the resulting $Digital_{GF}T$ and $Digital_{GF}R$ for a sample of the same $r-b-c-t$ combination, because there is no repositioning of the needles inside the sample holder when measuring and scanning a sample in T and R mode. Only the size of the illuminated area differs slightly during the OPs measurements, which translates into the use of T and R specific masks during the scanning and digital image processing. Following this rationale, the sensitivity analysis was performed only for T scans (i.e., samples with T mask). The $BEHD$ in the 1 -needle samples is expected to be almost negligible (it is feasible to position a single needle in the sample holder with the desirable precision). Therefore, this ϵT is used as the best indicator of the error inherited from the GF estimation via digital image processing.

Based on the results from the first sensitivity analysis, we performed a *second sensitivity analysis* applied on all samples corresponding to the nine needle sample scenarios ($F1, F2, F3, S1, S2, S3, Rh1, Rh2$, and $Rh3$). Here, we used the optimal 3 *scan-settings scenarios* identified within the previous extensive sensitivity analysis (Table 3.5, first sensitivity analysis) and all scans were digitally processed according to the same 49 *image-processing scenarios* used in the first sensitivity analysis. The effect of the GF estimation through scanning and image processing for each $r-b-c-t$ combinations was analyzed through Equation 3.13 as in the first analysis. Following the same logic used in the first sensitivity analysis, this *second sensitivity analysis* was carried out only for T scans (using T mask) and subsequently the resulting optimal $r-b-c-t$ per scenario were used to compute the final $Digital_{GF}T$ and $Digital_{GF}R$ per sample per scenario.

Table 3.5 Scanning and image-processing scenarios for GF digital computation. *p.p.i.*, pixels per inch; *n.a.*, not applicable..

1st sensitivity analysis: 1-needle-sample scenarios (F, S, Rh cross-section scenarios)			
Scenario	Quantity	Units	Values
Scan-settings	Resolution (r)	p.p.i.	800, 1200, 2400
	Brightness (b)	%	0-100 in steps of 10%
	Contrast (c)	%	0-100 in steps of 10%
Image processing	White-threshold (t)	n.a.	0-256 in steps of 2%
2nd sensitivity analysis: standard-needle-sample scenarios (F1, F2, F3, S1, S2, S3, Rh1, Rh2, and Rh3)			
Scenario	Quantity	Units	Values
Scan-settings	$r-b-c$	p.p.i.; %; %	1) 800-0-0
			2) 2400-100-0
			3) 2400-100-100
Image processing	White-threshold (t)	n.a.	0-256 in steps of 2%

As explained in Section 3.2.4, potential differences are expected in the optimal r - b - c - t settings per scenario due to variations in the scattering behavior of the scanner light caused by the different needle cross-section shapes and distance between needles. These scattering effects might result in different sharpness of the needle element edges in the scanned digital images forcing the need for specific optimal settings per scenario.

Effect of the GF estimation through digital image processing

The results from the first sensitivity analysis (i.e., *1-needle-sample* scenarios, Table 3.5) showed that the deviation of the $Digital_{GF}$ from the $Ideal_{GF}$ expressed through Equation 3.13 followed a similar pattern among the three available cross-section scenarios, with higher values in the rhomboidal cross section (Rh) than in the flat (F) and squared (S) ones, where the values are similar. Regardless of the scanning settings, the maximum error appeared always when the image-processing threshold (t) was fixed at the minimum value, with error values being: 19(3)% for flat (F) and squared (S) cross-section scenarios; and 28(4)% in rhomboidal (Rh) ones (numbers between brackets refer to the standard deviation). Conversely, if the threshold was not fixed at its minimum, error decreases to 1(0.3)% 4(1)% in rhomboidal scenario, irrespective of the other parameters. If the scanning settings were fixed at their minimum or median values, the error variation with increasing threshold showed an inflexion point (exact value differs per scenario) from which lower threshold values trigger the maximum error. Threshold values above the inflexion point caused error drops of 20% in the flat (F) and squared (S) scenarios and of almost 30% in the rhomboidal (Rh) ones, resulting in a stable error value ($< 4\%$). The optimal threshold value (i.e., for minimum error) differed per scenario and produced minimum errors of 0.1%. If the scanning settings were fixed at their maximum, error values stayed stable for all thresholds but increased among the cross-section scenarios: 1% for the flat scenario (F); 2% for the squared cross section (S); and 7% for the rhomboidal (Rh) one. Thus, the main findings from the first sensitivity analysis are: 1) the reliability of the $Digital_{GF}$ is mainly driven by the threshold value; 2) needles cross section affects the image processing and thus optimal threshold differs per scenario, as expected; and 3) selection of the proper threshold can ensure a negligible effect of the GF estimation through scanning and image processing (0.1%).

Based on the higher sensitivity of the $Digital_{GF}$ to the threshold value, the *scan-setting scenarios* were optimized to the best three combinations, whereas the 49 *image-processing scenarios* (threshold values) remained unchanged during the second sensitivity analysis (Table 3.5). The results here showed

that, similarly to the *first sensitivity analysis*, variation of the error according to the scanning settings followed a similar pattern in all the nine needle-sample scenarios, with a bigger deviation in the rhomboidal cross-section scenarios than in the flat (*F*) and squared (*S*) ones. The error here appeared to be also driven by the threshold value. Thus, the scanning settings (*r-b-c*) combination corresponding to a resolution of 800 ppi, and 0% contrast and brightness (800–0–0) was selected and fixed in further analysis, aiming to standardize the technique involving the lowest requirements possible, i.e., 800–0–0 settings are easily available in common and low-cost scanners.

For this scanning setting (800–0–0), the error variation with increasing threshold (values from 5.1 to 249.9) showed also an inflexion point, below which lower threshold values triggered errors above 100%. This point differs per scenario covering 30% of the lowest threshold values among the available range (5.1–249.9), i.e., from 0 to 77 (absolute *t* values per scenario in Table 3.6). For thresholds above the critical value, the following patterns were observed: 1) for the same gap-distance scenarios (e.g., *F1*, *S1*, and *Rh1*), the effect of the needle cross section triggered higher errors in the rhomboidal cross-section scenarios (*Rh*) and similar in the flat (*F*) and squared (*S*) ones; 2) for the same cross-section scenarios (e.g., *F1*, *F2*, and *F3*), the effect of the gap distance between needles showed that errors tended to be higher at gap distance Scenario 1 (0.5 mm, e.g., *F1*) and lowest at gap distance Scenario 2 (1 mm, e.g., *F2*), closely followed by values at Scenario 3; and 3) for the same threshold value, the error corresponding to a certain needle sample scenarios was higher than at the corresponding *1-needle-sample* scenario (e.g., *Rh1*, *Rh2*, or *Rh3* versus *Rh 1-needle scenario*). This difference was higher in the rhomboidal cross-section scenarios (*Rh*). These three error patterns support our hypotheses about the *BEHD* increase, except for the slightly lower error in gap Scenario 2 (1 mm) instead of in 3 (1.5 mm).

As expected, the optimal threshold, i.e., the value giving the lowest error per needle-sample scenario, differed per scenario (Table 3.6). Similarly, if we compared results from a *needle-sample* scenario with its corresponding *1-needle-sample* scenario (e.g., *S1*, *S2*, and *S3* standard-needle sample scenarios versus *S 1-needle sample*), we found not only an increase in the error in the first ones, but also a change in the optimal threshold value. This supports the hypothesis concerning the effect of the needle cross-section shape and gap distance on the multiple scattering of the scanner light. In *1-needle-sample* scenarios, where *BEHD* is assumed to be negligible, for a different material (flat plastic *versus* silicon), the optimal *t* value is different because of differences in the material properties. Also, for the same

material but different cross section (*S* and *Rh* *1-needle-sample* scenarios), photons from the scanner light will be hitting the needle surface at different incident angles (Figure 3.3h *versus* i), and scattered differently, which results again in different optimal values, due to differences in the needle-edge sharpness. The broader critical threshold value range observed in rhomboidal *1-needle-sample* scenario, where higher thresholds are needed to sharpen the image and reduce the error in the $Digital_{GF}$, also supports this. However, once the critical threshold value range is passed, the error stays stable for the three *1-needle-sample* scenarios no matter the cross-section shape, and the error can be negligible if the proper threshold value is selected in each scenario. Nevertheless, this is not the case when we increase the number of needles in the scanned area, as in the nine needle-sample scenarios. For the nine needle-sample scenarios, on top of the effect caused by material and cross-section shape differences, photons hitting the needle surface might be scattered toward neighbor needles, especially if they hit in a direction different from the normal to the needle surface (*Rh* cross section; Figure 3.3i) and if the needles are close to each other. This modulates the scanner light in a different way leading once more to changes in the optimal t value per scenario and resulting in higher errors, especially in case of rhomboidal cross-section needle scenarios ($RMSE_{gf_{Dt}}$, Equation 3.7 in Section 3.3.2).

Recommendations

We would like to finalize this section by giving some recommendations to potential users of this methodology. Differences per scenario on the optimal threshold make the standardization of the $Digital_{GF}$ estimation a complicated task, even enhanced in real needle samples due to the irregular shape and size of the needles. Based on our results, we recommend keeping the scanning settings (*r-b-c*) combination on 800–0–0 as a standard, since the error is driven by the threshold value. We also recommend selecting a threshold value higher than the first 40% values of the available range (5.1–249.9). In Table 3.6, we provide a selection of threshold value ranges corresponding to the minimum $\varepsilon T \pm a$ deviation of 1%. We recommend applying the threshold values corresponding to the closest cross-section shape available in Table 3.6 and leaving a gap distance between the needles similar to half-needle width, since the 0.5-mm gap- distance scenario appears to give the lowest error. As an example, for Norway spruce (*Picea abies* (L.) Karst.; rhomboidal cross section) or Scots pine needles (*Pinus sylvestris* L.; semicircular cross section), we would select the t values from the scenario *Rh* at 0.5-mm distance.

Finally, the selection of the threshold value range in this analysis is very specific and chosen to cover all possible values available in our 8-bit gray-scale digital images. Scanned images saved in formats other than 8-bit gray-scale might require an adaptation of the threshold range according to the same logic. Nevertheless, aiming to standardize the technique as much as possible, we provide all results concerning the threshold values as a % for the available range, 5.1–249.9 (i.e., instead of selecting the t value 249.9 select the value corresponding to 98% of the available range in the specific digital image, e.g., 16-bit gray scale). However, error propagation in a different range of t values has to be tested.

Table 3.6 Range of optimal threshold values per standard-needle-sample scenario. Resolution (r) =800 p.p.i., brightness (b) and contrast(c)=0% and the t values above correspond to the optimal r - b - c - t scan and image processing settings per scenario, used to compute the final $Digital_{GF}R$ and $Digital_{GF}T$ used to compute the OPs per scenario.

Scenario	Range of optimal t values (relative t in % for range 0-256)	Best threshold
<i>F1</i>	249.9 (98%)	
<i>F2</i>	137.7-234.6 (54%-92%)	204 (80%)
<i>F3</i>	96.9-193.8 (38%-76%)	147.9 (58%)
<i>S1</i>	249.9 (98%)	
<i>S2</i>	91.8-137.7 (36%-54%)	107.1 (42%)
<i>S3</i>	173.4-244.8 (68%-96%)	224.4 (88%)
<i>Rh1</i>	249.9 (98%)	
<i>Rh2</i>	204-239.7 (80%-94%)	219.3 (86%)
<i>Rh3</i>	249.9 (98%)	

Acknowledgements

The authors thank V. Kaplan, J. Hanuš (Global Change Research Centre AS CR, v.v.i, Brno, Czech Republic), and P. Lukeš (Department of Forest Sciences, University of Helsinki, Finland) for helping with the experimental setup, logistics, and data processing.

Chapter 4

A note on upscaling coniferous needle spectra to shoot spectral albedo

This chapter is based on:

Rautiainen, M., Mõttus, M., Yáñez-Rausell, L.*, Homolová, L., Malenovský, Z., & Schaepman, M.E. (2012). A note on upscaling coniferous needle spectra to shoot spectral albedo. *Remote Sensing of Environment*, 117, 469-474

DOI: 10.1016/j.rse.2011.10.019

*Author's contribution to research design (15%), data collection (30%), analysis (30%) and writing (10%)

Abstract

Mutual shading of needles in coniferous shoots and small-scale variations in needle area density both within and between shoots violate conventional assumptions used in the definition of the elementary volume in radiative transfer models. In this paper, we test the hypothesis if it is possible to scale needle spectral albedo up to shoot spectral albedo using only one structural parameter: the spherically averaged shoot silhouette to total area ratio (STAR). To test the hypothesis, we measured both structural and spectral properties of ten Scots pine (*Pinus sylvestris*) shoots and their needles. Our results indicate that it is possible to upscale from needle to shoot spectral albedo using STAR. The upscaling model performed best in the VIS and SWIR regions, and for shoots with high STAR values. As STAR is linearly related to photon recollision probability, it is also possible to apply the upscaling model as integral part of radiative transfer models.

Keywords

Photon recollision probability; spectral invariants; STAR; *Pinus sylvestris*

4.1 Introduction

In coniferous canopies, needles are densely packed in shoots with dimensions of typically only a few centimeters. Multiple scattering occurring within shoots is a long-known optical phenomenon (e.g. Norman & Jarvis (1975)). Mutual shading of needles in shoots and small scale variations in needle area density both within and between shoots also violate the traditional assumptions made in the definition of elementary volume in radiative transfer (RT) models. Thus, the use of a coniferous shoot (sometimes referred to as ‘shoot-like leaf’) as the basic scattering element or structural unit has been proposed to solve this problem (Nilson and Ross 1997). Forest reflectance simulations have also highlighted the importance of accounting for within-shoot scattering; within-shoot scattering may be the single most important structural effect causing the reflectance of coniferous forests to be lower than that of broadleaved forests (Rautiainen and Stenberg 2005).

The G-function, also called ‘mean projection of unit foliage area’ was originally defined for flat leaves (Nilson 1971). For coniferous shoots, it is conceptually analogous to the ratio of shoot silhouette area to total (or hemisurface, defined as half of the total) needle area. Overlapping of needles in the shoot causes the shoot's G-value (defined as the spherically averaged silhouette to total needle area ratio, abbreviated as STAR) to be smaller than that of a single needle (Stenberg 2006). The overlap can be quantified by a needle clumping index (Nilson 1999) or shoot shading factor (Stenberg et al. 1994). The STAR for a shoot with no-within shoot shading is 0.25 (Stenberg 1996b), because the spherically averaged projection area of a needle is precisely one fourth of its total surface area (Lang 1991). From extensive empirical measurements we know that, for example for Scots pine, the reduction in shoot silhouette area resulting from needles overlapping is typically over 40% (Oker-Blom and Smolander 1988). This results in considerable differences between the approaches needed for RT modeling in broadleaved and coniferous canopies. Consequently, a method that would unify the mathematical treatment of the basic elements in RT modeling in both broadleaved and coniferous species is needed.

An elegant theory connecting STAR to the scattering properties of a shoot or a canopy was put forward by Smolander and Stenberg (2003, 2005), and later applied to a forest reflectance model based on the photon

recollision probability theory by Rautiainen and Stenberg (2005). This theory states that the scattering of a vegetation unit (i.e. its spectral albedo) is approximated by the formula (Equation 4.1):

$$\omega_{unit}(\lambda) = \omega_{element}(\lambda) \left(\frac{1 - p}{1 - p\omega_{element}(\lambda)} \right) \quad (4.1),$$

where ω is the spectral albedo and p is the photon recollision probability between the ‘elements’ (scattering centers). The photon recollision probability p is defined as the probability that a photon scattered from a leaf surface will interact with the canopy again. (Note that the photon recollision probability p as shown in Equation 4.1 is conceptually similar to the canopy structural parameter defined by Knyazikhin et al. (1998) and the parameter that links canopy scattering at any two wavelengths (Panferov et al. 2001).

In the mathematical relationship shown above (Equation 4.1), the ‘unit’ corresponds to, for example, a coniferous shoot and the ‘element’ to a needle. Furthermore, Smolander and Stenberg (2003, 2005) suggested that p can be defined at different hierarchical levels, and theoretically, at shoot-level p is linearly related to a measurable characteristic: the STAR of the shoot. However, until now, the hypothesis as mathematically formulated in Equation 4.1 has not been tested empirically even though it is a fundamental underlying assumption of the photon recollision probability theory. If Equation 4.1 holds empirically, it would have many practical consequences. We could apply the relationship in RT models for coniferous forests, for example, to upscale from needle to shoot albedo or to estimate shoot albedo from shoot structure (quantified by STAR) for different tree species in a simple manner.

In this short communication paper, we test empirically the hypothesis (described mathematically by Equation 4.1) that it is possible to upscale needle albedo to shoot albedo (directional-spherical reflectance factor) using only one structural parameter: the spherically averaged shoot silhouette to total needle area ratio (STAR). To test the hypothesis, we measured both structural and spectral properties of Scots pine shoots and their needles in laboratory conditions.

4.2 Materials and methods

4.2.1 Sample shoots

Ten samples of coniferous shoots were collected from different mature Scots pine (*Pinus sylvestris* L.) trees growing in a temperate climate in Switzerland (N 47.39, E 8.54). The shoots were selected to represent a wide range of structures. The twig length of the shoots ranged from 6.1 to 16.8 cm, mean needle length from 4.7 to 6.8 cm, and number of needles in a shoot from 98 to 226 (Table 4.1).

Each sample consisted of two ‘sister-shoots’: same-year shoots growing next to each other. From the sister-shoots, one shoot was used for measuring shoot structural and spectral properties and the other shoot for measuring simultaneously needle optical properties. The reason for using sister-shoots is that the illumination source used emits heat and may cause the needles to dry up and change their optical properties. The sister-shoot samples were stored in zip-locked plastic bags with wet paper pulp in a cooling box (temperature approximately +8 °C) for a maximum of five hours before spectral and structural measurements.

4.2.2 Shoot structural properties

The silhouette area of each shoot was photographed in 24 different angles using a high resolution digital camera (NIKON D90) following the procedure described by Stenberg et al. (2001). A set of six measurements was made in which the angle of the shoot axis to the plane of projection was changed in steps of 30°. The procedure was repeated four times after rotating the shoot axis by 90° (since shoots were not symmetrical in respect to the shoot axis). Two measurement scales, a horizontal and a vertical one, were placed around the shoot and included in each image. After photographing the shoot silhouette area of the shoot, the dimensions of the shoot (twig length and diameter, number of needles, mean length of needles) were measured. Next, all needles were detached and photographed to obtain projected needle area. We assumed that the cross-sectional needle geometry of Scots pine needles is approximated by a half-cylinder (Niinemets et al. 2001; Tirén 1926) i.e. a constant factor of 2.57 was used to convert the projected needle area to an estimate of the total needle area. Finally, the ImageJ software (version 1.44) was used to calculate the silhouette areas for each shoot from the digital images. The final product, STAR, was computed for each shoot as a weighted average of the 24

silhouette areas divided by total needle area (Oker-Blom and Smolander 1988; Stenberg et al. 2001). The structural properties of the shoots are reported in Table 4.1

Table 4.1 Morphological properties of the sampled Scots pine shoots. (STAR = spherically averaged shoot silhouette to total needle area ratio; p=photon recollision probability, calculated from STAR).

Shoot number	Twig length (cm)	Twig diameter (mm)	Number of needles	Mean needle length (cm)	STAR	p
1	14.8	4	194	6.6	0.12	0.52
2	6.1	3	98	4.7	0.13	0.48
3	13.7	3	226	4.8	0.14	0.44
4	7.7	2	148	6.8	0.14	0.44
5	8.3	2	100	6.8	0.14	0.44
6	10.4	3	132	6.3	0.15	0.40
7	10.9	3	170	5.8	0.15	0.40
8	13.6	2	144	5.7	0.16	0.36
9	9.2	2	112	6.7	0.16	0.36
10	16.8	3	198	5.7	0.19	0.24

4.2.3 Shoot albedo measurements

The upper and lower hemispherical bidirectional reflectance distribution functions (BRDF) of each shoot were approximated by biconical measurements using the LAGOS goniometer (Dangel et al. 2005). The goniometer is built of black-coated aluminium and has a diameter of 4 meters (i.e. a zenith arc and an azimuth rail of 2 m radii). The azimuth rail can be rotated 360° and the spectroradiometer (attached to a motorized sled) can be operated from -74° to +74° along the zenith arc. To minimize effects of diffuse illumination, the walls of the laboratory are painted with a special low reflecting black color, and all other measurement equipment or reflecting surfaces within the lab were covered with optically black cloth.

The illumination source used for the spectrodirectional measurements was a 1000-W brightness-stabilized quartz tungsten halogen lamp (Oriel, type 6317). A dedicated lens system built as a Köhler illuminator using an spherical reflector and a condensor resulted in a beam diameter of approximately 4 cm at the front of the optical system. As the distance between the lamp and the sampled shoot was 80 cm, the beam divergence (i.e. half-

vertex angle) was about 12° resulting in the whole shoot (and nothing but the shoot) being illuminated. The spectroradiometer attached to the goniometer was an ASD FieldSpec 3 (Analytical Spectral Devices, Inc.) equipped with bare-fiber optics. Thus, the whole shoot was always completely within the field-of-view of the spectroradiometer. A schematic presentation of the measurement set-up is shown in Figure 4.1.

The measurement set-up for this study was as follows: the shoot was tightly secured with 0.2 mm black cotton thread in six directions in the middle of a circular steel frame (diameter 100 cm, i.e. larger than the illumination beam) that was clamped from below to a tripod so that the shoot was located 80 cm from the lens of the irradiance source. The direction of the axis of the shoot was in the plane of the shoot-holding frame, which was kept perpendicular to irradiation direction in the center of the goniometer. To obtain shoot spectral albedo, we needed to acquire two full hemispheres of spectral measurements. After completing a full upper hemisphere of measurements, the shoot-holding frame was rotated 180° in order to measure the lower hemisphere. After the rotation, the shoot together with the frame was re-centered in the goniometer, and the frame was oriented to be perpendicular to the direction of irradiation. The shoot was always irradiated from the same side. In other words, radiation interception was maximized by irradiating the shoot always from its longest side. To enable the calculation of shoot projection area in the direction of light rays, the shoot was photographed using a digital camera in the exact opposite direction from the lamp. The same camera and processing approach as in shoot structure measurements (Section 4.2.2) was used. The distance from the shoot to the camera was approximately 4 m.

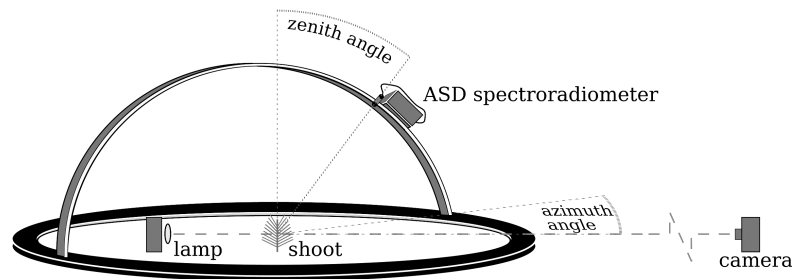


Figure 4.1 Measurement set-up using the goniometer in the laboratory.

As the aim of the measurements was to retrieve the spectral albedo of the shoot, we chose an angular sampling pattern based on Gauss–Legendre quadrature over the cosine of the polar angle and uniform sampling of the azimuth angle. However, to avoid having the shoot-holding frame within the field-of-view of the spectroradiometer at 90° , this specific azimuth angle was substituted by two azimuth angles, at 80° and 100° . Additionally, to continuously monitor the status of the shoot, an additional spectrum at 0° zenith was recorded in each azimuth angle. In other words, spectral measurements were carried out at 0° , 21.2° , 48.6° and 74° zenith angles, and $0/180^\circ$, $\pm 30^\circ$, $\pm 60^\circ$, $\pm 80^\circ$, $\pm 100^\circ$ and $\pm 150^\circ$ along the azimuth arc. Five spectra were recorded in each measurement angle using an integration time of 1.09 seconds. Before the shoot was placed in the center of the goniometer arc, we measured a reference signal using a 2” by 2” calibrated white Spectralon reference panel placed in the same location as the shoot. The reference panel was carefully adjusted to be orthogonal to the light beam.

The laboratory setup did not allow us to measure direction close to forward- and backward-scattering. Two directions could not be sampled out of the 36-direction quadrature in each hemisphere: zenith angle 74° , azimuth angles 0° and 180° . The backward-scattering direction was blocked by the lamp position itself whereas in the forward-scattering direction the spectroradiometer signal was saturated by the non-intercepted radiation beam. Therefore, we substituted the strongest signal recorded in a neighboring quadrature node for the direction closest to backscattering. For forward-scattering, we used the average signal measured at its four closest neighbor-nodes.

To obtain a spectral albedo (directional-spherical reflectance factor) for each shoot the measured signal was integrated over the full sphere using the Gauss-Legendre quadrature weights. The integrated reflectance signal was finally normalized to the signal produced by a non-absorbing object of the same projection area. The integrated signal of such a perfect scatterer was calculated using the shoot projection area and the signal produced by the reference panel. We call the quantity produced as an end-result of these calculations the spectral albedo of the shoot.

4.2.4 Needle albedo measurements

The spectral albedos for needles in each sister-shoot were measured concurrently in a calibration laboratory using a second ASD FieldSpec 3 spectroradiometer. The two ASD instruments used in this study were recently

intercalibrated (Suárez et al. 2011). The calibration results showed that relative differences in hemispherical- conical reflectance factors (HCRF, see Schaepman-Strub et al. (2006) for terminology conventions) were less than 5% in the spectral range from 450 to 2450 nm and 1–2.5% from 600 to 2300 nm. The ASD spectroradiometer was also coupled to an integrating sphere (ASD RTS- 3ZC). Imperfect sphere wall coating led to increased measurement noise above 1800 nm, and therefore, the range above this was removed prior to further analysis.

Three needle samples were prepared per sister-shoot. Each sample consisted of eight to ten randomly selected needles, which were placed parallel to each other at a distance of less than the width of a needle into a specifically designed needle sample carrier (Malenovský et al. 2006a). The hemispherically integrated spectral reflectance and transmittance of both abaxial and adaxial needle sides were measured using the coupled spectroradiometer and integrating sphere. Each measurement represented an average of 100 spectral scans. The directional-hemispherical reflectance (R) and transmittance (T) was calculated using adopted equations (Mesarch et al. 1999) as follows:

$$R = \frac{R_{TOTAL} - STR}{REF - STR} \cdot \frac{1}{1 - GF_R} \quad (4.2),$$

and

$$T = \frac{\left(\frac{T_{TOTAL}}{REF - STR} - R_w \cdot GF_T \right)}{1 - GF_T} \quad (4.3),$$

where R_{TOTAL} and T_{TOTAL} is s the reflected/transmitted radiation from the sample in the reflectance/transmittance mode, REF is the radiation reflected from the white reference standard in the reference mode, STR is the stray light radiation, R_w is the reflectance of the integrating sphere, and $GF_{R/T}$ is the gap fraction of the sample in reflectance/ transmittance mode. The gap fraction was obtained using a needle sample overlapped with a mask defining the exact illumination area of the sample during the reflectance and transmittance measurements. The samples were subsequently scanned with a double-lamp

desktop scanner at 800 dpi. $GF_{R/T}$ was retrieved from 8-bit gray-scale scanned images of the needle samples as the ratio of the total number of white pixels (air gaps) in the image to the number of white pixels of the empty mask area. ‘White pixels’ here refer to the pixels with digital numbers greater than or equal to the gray-scale threshold value of 224.

The R and T signatures were calculated using Equations 4.2 and 4.3 and smoothed using a Savitzky-Golay filter. The final needle spectral albedo per sample was the sum of the directional-hemispherical R and T, which were computed as an average of the abaxial and adaxial measurements of three needle samples.

4.2.5 Upscaling from needle to shoot spectra

We computed a predicted shoot spectral albedo (ω_{shpr}) as a function of wavelength (λ) from the measurements of needle spectral albedo (ω_L) and shoot STAR in the following way (*sensu* Smolander and Stenberg (2003)):

$$\omega_{shpr}(\lambda) = \omega_L(\lambda) \left(\frac{1-p}{1-p\omega_L(\lambda)} \right) \quad (4.4).$$

4STAR can be interpreted as the mean probability that a photon emitted from a random point on the needle surface of the shoot will not hit another needle of the shoot (Smolander and Stenberg 2003). Thus, subtracting 4STAR from 1 will give us the recollision probability p needed in the previous equation:

$$p = 1 - 4 \cdot STAR \quad (4.5).$$

Finally, the predicted shoot spectral albedo was compared to the measured shoot spectral albedo. The theoretical background of the upscaling model (cf. Equations 4.4 and 4.5) is discussed in detail in Smolander and Stenberg (2003).

4.3 Results and discussion

Needle spectral albedos were considerably higher than shoot spectral albedos throughout the studied wavelength range (400–1800 nm) (Figure 4.2). Generally, more variation was observed in the shoot spectra (coefficient of variation, CV 8-21%) than in the needle spectra (CV 2-13%) due to the

influence of shoot geometry. The largest variations both in needle (CV up to 13%) and shoot (CV up to 21%) spectral albedos were observed in the visible range (VIS, 400-700 nm) range, and the smallest variations in the near infrared (NIR, 700-1400 nm) range (i.e. CV was as low as 2% for needles and 8% for shoots). The shoots with the highest STAR values (i.e. STAR > 0.15) tended to have also the highest shoot spectral albedos (especially in the near infrared range), and vice-versa.

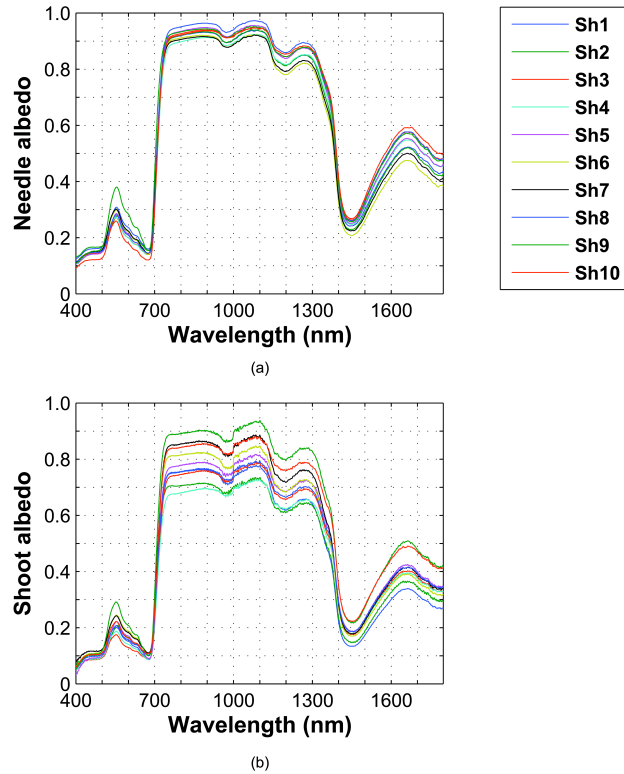


Figure 4.2 Measured spectra. (a) Needle spectral albedos for the ten study shoots. (b) Shoot spectral albedos for the ten study shoots.

Upscaling from needle to shoot spectral albedo using STAR (Equation 4.4) performed well in the visible (VIS) and SWIR regions i.e. for shoot albedo values smaller than 0.5 (Figure 4.3). In the NIR range ($\omega_{\text{shpr}} > 0.5$), on the

other hand, the upscaling model produced slight overestimates of shoot spectral albedo when compared to the measurement data. The shoots with large STAR values showed a better fit between measured and predicted shoot spectral albedos as compared to shoots with smaller STAR values, which tended to have a larger difference between the measured and predicted spectral albedos in the NIR region.

Shoot8 stands out as an exception in our results: it had one of the largest STAR values, yet it had relatively low shoot spectral albedos (Figure 4.2b) and a poorer fit between measured and predicted values (Figure 4.3) than other shoots with a similar STAR. This is probably due to the exceptionally sparse structure of the shoot: it had the smallest number of needles per twig length when compared to all other study shoots (Table 4.1). Thus, we can expect the contribution of the twig to the spectrum of the shoot to be larger than in other shoots.

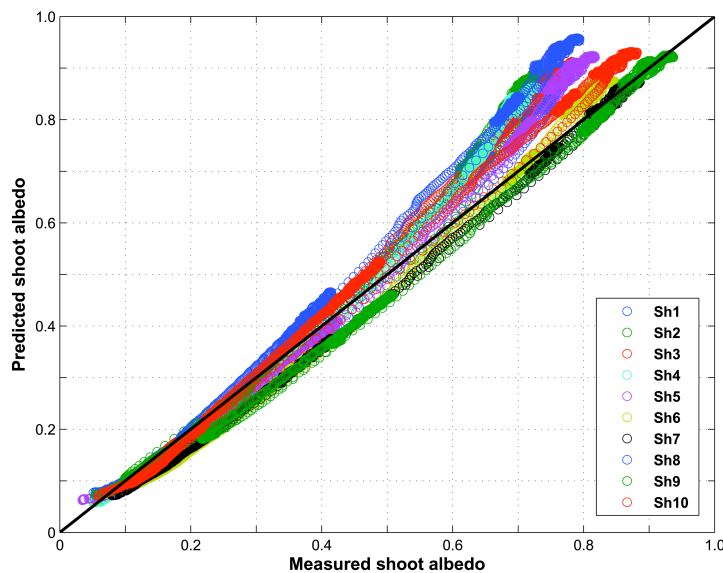


Figure 4.3 A comparison of measured and predicted shoot spectral albedos for 400-1800 nm.

Finally, we examined the overall performance of the upscaling model through relative root mean square errors (RMSE) averaged for all study shoots (Figure 4.4). The relative RMSE's in most of the VIS and SWIR regions were

often lower than in the NIR region. Firstly, the better performance of the model could be attributed to better quality spectral data in the VIS and shortwave infrared (SWIR, 1400-1800 nm) regions: the spectrometer has better radiometric performance in these regions. A second explanation is simply the shape of the functional dependence between needle and shoot spectral albedos: there is an enhanced sensitivity to model parameter errors in NIR (c.f., Equation 4.4). A third possible explanation could be that there is, in theory, less specular reflectance in SWIR, though little empirical data is available support this statement. The level of specular reflectance depends on the refractive index of the needle's wax layer. The slow decrease in wax refractive index is hardly detectable when comparing scattering in VIS and NIR leading to an approximately constant contribution of specular reflectance with values close to 0.04 (in absolute reflectance units). Theoretically, using wax refractive index data from the PROSPECT leaf reflectance model (Jacquemoud and Baret 1990), specular reflectance decreases by 25% to a value of 0.03 at 2000 nm. In other words, if more scattering took place inside the needle compared with the VIS and NIR regions, then the photon recollision probability theory (which describes diffuse scattering) would work better in SWIR. However, to assess whether this explanation is plausible we would need to measure the specular and diffuse components for a whole spectral region of interest (400-1800 nm) separately, following for instance the approach of Bousquet et al. (2005).

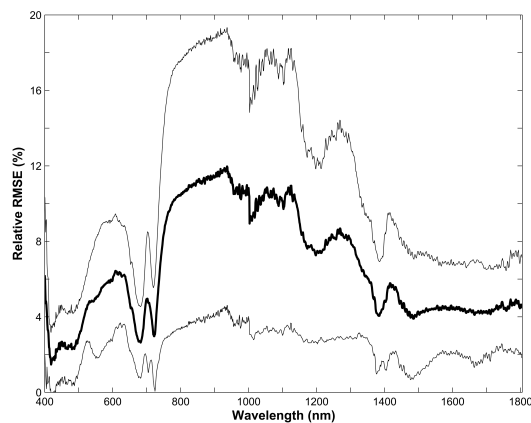


Figure 4.4 Average relative root mean square error (RMSE, in percent) of measured and predicted shoot spectral albedos as a function of wavelength. The grey lines show standard deviation of RMSE values.

Generally speaking, the most likely reasons for a non-perfect agreement between the upscaling model and our measured data has its foundations both in the definition of photon recollision probability and in measurement uncertainties. Equation 4.5 is formulated for photon recollision probability under absolutely diffuse illumination (i.e. all needle surfaces are uniformly irradiated) and diffuse (Lambertian) scattering. Neither condition is perfectly fulfilled in our experiment. Thus, the actual probability that a photon will interact within the shoot again cannot be exactly related to STAR via Equation 4.5.

The shoot scattering measurements were performed at the sensitivity limit of the spectroradiometer. Thus, large levels of noise are expected in the directional shoot scattering measurements as the number of spectra averaged was five, considerably less than what is suggested by instrument manufacturer (30). However, a total of 80 measurements, thus 400 spectra, were used in calculating the albedo of each shoot. This reduced efficiently random noise. Further errors were probably introduced from stray light scattered by the equipment, and from the inaccuracy of the Spectralon measurements used to normalize the scattering measurements. Stray light was measured for all quadrature angles. In the VIS region, the level of stray light was low (less than 1% of the signal using a Spectralon measurement). Stray light increased abruptly at 700 nm to a level of 1.5% relative to Spectralon measurements and remained constant in NIR and SWIR. When compared to the spectral scattering properties of an average shoot, stray light contributed about 1% in the visible range and increased to 2% at 1850 nm. The relative stray light spectrum had a narrow local peak of 4% close to 700 nm and a wider peak at 1450 nm (about 8%). Although stray light was removed from the spectra, we still estimate that total noise-related measurement certainties are on average 2% and increase with wavelength.

The errors related to normalization of shoot reflectance using the Spectralon are more difficult to quantify. At least six Spectralon measurements (a total of 30 spectra) were averaged for each shoot. Orientation of the Spectralon panel caused additional measurement uncertainty. However, we were able to compare average Spectralon measurements made before and after measuring different shoots and estimate the relative error in measured shoot albedo arising from Spectralon signal to be about 4%. Therefore, we estimate the total uncertainty (at 2*standard deviation level) in our shoot albedo estimates to be at least 5%.

Shoot and needle geometry vary considerably in response to the light conditions under which they grow. From STAR measurements conducted for different coniferous species (e.g. Sprugel et al. (1996), Stenberg et al. (1995)) we know that shoot STAR increases when shading increases. In other words, shaded shoots exhibit the highest STAR values, and thus, also the least mutual shadowing of needles in a shoot (Stenberg 1996b). A shoot with a high STAR value can be either flat ('leaf-like') or cylindrical ('brush-like'). A shoot with a high STAR value not only has a lower photon recollision probability (Equation 4.3, Table 4.1) and a higher spectral albedo, but also a more even spatial distribution of photon-needle interactions than a shoot with a lower STAR value. The discrepancy between measured and predicted spectral albedos for sparser shoots ($STAR < 0.15$) could possibly result from the poor performance of the photon recollision probability theory (due to the uneven distribution of photon-needle interactions) or a larger influence of the twig (bark). This result implies that the upscaling model tested in this paper performs the best in canopies with an even distribution of radiation.

Our study showed that it is possible to scale from needle up to shoot spectral albedo using only one structural characteristic of the shoot, STAR. The upscaling model performed best in the VIS and SWIR regions. As STAR is linearly related to photon recollision probability p , it is possible to apply the upscaling model as part of RT models. From the perspective of further applications, it would be interesting to investigate simple parameterizations of shoot scattering phase functions (Möttus et al. 2012) and, for example, whether the spectral albedo of a whole tree crown (and furthermore, a forest stand) can be linked to the crown spherically averaged silhouette area through a simple relationship. In other words, can we upscale crown spectral albedo from shoot spectral albedo similarly?

Acknowledgements

We wish to thank D. Markulin for assisting in the set-up of the experiment and Pauline Stenberg for fruitful scientific discussions. Our study was funded by the Academy of Finland, University of Helsinki Postdoctoral Funds, and the EC (ECOCHANGE, GOCE-036866).

Chapter 5

Estimation of spruce needle-leaf chlorophyll content based on DART and PARAS canopy reflectance models

This chapter is based on:

Yáñez-Rausell, L., Malenovský, Z., Rautiainen, M., Clevers, J., Lukeš, P., Hanuš, J., & Schaepman, M.E., (In review). Estimation of spruce needle-leaf chlorophyll content based on DART and PARAS canopy reflectance models. *IEEE Journal of Selected Topics in Applied Earth Observations and Remote Sensing*

Abstract

Needle-leaf chlorophyll content (Cab) of a Norway spruce stand (*Picea abies* /L./ Karst.) was estimated from CHRIS-PROBA data using top-of-canopy bidirectional reflectance factor (BRF) simulated by a leaf radiative transfer (RT) model (PROSPECT) coupled with two different canopy reflectance models (DART and PARAS). The DART BRF simulations are based on a detailed description of the 3D forest scene, whereas the forest structural description in PARAS is simplified using photon recollision probability theory (p). The Cab sensitive continuum-removal based optical indices ANCB₆₇₀₋₇₂₀ and ANMB₆₇₀₋₇₂₀ were calculated from the canopy BRFs simulated with both canopy models. Empirical relationships established between the optical indices and the needle-leaf Cab content were applied to the CHRIS-PROBA data to retrieve spatially distributed Cab estimates. We used empirical relationships fitted to two retrieval methods, namely ANMB₆₇₀₋₇₂₀ and ANCB₆₇₀₋₇₂₀. The regressions for ANMB₆₇₀₋₇₂₀ were robust, especially when using the DART model. The ANCB₆₇₀₋₇₂₀ presented a worse performance, especially for PARAS, due to the sensitivity of the index to LAI variation. An inter-comparison between Cab estimates obtained with both optical indices simulated with both canopy RT models showed strong linear correlations, with a nearly perfect linear fit between the PARAS and DART retrievals using the ANMB₆₇₀₋₇₂₀ index (slope = 1.1, offset = 11 $\mu\text{g cm}^{-2}$). The relationship between Cab estimates based on the ANCB₆₇₀₋₇₂₀ index was also linear, although the deviation was increasing with increasing Cab values resulting in a steeper slope of the function. Comparison against the Cab map produced by an artificial neural network applied to an airborne image of the studied forest stand acquired with an AISA Eagle sensor showed a better performance of PARAS retrievals with an RMSE = 2.7 $\mu\text{g cm}^{-2}$ for the ANCB₆₇₀₋₇₂₀ approach and an RMSE = 9.5 $\mu\text{g cm}^{-2}$ for the ANMB₆₇₀₋₇₂₀ approach. DART retrievals encountered larger differences with an RMSE = 7.5 $\mu\text{g cm}^{-2}$ for the ANCB₆₇₀₋₇₂₀ approach and an RMSE = 23 $\mu\text{g cm}^{-2}$ for the ANMB₆₇₀₋₇₂₀ approach. Although better validation results were obtained for PARAS, DART empirical relationships were more robust. For most estimates systematic errors were dominating over random errors, indicating that retrieval algorithms can be potentially further improved. We recommend further analysis elaborating on the impact of parameterization differences for each model. The results indicate

that for the spatial resolution used, simpler RT models such as PARAS can be applied to retrieve plausible needle-leaf Cab estimates from satellite imaging spectrometer data.

Keywords

Chlorophyll estimation; continuum removal; radiative transfer; PROSPECT; DART; recollision probability; PARAS; optical indices; Norway spruce; CHRIS-PROBA; needle-leaf; coniferous forest

5.1 Introduction

The content of green photosynthetically active foliar pigments, mainly chlorophylls, is a key parameter for understanding the physiological functioning of coniferous forests within the global carbon cycle under dynamic climate changes (IPCC 2007). Chlorophyll molecules strongly absorb solar irradiation in blue and red parts of the electromagnetic spectrum (Chen et al. 2010). This phenomenon results in spectral absorption features that can be exploited by optical remote sensing (RS) methods to detect and quantify the leaf chlorophyll *a* and *b* content (*C_{ab}*). Established RS methods for estimating *C_{ab}* range from spectral indices (red/near-infrared band ratios, green and red-edge indices, and derivative indices) to more complex radiative transfer (RT) based methods (see reviews from Blackburn (2007), Le Maire et al. (2004) and Ustin et al. (2009)). The first, empirically based indices, are designed to suppress factors contributing to the remotely-sensed canopy reflectance besides the leaf pigments, i.e. the canopy structure, background reflectance, illumination and viewing geometry (Myneni et al. 1995). Conversely, the RT methods that are built on the physical laws governing photon-canopy absorption and scattering processes can explain the contribution of the different factors involved in forming the RS signal (Schaepman et al. 2009), thus providing a consistent link between leaf pigments and canopy reflectance (Knyazikhin et al. 2013). This is especially important when applied to heterogeneous forest environments, where canopy structure plays a major role in the canopy scattering processes (Verrelst et al. 2008; Widlowski et al. 2007).

Coniferous forest stands represent a structurally heterogeneous environment, especially due to the complex foliage clumping, i.e. non-random distribution of foliage, appearing at different hierarchical levels of the canopy (Chen 1996; Stenberg 1996a, 2006). The clumping of small needle-leaves is claimed to be the main reason for a lower reflectance in the near-infrared (NIR) region, as compared to broadleaf forests (Nilson 1999; Rautiainen and Stenberg 2005). Despite its importance, many RT models have not fully implemented the foliage clumping effect. For example, photon scattering properties of the shoots are often not considered (see review from Stenberg et al. (2008)), although it is known that the within-shoot multiple scattering considerably affects the canopy radiation regime (Norman and Jarvis 1975).

One RT model used for Cab estimation in coniferous forests as demonstrated by Malenovský et al. (2013), is the Discrete Anisotropic Radiative Transfer (DART) model (Gastellu-Etchegorry et al. 2004). Although scattering at shoot level is not accounted for in DART either, the characterization of the structural complexity of the coniferous forest in terms of branch foliage clumping and inclusion of various woody elements is possible. In Malenovský's study, a more detailed definition of tree crown structures allowed DART to simulate the canopy bidirectional reflectance factor (BRF, for terminology see (Schaepman-Strub et al. 2006)) corresponding to Airborne Imaging Spectroradiometer for Applications (AISA) Eagle (Spectral Imaging, Specim Ltd., Finland) image data, acquired at a spatial resolution of 0.4 m. An artificial neural network and a new optical index built upon the relationship between the DART simulated BRF and the Cab content was applied to estimate Cab from the AISA data. The results showed that a 3D RT model like DART can be employed to estimate Cab of complex coniferous forest canopies. However, the approach requires many input parameters and it is computationally highly demanding.

An alternative with a simpler parameterization of coniferous canopy structure, but taking into account the shoot-level scattering processes, is a physically based forest reflectance model named PARAS (Rautiainen and Stenberg 2005). PARAS simulates canopy BRF by upscaling the leaf scattering albedo (i.e., sum of leaf reflectance and transmittance) through a spectrally invariant parameter called the photon recollision probability (p). This approach is based on the spectral invariants theory introduced by Panferov et al. (2001). The p is defined as the probability that a photon which has been scattered by the canopy will interact with a canopy phytoelement again (Smolander and Stenberg 2003). The PARAS model was used to examine the effect of understory vegetation on forest reflectance in the boreal ecosystems (Rautiainen et al. 2007) and also for estimation of forest structural characteristics, for example leaf area index, from satellite RS data (Heiskanen et al. 2011). Yet, to our best knowledge, it has not been tested for estimation of forest Cab.

The objective of this paper is to compare the performance of the two described canopy RT models, i.e. DART and PARAS, when being employed in the estimation of coniferous needle-leaf Cab from satellite imaging spectroscopy data at a spatial resolution of about 20 m. We will evaluate how much the leaf Cab estimates based on a detailed 3D structural forest description in DART differs from the Cab estimates produced by PARAS with

a simpler structural parameterization based on the photon-recollision probability using an established chlorophyll sensitive optical index. Comparable performance of both models would imply that the same level of Cab retrieval accuracy could be achieved with less intensive RT model parameterization and reduced computational power using PARAS.

5.2 Materials and methods

5.2.1 Study area and CHRIS-PROBA satellite image data

The study area is a regularly planted Norway spruce (*Picea abies* /L./ Karst.) stand (an area of 11,560 m²) at the permanent eco-physiological research site “Bílý Kříž” located in the Moravian-Silesian Beskydy Mountains (18.54° E, 49.50° N, mean elevation of 894 m a.s.l.) in the Czech Republic. The forest grows on a moderate slope of 13.42° with a southern aspect. CHRIS-PROBA (Compact High Resolution Imaging Spectrometer) satellite images (Cutter et al. 2000) of the study area were acquired on 12th September 2006. The acquisition was carried out in sensor mode 4, designed specifically for remote sensing of chlorophyll content (Cab), collecting images of 18 channels located in the spectral region of 485 – 800 nm, with a bandwidth ranging from 5.8 to 14.9 nm, and with a nadir spatial resolution of 17 m. At the time of the CHRIS-PROBA acquisition, the stand was about 29-years old, the stand density was 1430 stems.ha⁻¹, the average tree height was around 11.6 m and the average diameter at breast height (DBH) was equal to 14.3 cm. The canopy cover (CC) of about 80-90% strongly limited the influence of the forest background on the satellite data. The acquired CHRIS-PROBA multi-angular images were all radiometrically and atmospherically corrected as described in Lukeš et al. (2011), but only the nadir reflectance image was used in this study for the needle-leaf Cab estimation.

5.2.2 Field measurements

The study area was subjected to an intensive field investigation characterizing the overall canopy structure, foliar biochemistry, and optical properties of needles and other canopy elements including forest background. A set of 120 needle-leaf samples of the last three age-classes (C ~ current year, C+ ~ 1 year old, and C++ ~ 2 years old) were collected from three levels of the vertical crown profile (upper-part ~ sun exposed (E), middle-part ~ transitional (T), and lower-part ~ shaded (S) needles) around

the CHRIS-PROBA acquisition time. Needle-leaf directional-hemispherical reflectance and transmittance factors (DHRF and DHTF, respectively, further referred to as reflectance and transmittance) were measured as described in Lukeš et al. (2011). Simultaneously, a complementary set of needle samples, analyzed later for foliar pigments and biophysical characteristics were acquired and processed as described in Malenovský et al. (2013) using the method of (Yáñez-Rausell et al. 2014a; Yáñez-Rausell et al. 2014b). The DHRF of bark samples, peeled from four randomly selected branches and one tree stem, were also measured. Finally, the reflectance of the forest floor at the study site, mostly composed of litter (senescent needle-leaves) with occasional spots of bare soil, was derived as follows: the DHRF of both soil and senescent needles were measured separately (Malenovský et al. 2008) and the weighted average spectrum of the stand floor was then mixed using the surface's abundance ratio of 1/3 of bare soil vs. 2/3 of senescent needle-leaves as weights.

Besides the spectral optical properties, above and below-canopy readings were collected with the LAI-2000 Plant Canopy Analyzer (Li-Cor, Inc., USA). These measurements were part of an extensive and continuous LAI monitoring activity carried out between 2005-2007 in the studied Norway spruce forest along two subplots with different stand densities following the sampling scheme described in Pokorný et al. (2008). The readings were used to compute the effective leaf area index (LAI_{eff}), the canopy gap fraction (*cgf*) and the so-called “diffuse non-interceptance” (DIFN). The additional canopy structural parameters like the stand branch area index (BAI) and the vertical and horizontal foliage distributions within a crown, the geometry of first order branches, and the distribution of fine woody twigs, needed to create the 3D forest scene for DART model (Malenovský et al. 2008), were obtained from destructive measurements (Lukeš et al. 2011; Pokorný and Marek 2000).

All the field measurements provided representative values used to parameterize the coupled leaf-canopy RT models employed in this study to simulate the Norway spruce forest BRDF.

5.2.3 Simulation of top-of-canopy bidirectional reflectance factor

5.2.3.1 PROSPECT model

Needle-leaf reflectance and transmittance were simulated with the PROSPECT leaf RT model (version 3) (Jacquemoud and Baret 1990), adjusted for Norway spruce needles by Malenovský et al. (2006a). Measured

needle reflectance and transmittance spectra were used to adjust the PROSPECT parameters for the three age-classes of exposed, transitional and shaded spruce needles (Malenovský et al. 2006a). PROSPECT input values are summarized in Table 5.1 (for details about the PROSPECT parameterization see Malenovský et al. (2013)).

The nine PROSPECT simulated needle reflectance and transmittance spectra, i.e. three age-classes of exposed, transitional and shaded spruce needles, were upscaled to the level of forest canopy with (i) the DART (Gastellu-Etchegorry et al. 2004), and (ii) the PARAS model (Rautiainen and Stenberg 2005). For the latter case, a needle-leaf albedo (ω_L) was used instead of the reflectance and transmittance spectra. The representative mean reflectance and transmittance were computed as weighted averages of the nine corresponding PROSPECT simulated spectra, using the weights established in Table I of Lukeš et al. (2011). Finally, ω_L was calculated as the sum of these weighted averages.

5.2.3.2 DART simulations

Canopy BRF was simulated with DART according to the approach described in Malenovský et al. (2013), with minor modifications of the input parameters related to the specific image acquisition and sensor, i.e. CHRIS-PROBA instead of AISA (Table 5.2). In total eight spectral bands corresponding to the red and red-edge bands of the CHRIS-PROBA image (with central wavelengths at 670, 681, 689, 695, 701, 707, 714 and 720 nm) were simulated. All combinations of five LAIs and ten Cab values in the PROSPECT-DART model combination resulted in 50 BRF simulations per single spectral band. The other parameters were kept fixed (Malenovský et al. 2013; Malenovský et al. 2008). To account for the canopy structural heterogeneity, the forest geometrical description included different structural and optical characteristics for several horizontal and vertical positions within individual tree crowns (Malenovsky et al. 2013). For comparison purposes with PARAS simulations the canopy-cover (CC) of DART forest scenes was fixed at 90%, as measured on average ($\pm 5\%$) at the study site. This parameter was approximated as $1 - \text{cgf}(\theta_i)$ (Rautiainen et al. 2005) where $\text{cgf}(\theta_i)$ is the canopy gap fraction (cgf) in the direction of the viewing zenith angle (θ_i), and it was obtained from the LAI-2000 Plant Canopy Analyzer measurements. The output dataset from DART will be referred to as the DART Look-Up-Table.

Table 5.1 Fixed input parameters for the PROSPECT model simulations of Norway spruce needle optical properties (Cw = needle-leaf water column, Cm = needle-leaf mass per area, N = needle-leaf mesophyll structural parameter, C = needles of the current growing season, C+ = needles of the previous growing season, and C++ = needles older than the previous growing season).

Needle type	Cw [cm]	Cm [g cm ⁻²]	N
Exposed C	0.0221	0.0177	2.13
Exposed C+	0.0250	0.0197	2.13
Exposed C++	0.0246	0.0202	2.13
Transitional C	0.0213	0.0128	2.13
Transitional C+	0.0230	0.0157	2.13
Transitional C++	0.0229	0.0166	2.13
Shaded C	0.0169	0.0102	2.13
Shaded C+	0.0199	0.0119	2.13
Shaded C++	0.0234	0.0149	2.13

5.2.3.3 PARAS simulations

For comparison purposes, the 3D forest description and the sensor and solar angular specifications used to generate the DART Look-Up-Table were used to simulate the PARAS Look-Up-Table of BRF values (Table 5.2). In PARAS, the forest BRF is calculated as a sum of the understory and canopy components through the equation:

$$BRF = cgf(\theta_1)cgf(\theta_2)\rho_{ground} + f(\theta_1, \theta_2)i_0(\theta_2)\frac{\omega_L - p\omega_L}{1 - p\omega_L} \quad (5.1),$$

where θ_1 and θ_2 denote the view (sensor) and Sun zenith directions, cgf denotes the canopy gap fraction, ρ_{ground} is the BRF of the forest understory, f describes the directional distribution of the reflected radiation, i_0 is the canopy interception (i.e. fraction of the incoming radiation hitting canopy elements), p is the photon recollision probability, and ω_L is the single scattering leaf (needle) albedo.

The cgf s, which are extracted from the LAI-2000 Plant Canopy Analyzer measurements, are the device readings corresponding to the concentric rings whose angles are closest to θ_1 and θ_2 , respectively. The ρ_{ground} was expressed as the weighted average from bare soil and senescent needle leaves spectra (Section 5.2.2).

Table 5.2 Fixed and varying key input parameters for DART and PARAS BRF simulations of a Norway spruce scene.^(a) In the PARAS model, field-based LAI values were averaged to match DART simulated LAI ranges.^(b) PARAS BRF simulated between 450 and 1000 nm was resampled from 5 to 1 nm spectral resolution and then integrated into the eight CHRIS-PROBA bands.

Parameters common to DART and PARAS models			
Sun position (fixed)	/Real solar noon/		
Zenith angle	θ_s	[°]	46.6
Azimuth angle (from North angle clockwise)	ϕ_s	[°]	180
Needle-leaf area Index	LAI	[m ² m ⁻²]	3-11 in steps of 2 ^(a)
Simulated CHRIS- PROBA bands (central wavelengths)	λ	[nm]	670, 681, 689, 695, 701, 707, 714 and 720 ^(b)
Parameters that are specific for DART model			
Slope (fixed)		[°]	13.5
Canopy closure (fixed)	CC	[%]	90

The f function was calculated according to Möttus and Stenberg (2008). The i_0 was computed from the cgf as $(1 - cgf(\theta_2))$. The average photon recollision probability of the stand (p) was estimated using the method proposed by Stenberg et al. (2013):

$$p = 1 - \frac{i_D}{LAI + BAI} \quad (5.2),$$

where i_D is the canopy diffuse interceptance approximated as (1-DIFN), i.e. one minus the “diffuse non-interceptance”. Canopy LAI was estimated from the effective LAI (LAI_{eff}) measured by the LAI-2000 Plant Canopy Analyzer as $LAI = 1.6 * LAI_{eff}$. The coefficient 1.6 is a site-specific coefficient derived from the field destructive measurements that corrects for both the shoot-clumping and the presence of woody biomass (Pokorný and Marek 2000). In order to incorporate the annual variability of LAI into the PARAS Look-Up-Table simulations, we used a normally distributed LAI dataset collected between 2005 and 2007 over several areas of different stand densities within the Norway spruce forest where our study area is located. For comparison purposes, among all values in the dataset only LAI values matching the values used in the DART simulations (i.e. LAI=3-11 in steps of 2, Table 5.2) were used to build the PARAS Look-Up-Table. For each selected LAI the corresponding cgf and DIFN recorded by the LAI-2000 Plant Canopy Analyzer were extracted and used in the corresponding

equations. The branch area index (BAI) was computed based on the relationship $BAI=0.3*LAI$, where 0.3 is a site-specific coefficient derived destructively from the selected trees removed from the stand (Pokorný and Tomášková 2007). Since the proportion of woody elements is considered in the calculation of the probability p (Equation 5.2), the needle-leaf albedo (ω_L) was computed as a weighted average of the albedo from the needle and canopy woody elements (Stenberg et al. 2013). Weights were based on the LAI and the BAI, respectively. Finally, PARAS BRFS simulated between 450 and 1000 nm was resampled from 5 to 1 nm spectral resolution and then integrated into the eight CHRIS-PROBA bands according to their spectral specifications.

5.2.4 Cab estimation for CHRIS-PROBA data using optical indices

We implemented and cross-compared the retrieval approaches in estimating forest canopy Cab from the space-borne spectral CHRIS-PROBA image using the DART and the PARAS simulated Look-Up-Tables. The first approach employed the optical index presented by Malenovský et al. (2013) named $ANCB_{650-720}$ that is defined as the Area Under Curve of the continuum-removed (CR) reflectance between 650 and 720 nm ($AUC_{650-720}$), normalized by the CR Band Depth at 670 nm (CBD_{670}). The spectral region between 650 and 720 nm, where wavelength 650 nm represented the middle of the red chlorophyll absorption feature (550–750 nm) and wavelength 720 nm the middle of the red-edge region (680–760 nm) was chosen to include the most sensitive Cab absorption wavelengths and to avoid the negative interferences of canopy structure at the longer wavelengths of the red-edge region. The CBD_{670} to which the $AUC_{650-720}$ was normalized represented the least varying continuum-removed band depth within the chlorophyll absorption spectral range of 660–695 nm (Malenovský et al. 2013). The position of the particular band with the maximum chlorophyll absorption varies; however, the CBD at 670 nm was found to be the least sensitive to Cab changes, which provides a stable quantity for the normalization and expectedly a more robust performance of the $ANCB_{650-720}$ index.

In our study, the wavelength range corresponded to the 4th and 11th CHRIS-PROBA bands, i.e. 670 and 720 nm, defining the index as:

$$ANCB_{670-720} = \frac{AUC_{670-720}}{CBD_{681}} \quad (5.3).$$

The $AUC_{670-720}$ is computed as:

$$AUC_{670-720} = \frac{1}{2} \sum_{j=1}^{n-1} (\lambda_{j+1} - \lambda_j) (\rho_{j+1} + \rho_j) \quad (5.4),$$

where ρ_j and ρ_{j+1} are the values of the continuum-removed reflectance at the bands j and $j+1$, λ_j and λ_{j+1} are the wavelengths of the bands j and $j+1$, and n is the number of used spectral bands. For the given wavelength range, the continuum-removed band depth at 670 nm is equal to zero (first band of the continuum-removed interval), and therefore the next band at 681 nm was selected for the normalization (CBD_{681}). A subsequent sensitivity analysis with the simulated continuum-removed BRF confirmed that this band provided the most stable CBD among the available wavelengths with respect to the systematic Cab variations (Figure 5.3).

The $ANCB_{650-720}$ defined by Malenovský et al. (2013) is a variant of the optical index $ANMB_{650-725}$, defined originally in Malenovský et al. (2006b). The differences between these two are the wavelength range (650-725 nm for the $ANMB_{650-725}$) and the normalization of the continuum-removed area that is done by the maximum continuum-removed band depth of this spectral region. In our study, we had to adapt the $ANMB_{650-725}$ index to the available CHRIS-PROBA bands, resulting into the following index definition:

$$ANMB_{670-720} = \frac{AUC_{670-720}}{MBD_{670-720}} \quad (5.5).$$

where $MBD_{670-720}$ refers to the maximal band depth of the continuum-removed reflectance between 670 and 720 nm, i.e. one of the spectrally stable and the strongest chlorophyll absorption wavelengths between 681 and 695 nm.

The empirical functions describing the fit between the indices and the predefined Cab values were established using the TableCurve 2D software package (Systat Software, Inc., USA). The most appropriate functions describing the behaviour of optical indices in relation to changing Cab were expected to be of the same nature as published in Malenovsky et al. (2013), i.e. exponential. The best fitting exponential equations were selected based on the best combination with the highest coefficient of determination R^2 , the highest degree-of-freedom adjusted R^2 , the lowest fit standard error, and the

largest F-test ratio (tested at the probability level $p \leq 0.05$). They were then applied per-pixel to the CHRIS-PROBA image to estimate Cab.

The Cab estimates obtained per index and per RT model were cross-compared by computing the root mean square error (RMSE, Equation 5.6), the corresponding systematic (RMSEs, Equation 5.7) and unsystematic RMSE (RMSEu, Equation 5.8) (Willmott 1981):

$$RMSE = \sqrt{\sum_{i=1}^N (P_i - O_i)^2 / N} \quad (5.6),$$

$$RMSEs = \sqrt{\sum_{i=1}^N (\hat{P}_i - O_i)^2 / N} \quad (5.7),$$

and

$$RMSEu = \sqrt{\sum_{i=1}^N (P_i - \hat{P}_i)^2 / N} \quad (5.8),$$

where O corresponded to Cab estimated per index based on PARAS model, P to Cab estimated per index based on DART model, and

$$\hat{P}_i = a + bO_i \quad (5.9),$$

where a and b are the coefficients of an ordinary least squares regression between O and P . RMSEs and RMSEu are related through $RMSE^2 = RMSE_s^2 + RMSE_u^2$. Based on this relationship, if RMSEs dominates over RMSEu, the estimation algorithm is expected to produce biased Cab estimations due to the prevailing model systematic errors. On the contrary, if the RMSEu is the largest component of RMSE, then the algorithm is as good as it can be.

Finally, Cab CHRIS-PROBA estimates were compared against a Cab map created from an AISA Eagle image of the study area acquired at 0.4 m spatial resolution on September 14th, 2006. Cab was estimated for the AISA image by a conventional artificial neural network (ANN) trained with continuum removed PROSPECT-DART simulated BRF, following the approach

published by Malenovský et al. (2013). We selected a set of 56 validation polygons located in both the CHRIS and the AISA image, where each polygon is the size of the CHRIS-PROBA image pixel (i.e. 17 m x 17 m). Figure 5.1 illustrates a typical spectral signature as obtained with CHRIS-PROBA for the Norway spruce stand in the Bílý Kříž study area. It shows the average reflectance and the one standard deviation interval of the 56 pixels used for the validation of the Cab estimates derived from the CHRIS-PROBA image. Average Cab computed per polygon of the AISA-ANN image (average of approximately 1000 AISA sunlit pixels in a polygon) was compared to the Cab of the corresponding CHRIS-PROBA pixel. The Cab estimation performance of each optical index per model was assessed via RMSE, RMSEs and RMSEu as described above, where P corresponded to Cab estimated per optical index and per canopy model and O corresponded to the Cab estimated for the AISA-ANN image.

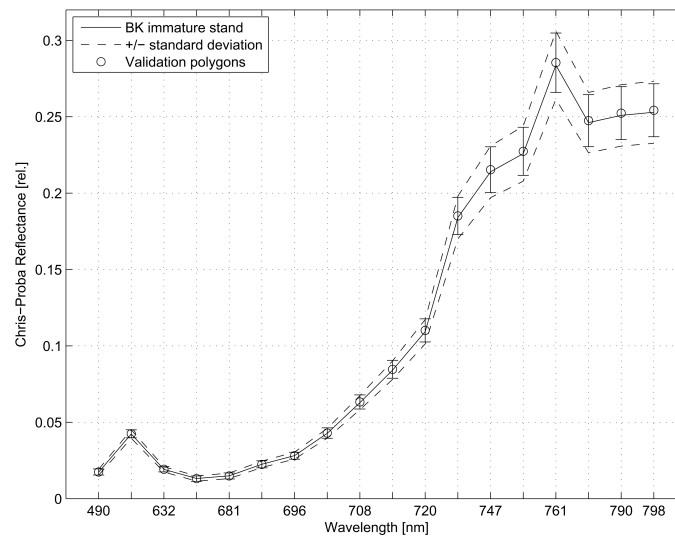


Figure 5.1 Mean top-of-canopy reflectance factors for 18 CHRIS spectral bands for all pixels corresponding to the Bílý Kříž Norway spruce stand (number of pixels=167). The solid line with open circular symbols represents the mean CHRIS-PROBA reflectance of 56 pixels used for the validation of the CHRIS-PROBA Cab estimates. Dashed lines represent the reflectance \pm standard deviation. Observed reflectance peak at band 15 (761 nm) is due to overcorrection of the atmospheric absorption feature.

5.3 Results and discussion

5.3.1 DART versus PARAS simulated BRF

First we compared the BRF of the investigated forest stand simulated with PARAS and DART. Figure 5.2a presents PARAS and DART simulated BRF of each spectral band averaged over all LAI and Cab input values. On average, the PARAS BRF is systematically higher than the DART BRF, with a mean offset of 0.02 for most of the wavelengths except for the three longest wavelengths (701-720 nm) where the difference increased to 0.03. Although, the average difference of 0.02 can be considered as relatively small, the standard deviation (STD) of the PARAS simulated BRF of about 0.05 (Figure 5.2b) is considerably larger than the STD of the DART simulated BRF of 0.02, especially at longer wavelengths where it increases up to 0.06 for PARAS, but remains the same for DART.

A cross-comparison between PARAS BRF and DART BRF values shows that the cause of these differences is a higher sensitivity of PARAS simulations to the specified LAI values (Figure 5.2a). Overall, the obtained relationship between DART and PARAS BRF is non-linear ($R^2=0.56$) with an RMSE equal to 0.04, where the contribution from RMSEs prevails over the RMSEu, which indicates that the deviation is not random, but of a systematic nature. A closer look at the LAI dependency reveals that the PARAS BRF is systematically higher than the DART BRF for LAI lower than 5 (simulations start at an LAI of 3, cf. Table 5.2), while for $LAI \geq 7$ the deviation between models decreases considerably. The cross-comparison per LAI in Table 5.3 shows a linear relationship between both models for all cases ($R^2=0.99$), suggesting that canopy RT modelling of both models is comparable, especially for $LAI \geq 7$ where a nearly 1:1 relationship between BRF of both models resulted in RMSEs ≤ 0.01 (RMSEu=0). However, if $LAI < 7$ slope decreases and RMSE increases with decreasing LAI.

The simulated BRF is expected to be dependent on LAI and partially also on BAI of the canopy woody elements (Malenovský et al. 2008), mainly at longer wavelengths where absorption by foliar pigments is less significant. Our PARAS BRF estimates are, however, systematically overestimated when compared to the space borne CHRIS-PROBA observations. As already mentioned in Chapter 4 (Rautiainen et al. 2012), the photon recollision probability theory (p) relies on multiple scattering by canopy structural features, and therefore an uneven distribution of photon-needle interactions or a larger simulated contribution of the canopy woody elements than in reality

can possibly result in an overestimation of the BRF by the model. Thus, a lower LAI combined with a higher BAI might produce a higher BRF simulated by PARAS for the studied forest canopy. This explanation is also supported by the fact that DART-PARAS BRF differences appear to be stronger at red-edge wavelengths (701-720 nm), where the photon scattering dominates over the photon absorption by photosynthetically active foliar pigments. Additionally, differences in parameterization of the needle optical properties can play a role in the simulated BRF. Needle-leaf OPs for DART are derived and specified per vertical level (upper, transitional, and lower crown) of a tree crown, whereas a single weighted average of the reflectance and transmittance functions corresponding to 9 needle-classes (see Section 5.2.3.3) is used to compute the representative needle-leaf albedo in PARAS. The latter is subsequently combined with the bark spectrum by taking into account the stand LAI and BAI proportions as the averaging weights (see Section 5.2.3.3). Since DART leaf OPs are not being averaged, a small inaccuracy in parameterization of the PROSPECT model for the upper crown levels may potentially result in the systematic discrepancy observed in Figure 5.2.

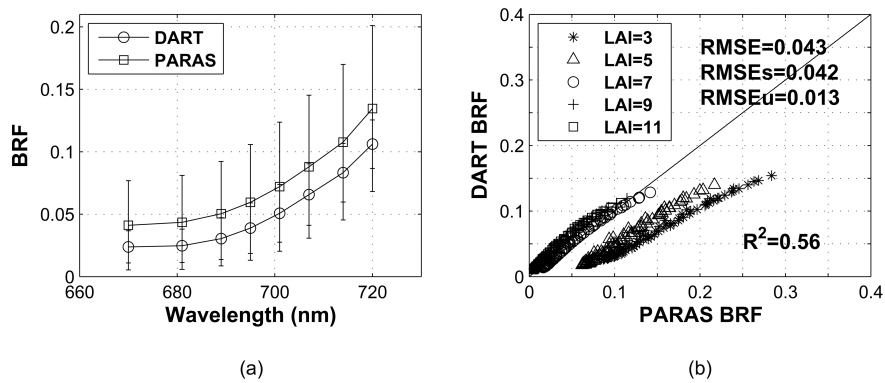


Figure 5.2 Comparison of PARAS and DART simulated BRF. (a) shows PARAS and DART BRF, averaged over all LAI (m^2m^{-2}) and Cab ($\mu g\ cm^{-3}$) values per simulated spectral band. (b) shows the comparison between PARAS BRF and DART BRF per LAI. R^2 : the coefficient of determination of the overall linear function; RMSE: root-mean squared error (Equation 5.6); $RMSE_s$: systematic RMSE (Equation 5.7); and $RMSE_u$: unsystematic RMSE (Equation 5.8).

Table 5.3 Comparison of PARAS and DART simulated BRF per input LAI value (i.e. LAI between 3 and 11 in steps of 2 m^2m^{-2}).

LAI	Linear relationship	R ²	RMSE	RMSEs	RMSEu
3	$\text{BRF}_{\text{DART}} = 0.7 \cdot \text{BRF}_{\text{PARAS}} - 0.03$	0.99	0.08	0.08	0.00
5	$\text{BRF}_{\text{DART}} = 0.8 \cdot \text{BRF}_{\text{PARAS}} - 0.04$	0.99	0.05	0.05	0.00
7	$\text{BRF}_{\text{DART}} = \text{BRF}_{\text{PARAS}}$	0.99	0.00	0.00	0.00
9	$\text{BRF}_{\text{DART}} = 1.1 \cdot \text{BRF}_{\text{PARAS}} + 0.01$	0.99	0.01	0.01	0.00
11	$\text{BRF}_{\text{DART}} = 1.1 \cdot \text{BRF}_{\text{PARAS}} + 0.01$	0.99	0.01	0.01	0.00

A strong sensitivity of PARAS BRF to LAI variation can also be observed after applying the continuum removal transformation (Figure 5.3a). The PARAS continuum-removed BRF between 670-720 nm is significantly depending on both LAI as well as Cab. Conversely, Figure 5.3b demonstrates that for DART the BRF after continuum-removal is only slightly influenced by LAI, while it is maintaining a systematic response towards Cab, especially for bands with wavelengths ≥ 695 nm. The continuum removal of BRF spectral bands simulated for 670-720 nm by DART corresponds to a large extent with the results published for the BRF of sunlit crown pixels in similar airborne spectral bands by Malenovsky et al. (2013). The PARAS continuum-removed BRF is in general smaller than the DART continuum-removed BRF for $\text{LAI} < 7$, while the opposite trend is observed for $\text{LAI} \geq 7$.

Variability of the PARAS continuum-removed BRF is consequently greater than in the case of DART simulations. Moreover, the differences in continuum-removed BRF of all spectral bands simulated with PARAS for $\text{LAI} \leq 7$ and $\text{Cab} > 40 \mu\text{g cm}^{-2}$ are very small (Figure 5.3a) which might have negative implications on the sensitivity of indices for Cab and therefore on the accuracy of Cab estimates retrieved from the CHRIS-PROBA satellite image using the continuum-removal based optical indices, i.e. $\text{ANCB}_{670-720}$ and $\text{ANMB}_{670-720}$.

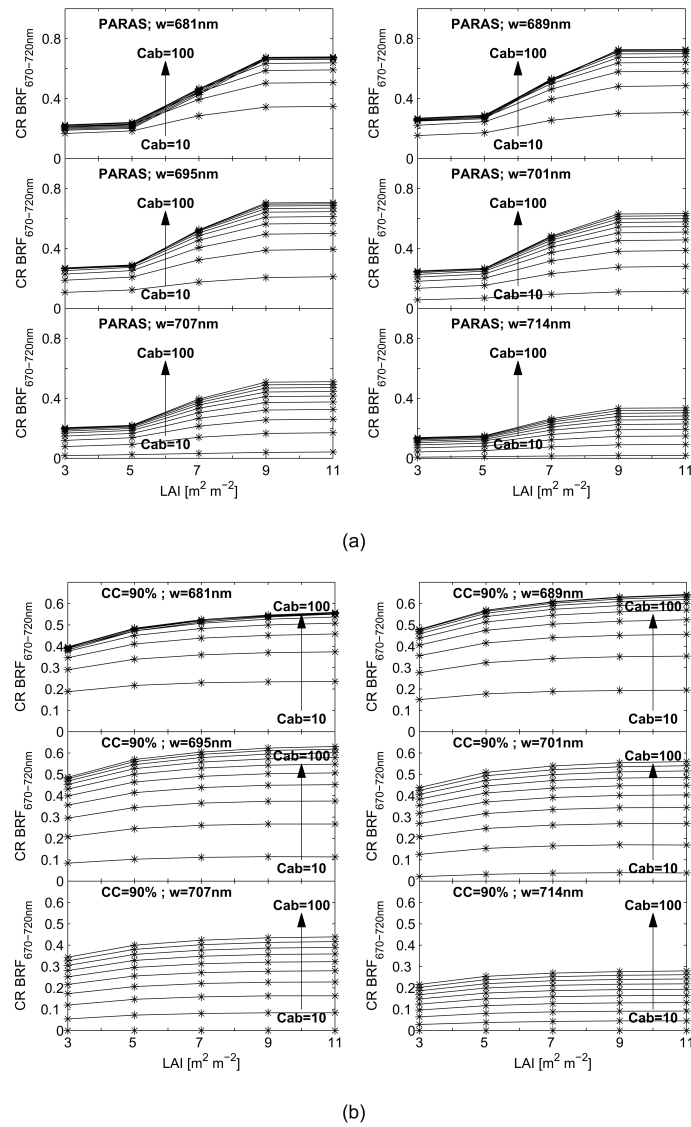


Figure 5.3 Sensitivity of the continuum-removed bidirectional reflectance factor between 670 and 720 nm to needle-leaf chlorophyll content (Cab) and LAI (m² m⁻²) for six spectral bands (681, 689, 695, 701, 707, and 714 nm) simulated by PROSPECT-PARAS (a), and by PROSPECT-DART (b). Each line corresponds to a simulated Cab level (Cab=10 to 100 in steps of 10 μg cm⁻²); 'w' refers to the wavelength in nm.

5.3.2 Empirical relationships between Cab and optical indices based on DART and PARAS model simulations

The Cab sensitive optical indices $ANCB_{670-720}$ and $ANMB_{670-720}$ were computed from the DART and PARAS simulated Look-Up-Tables and related statistically to the Cab model input. The empirical relationships corresponding to the best exponential functions established between Cab and the simulated indices are listed in Table 5.4 and plotted in Figure 5.4. Although, the functions are expressing the overall relationships as simulated by the two models, the index values are plotted per LAI to visualize how LAI affects the curve fitting (Figure 5.4).

An exponential equation was found to represent the best fit in a previous study on $ANCB_{670-720}$ by Malenovský et al. (2013). All functions fitted in our study are also of an exponential nature; nevertheless, their mathematical expressions slightly differ (Table 5.4). Malenovský et al. (2013) used the BRF of only sunlit spruce crown pixels of an AISA image for fitting, while here we consider the BRF of the spruce stand including shaded parts, assuming that sunlit spruce crowns are contributing dominantly to the BRF signal. The differences in statistical relationships for $ANMB_{670-720}$ and $ANCB_{670-720}$ are caused by their different ways of computation (normalization).

Results show that $ANMB_{670-720}$ is less sensitive to LAI variation than $ANCB_{670-720}$ for both models. On the one hand, the DART and PARAS based $ANMB_{670-720}$ shows very little confounding effect of LAI (Figure 5.4b and d) resulting in strong and stable Cab- $ANMB_{670-720}$ statistical relationships ($R^2=0.99$ and $R^2=0.95$, respectively). On the other hand, the PARAS based $ANCB_{670-720}$ index (Figure 5.4c) is strongly affected by the LAI, which resulted in a poor curve fitting result ($R^2=0.65$). However, for its DART counterpart the statistical relationship with Cab is considerably better ($R^2=0.97$), even though there is a small dispersion of $ANCB_{670-720}$ due to the LAI levels for Cab $\geq 50 \mu\text{g cm}^{-2}$ (Figure 5.4a).

The observed differences in performance of both indices generated by the same model are caused by their mathematical definition. While in the case of $ANCB_{670-720}$ the area under the continuum-removed BRF curve ($AUC_{670-720}$) is normalized to the continuum-removed BRF at the wavelength of 681 nm (CBD_{681} , Equation 5.3), in the case of $ANMB_{670-720}$ it is normalized to the continuum-removed BRF at the maximum band depth of the whole range 670-720 nm ($MBD_{670-720}$, Equation 5.5). As previously explained, the selection of the band at the fixed wavelength of 681 nm was based on its most stable response towards Cab changes when compared to all continuum-removed bands. Figure 5.3 shows that the continuum-removed BRF at 681 nm is still sensitive to LAI, especially to LAI values smaller than 7. The selection of the maximum band depth, which corresponded to 681 nm in 20%, to 689 nm in 60% and to 695 nm for the remaining 20% of simulated cases, is able to eliminate this LAI sensitivity. Based on

these results generated by both the DART and PARAS model it is concluded that the $ANMB_{670-720}$ is a more robust and stable Cab estimator than the $ANCB_{670-720}$.

Table 5.4 Empirical functions describing the relationship between simulated Cab and $ANMB_{670-720}$ and $ANCB_{670-720}$ indexes, respectively. R^2 : the coefficient of determination of the function; Adj R^2 : the degree-of-freedom adjusted coefficient of determination; FitStdErr: the fit standard error; F-ratio: the F-test ratio (tested at the probability level $p \leq 0.05$).

Index	Fitted Equation	R^2	Adj R^2	FitStdErr	F-ratio
$ANCB_{670-720}$ DART	$y = e^{-7.4505211+3.2571664\ln(x)}$	0.9677	0.9663	5.2682	1438.3000
$ANMB_{670-720}$ DART	$y = e^{1.7307696+0.000076322471x^3}$	0.9946	0.9944	2.1458	8911.0213
$ANCB_{670-720}$ PARAS	$y = 6.0004141e^{0.060745331x}$	0.6464	0.6313	17.4326	87.7373
$ANMB_{670-720}$ PARAS	$y = e^{0.93134314+0.000091989141x^3}$	0.9519	0.9499	6.4277	950.4265

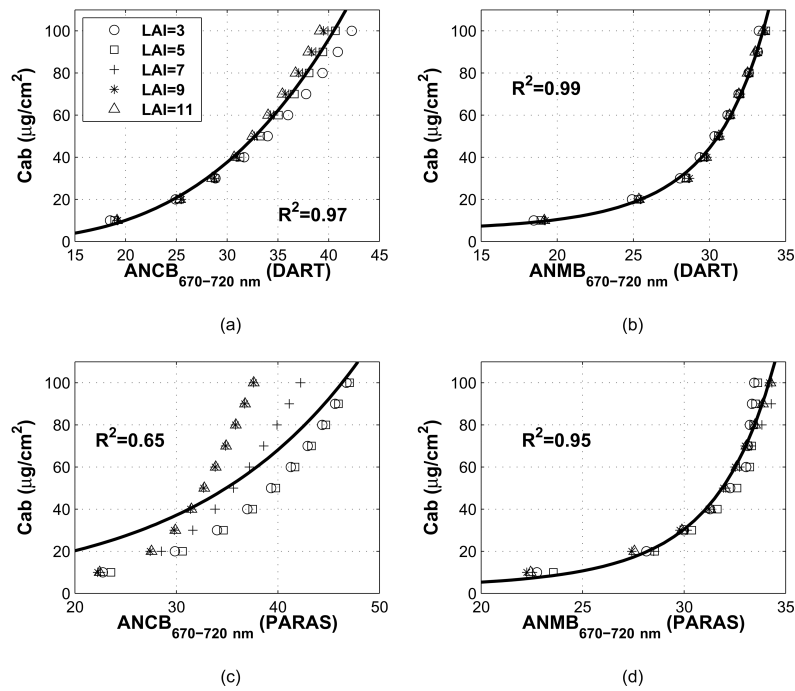


Figure 5.4 Relationship between Cab and respectively $ANCB_{670-720}$ (a and c) and $ANMB_{670-720}$ (b and d) computed from DART simulated BRF (a and b) and PARAS simulated BRF (c and d) for the LAI range 3-11 m^2m^{-2} in steps of 2. Index values corresponding to each LAI are represented by different symbols.

5.3.3 Cab estimated from CHRIS-PROBA data

5.3.3.1 Cab estimates retrieved by DART and PARAS based optical indices

The $ANCB_{670-720}$ and $ANMB_{670-720}$ indices computed from the atmospherically corrected and continuum-removed CHRIS-PROBA bands were used as inputs in the empirical functions established using the DART and PARAS simulations (Table 5.4) to estimate Cab of the immature Norway spruce stand under investigation. Figure 5.5 shows the histograms of Cab estimates retrieved from the CHRIS-PROBA image over the whole forest stand (176 image pixels) for the two indices and the two canopy RT models studied. Histograms show that in the case of the $ANCB_{670-720}$ (Figure 5.5a and c) the maximum frequency corresponds to Cab=49 $\mu\text{g cm}^{-2}$ for DART and 43 $\mu\text{g cm}^{-2}$ for PARAS. Similarly, in the case of the $ANMB_{670-720}$ (Figure 5.5b and d) the maximum frequency corresponds to Cab=66 $\mu\text{g cm}^{-2}$ for DART and 42 $\mu\text{g cm}^{-2}$ for PARAS. In addition, the range of estimated Cab is wider for DART than for PARAS. These differences in output of the models and indices were expected due to the variations in the established empirical functions. However, all the estimates are ranging within a physiologically plausible interval of Cab values published for Norway spruce needles in previous studies (e.g. Malenovsky et al. 2006).

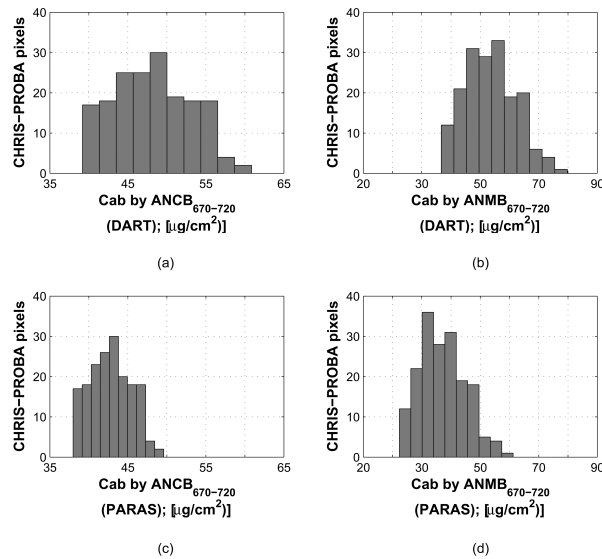


Figure 5.5 Histograms showing the number of CHRIS-PROBA pixels of the studied stand (total number 176 pixels) for Cab values estimated using the $ANCB_{670-720}$ empirical functions (a and c) and the $ANMB_{670-720}$ empirical functions (b and d) found for DART (a and b) and PARAS (c and d).

To indirectly validate the per-pixel CHRIS-PROBA Cab estimates, they were cross-compared with the Cab map produced from the airborne AISA image of the study area applying an ANN. Figure 5.6 and Figure 5.7 provide the results corresponding to ANCB₆₇₀₋₇₂₀ and ANMB₆₇₀₋₇₂₀ estimates of both RT models, respectively.

Subplot (a) in Figure 5.6 and 5.7 shows the one-to-one comparison between DART and PARAS. Cab estimated from the CHRIS-PROBA image using the ANCB₆₇₀₋₇₂₀-based empirical functions corresponding to the DART model versus the Cab estimates corresponding to the PARAS model (Figure 5.6a) show a strong linear relationship. A similar statistically significant linear relationship was found for the ANMB₆₇₀₋₇₂₀ (Figure 5.7a). ANCB₆₇₀₋₇₂₀ results reveal a smaller overall difference between DART and PARAS based Cab estimates (RMSE=5.8 $\mu\text{g cm}^{-2}$) than ANMB₆₇₀₋₇₂₀ results (RMSE=17 $\mu\text{g cm}^{-2}$). In both cases the error is mostly systematic (RMSEs>RMSEu), as one expects when comparing two models. The slope of the linear function is steeper for the ANCB₆₇₀₋₇₂₀ case, resulting in an increasing deviation between the two model results with increasing Cab. In case of the ANMB₆₇₀₋₇₂₀, a nearly 1:1 linear relationship with a systematic offset of 11 $\mu\text{g cm}^{-2}$ of DART Cab estimates with respect to PARAS ones was found.

The linear relationships signalize that radiative transfer is modelled in a similar way by both DART and PARAS; however, there is a systematic bias that results in higher Cab estimates for DART. The systematic deviation is driven by a higher sensitivity of the PARAS simulated BRF for LAI and subsequently also generated optical indices more sensitive for changing LAI. The PARAS BRF is systematically higher (average offset of 0.02, see Section 5.3.1) for low LAI values (LAI < 7), which results into a less statistically reliable empirical fit between Cab and optical indices (Figure 5.4). This effect was propagated into the Cab retrieval, where PARAS-based Cab estimates of a given pixel are systematically lower than DART-based estimates (Figure 5.7a). One may argue that this situation is caused by a systematic difference in parameterization of the models. A feature potentially responsible for this mismatch is the implementation of woody elements in each model. A previous study of Stenberg et al. (2013), which compared the forest radiation regimes simulated by a RT model from the PARAS “family” and by a detailed forest RT model (FRT; Kuusk and Nilson (2000)), demonstrated that inclusion of the BAI proportion in the photon recollision computation of PARAS (Equation 5.2) resulted in forest albedo values that were closer to those simulated by the FRT model. The next most probable reason is a different parameterization of

leaf optical properties. As already mentioned, the DART specification of leaf reflectance and transmittance is more detailed and specified per vertical crown level, whereas PARAS is upscaling a single weighted average of the leaf scattering albedos. Since DART leaf OPs are not being averaged, a seemingly small inaccuracy in parameterization of the PROSPECT model for the upper crown levels may potentially result in the systematic discrepancy observed in Figure 5.7.

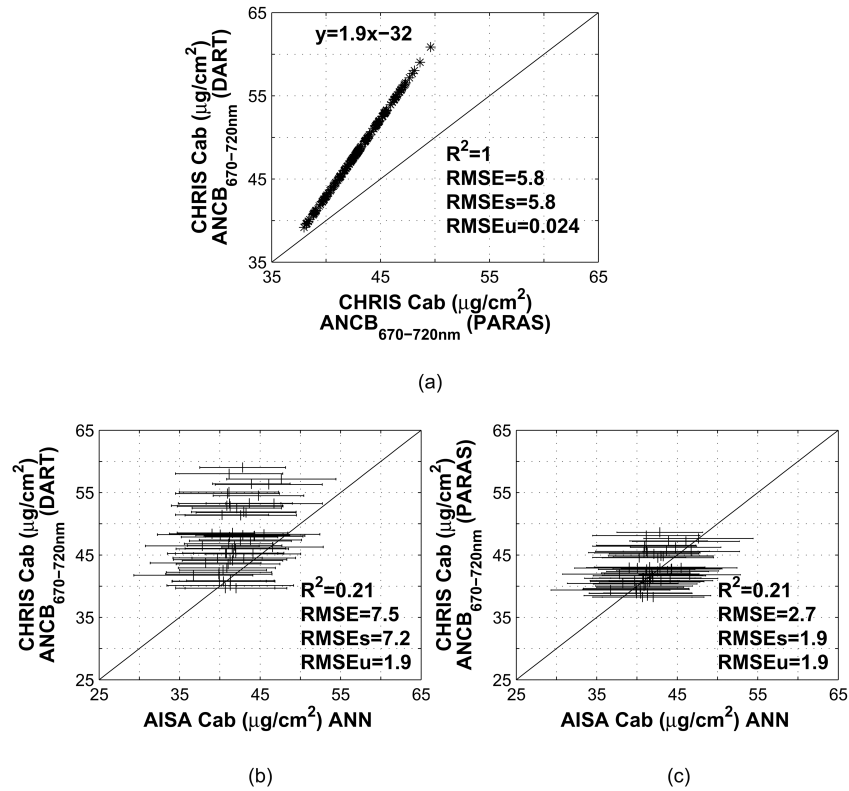


Figure 5.6 Scatter plot of needle-leaf chlorophyll content (Cab) estimated from the CHRIS-PROBA image using the ANCB₆₇₀₋₇₂₀ based empirical function corresponding to DART versus the same estimates corresponding to PARAS (a). Each point represents a CHRIS-PROBA pixel of the test forest stand. Lower graphs: comparison of leaf chlorophyll content (Cab) retrieved from the CHRIS-PROBA image using ANCB₆₇₀₋₇₂₀ derived from DART simulations (b) and PARAS (c) against the average Cab estimated from the AISA Eagle image using an artificial neural network (ANN). Horizontal bars correspond to the standard deviation of mean Cab extracted from the AISA image.

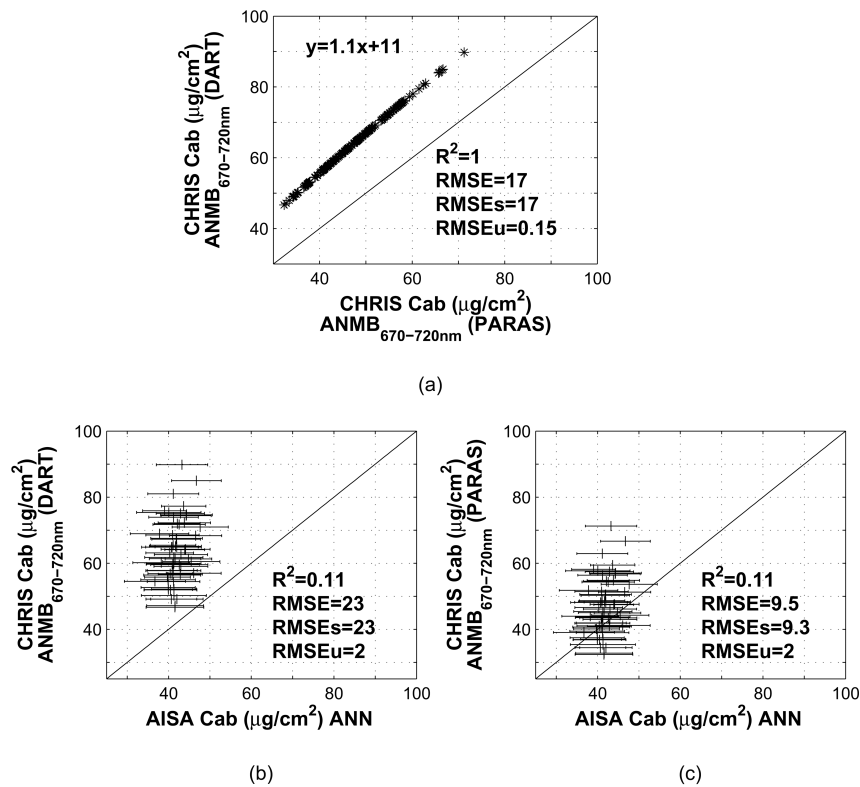


Figure 5.7 Scatter plot of needle-leaf chlorophyll content (Cab) estimated from the CHRIS-PROBA image using the ANMB₆₇₀₋₇₂₀ based empirical function corresponding to DART versus the same estimates corresponding to PARAS (a). Each point represents a CHRIS-PROBA pixel of the test forest stand. Lower graphs: comparison of leaf chlorophyll content (Cab) retrieved from the CHRIS-PROBA image using ANMB₆₇₀₋₇₂₀ derived from DART simulations (b) and PARAS (c) against the average Cab estimated from the AISA Eagle image using an artificial neural network (ANN). Horizontal bars correspond to the standard deviation of mean Cab extracted from the AISA image.

5.3.3.2 Validation CHRIS-PROBA derived Cab estimates

Subplots (b) and (c) in Figure 5.6 and Figure 5.7 show the relationship between Cab values extracted from the validation polygons superimposed over the CHRIS-PROBA image compared to the Cab values extracted from the same polygons overlaying the AISA Cab map. The AISA Cab values were estimated using the ANN approach as described in Malenovský et al. (2013) and averaged per polygon. Cab estimations plotted in Figure 5.6 were made through the ANCB₆₇₀₋₇₂₀ empirical relationships obtained from DART and PARAS.

Quantitatively the Cab estimation based on PARAS is closer to the airborne Cab map than the same one based on DART (RMSE = $2.7 \mu\text{g cm}^{-2}$ and $7.5 \mu\text{g cm}^{-2}$, respectively). The RMSE for DART is dominated by a systematic error (RMSEs), which indicates that a systematic change in DART model parameterization would be able to improve the performance of the ANCB₆₇₀₋₇₂₀ retrieval procedure. Validation of the ANMB-counterpart (Figure 5.7b and c) showed that the Cab point clouds are similar in shape, with DART results being higher by a constant offset of $11 \mu\text{g cm}^{-2}$. This was expected from the nearly linear relationship between ANMB₆₇₀₋₇₂₀ estimates of both models with only an offset (Figure 5.7a). This situation resulted in a lower RMSE for PARAS (RMSE = $9.5 \mu\text{g cm}^{-2}$) than for DART (RMSE = $23 \mu\text{g cm}^{-2}$). For both models, the same poor relationships with the AISA-ANN Cab occur, with the RMSEs dominating the RMSE. These results suggest that although the ANMB₆₇₀₋₇₂₀ demonstrates closer and LAI independent relations with simulated Cab classes (Figure 5.4) it is not necessarily producing more accurate estimates than the ANCB₆₇₀₋₇₂₀.

At this point we have to stress the fact that the AISA airborne Cab map, even though being created at a higher spatial resolution of 0.4 m and thus expectedly of a high accuracy, is used for the validation by simple averaging of Cab estimates at 0.4 m pixel size, which is essentially a linear mixing approach. Since the BRDF of a 17 m CHRIS-PROBA pixel will be defined by a non-linear reflectance mixture of heterogeneous sunlit and shaded surfaces, the resulting Cab estimates may not necessarily fully resemble the Cab values retrieved and averaged at a high spatial resolution. In addition, the airborne Cab retrieval was carried out only for sunlit pixels of Norway spruce crowns. As explained in Malenovsky et al. (2013) this methodological decision was taken in order to exclude the shaded pixels with a low signal-to-noise ratio that cause an underestimation of the retrieved Cab. Applying this at a spatial resolution of 0.4 m is feasible, because a single spruce crown is always assembled from several pixels. However, the hypothesis assuming that these spectrally pure sunlit pixels, covering approximately half of the forest canopy, are representative enough to be compared with Cab estimate of a CHRIS-PROBA pixel, which is composed by several spruce crowns, has not been tested yet. Such a test, being certainly important for validation of satellite estimates using airborne products, was beyond the scope of this study.

5.4 Conclusions

This study demonstrates that retrieval of needle-leaf chlorophyll content from the continuum-removed reflectance of red and red-edge wavelengths (670–720 nm) using a leaf radiative transfer model coupled to a canopy model based on the photon-recollision probability (PARAS) can lead to comparable results as achieved with a canopy 3D radiative transfer model (DART). This suggests that, despite less input parameters and its simplicity, PARAS presents an alternative to more detailed and complex 3D radiative transfer canopy models when applied to satellite imaging spectroscopy data with a spatial resolution of tens of meters.

Results of the radiative transfer modelling revealed that the PARAS simulated BRF is more sensitive to predefined LAI parameters than the BRF simulated with DART in the selected wavelength range. This sensitivity, which was observed especially for PARAS simulations with LAI lower than 7, can potentially be attributed to a higher impact of optical properties and geometry of woody elements on the canopy BRF. A systematically higher BRF between 670 and 720 nm simulated by PARAS led to a reduced performance of the statistical fit between C_{ab} and the studied chlorophyll sensitive optical indices based on the reflectance continuum removal.

In general, the relationship between C_{ab} and the $ANMB_{670-720}$ optical index, simulated for the spectral and spatial characteristics of a CHRIS PROBA satellite image, was statistically more robust than the similar relationship established for the $ANCB_{670-720}$ index. This difference can be attributed to different mathematical definitions of both indices. The C_{ab} values retrieved from the CHRIS PROBA imaging spectroscopy image using the PARAS- $ANMB_{670-720}$ algorithm were systematically lower for our study area than the corresponding estimates based on the DART- $ANMB_{670-720}$ approach, following a nearly one-to-one relationship with only an offset of $11 \mu\text{g cm}^{-2}$. Such a strong linear relationship implies that the modelling of canopy RT of both models is similar and the systematic offset might be caused by differences in model parameterizations. The relationship between C_{ab} estimates produced by both models based on the $ANCB_{670-720}$ was also linear, although the differences were systematically increasing with increasing C_{ab} .

Finally, for both indices C_{ab} estimations based on the PARAS model were closer to the C_{ab} values extracted from an AISA image using an inversion approach based on an artificial neural network. Nonetheless, empirical relationships between C_{ab} and the indices were more robust for DART than for PARAS due to the LAI sensitivity of the latter. Interestingly, although

empirical functions fitted to $ANCB_{670-720}$ were statistically less robust than for $ANMB_{670-720}$, the $ANCB_{670-720}$ approach for both models yielded lower RMSEs values computed between the CHRIS-PROBA Cab estimates and the airborne Cab map.

The findings indicate that further analysis on the impact of the optical parameterization of needles and woody elements might potentially reduce the bias between the resulting BRF simulated by both models.

Acknowledgements

Authors acknowledge the support provided by Dr. Radek Pokorný concerning the acquisition and processing of field data acquired with the LAI-2000 Plant Canopy Analyzer. The contribution of Michael Schaepman is supported by the University of Zurich Research Priority Program on 'Global Change and Biodiversity' (URPP GCB).

Chapter 6

Synthesis

6.1 Main results

This thesis contributes to improving the interpretation of the remotely sensed optical signal reflected from coniferous canopies. Recognizing the need for a better adaptation of RS methods to such spatially heterogeneous and structurally complex canopies (Chapter 1), the main objective of this thesis is to bridge scaling gaps in the application of RS methods to studies on coniferous canopies by addressing identified problematic issues and by exploring the application of approaches that simplify the way the structural complexity of such an environment is tackled when using canopy-level radiative transfer approaches. Three main canopy levels based on the identified gaps were defined for the analysis: (needle) leaf level (Chapter 2 and 3); shoot level (Chapter 4) and canopy level (Chapter 5). At leaf level this thesis contributes to a better understanding and to minimizing the uncertainties and errors related to leaf optical measuring methods adapted for needle leaves. The needle spectral signal is, however, quickly transformed due to scattering driven by the complex clumped structure of coniferous forests. This clumping makes the description of the canopy RT complex and encourages the search for simplified yet robust approaches. Thus, subsequent steps in this thesis focus on one such simplified approach, known as the recollision probability theory (“p-theory”), applied at two hierarchical levels, i.e., shoots (Chapter 4) and the whole canopy (Chapter 5). Each of these four chapters concentrates on one of the research questions presented in Section 1.6, which are answered below and followed by a discussion on the main results.

6.1.1 Research question A: Theoretical review of narrow-leaf OP measurements

- A. What are the shortcomings and uncertainties in measurement methods of optical properties (OPs) of narrow leaves?

This research question was addressed in Chapter 2. The aim of this chapter was to review the state of the art and recent developments in measurement methods for narrow leaf optical properties. This analysis is important because

the small size of narrow leaves, e.g. coniferous needle leaves, requires adaptations from conventional measuring techniques of plant leaf optical properties (OPs), i.e. reflectance and transmittance measured by means of a single beam integrating sphere coupled to a spectroradiometer. Yet, despite the global ecological relevance of coniferous tree species with predominantly non-flat needle-shaped leaves, and even though OPs of coniferous needles are extensively used by the remote sensing community, there are only few techniques available adapted to measuring their optical properties and little knowledge exists about their related errors. We focused on methodological shortcomings and uncertainties, with special attention to non-flat non-bifacial coniferous needle leaves (e.g., needles of Norway spruce).

Based on literature we were able to identify three predominantly used approaches. These were those suggested by Hosgood et al. (1995), Harron (2000), and Daughtry et al. (1989), with improvements by Mesarch et al. (1999). Among all, the method by Mesarch et al. (1999) (further referred to as *Mesarch's* method) was the most suitable one since it was both systematic and easily adaptable to narrow leaves of different kinds, e.g. different coniferous species and flat narrow leaves (e.g. grasses).

In *Mesarch's* approach a single layer of needles was placed side-by-side at an even distance and fixed between two sample holder plates, which are tightened and positioned at the sample port of the integrating sphere. Subsequently, the recorded signal has to be corrected for the effect of the air gap fraction (GF) between the needles. The correction is based on the linear relationship assumed between the recorded sample signal and the GF. It requires a technique for accurately estimating the GF, which in this case is done through processing of a digital image of the evenly spaced needle layer placed inside the sample holder.

Revisiting the limitations of *Mesarch's* method revealed further potential for improvements. The main limitations found were:

- i. *Effect of multiple scattering between needles is not corrected.* The method worked well for flat narrow leaves, but for non-flat needle leaves (representing most coniferous species) small GFs improved accuracy of the transmittance signal while it increased the error in reflectance. This effect was attributed to the multiple scattering between the needles.
- ii. *Sample holder effect is unknown.* Although there is no direct interaction between the illumination beam and the sample holder, the holder has a significant thickness that might indirectly influence the

signal. It increases the distance between the sample and the inner sphere wall, increasing the probability of absorptions at the port edge (Merzlyak et al. 2002). In addition, multiple scattering enhanced by the non-flat cross section of the needles can potentially redirect some of the photons towards the sample holder plates.

- iii. *Effect of image acquisition and processing settings is unclear, e.g.,* the effect of the threshold applied for separating the air needle interface during the GF estimation from digital images.
- iv. *Method optimization is based on a non-directly computable quantity: the GF.* The calculation of the GF prior to the measurement is not visually straightforward requiring extra time during sample preparation that might lead to further biological degradation of the sample before the OPs measurement is finished. Conversely, if the optical measurements are done without knowing the sample GF, a significant number of measurements might potentially be discarded after the processing due to an unacceptable large uncertainty caused by too large or too small GFs, leading to a substantial reduction of overall usable data.

Given the increasing importance of scaling-based approaches in combination with the ecological importance of ecosystems dominated by non-flat needle-shaped leaves, improvements to the error-prone *Mesarch's* method are already overdue. Thus, in the following chapter we propose an experimental set-up improving the original method of Mesarch et al. (1999), where the objective is to investigate the above addressed uncertainties.

6.1.2 Research question B: experimental set-up and error analysis of narrow-leaf OP measurements

- B. What is the influence of the sample holder, the needle cross-section shape and the mutual distance between the needles on the measured leaf reflectance (R) and transmittance (T) factors?

This research question was addressed in Chapter 3. In this chapter we proposed an experimental set-up optimizing established needle-leaf OPs measurement approaches by systematically minimizing their uncertainties. The approach is based on the method of Mesarch et al. (1999), presented in Chapter 2. The measuring protocol was described in detail in Chapter 3. We focus on analysing the influence of three factors on the measured signal: the presence of the sample holder, the specific needle cross-section shape, and the distance between

the needles composing a sample. The hypotheses are that both the holder presence and the multiple scattering, driven by the cross-section and the distance between needles, have an effect on the measured signal, which is not fully corrected when using *Mesarch's* method. Regarding the multiple scattering, the hypotheses are: i) that the rhomboidal non-flat cross-section of needles increases multiple scattering between the measured needles, which triggers a direct effect on the measured signal; and ii) that decreasing the distance between needles (smaller air gaps within the sample) increases the probability of multiple scattering, which consequently affects the measured signal.

First, the sample holder cannot be excluded, because it fixes the position of the small sized needles in front of the sample port of the integrating sphere during the optical measurements. The use of the sample holder caused a signal underestimation, especially in transmittance mode and in the case of silicon material (i.e. broad-leaf-like material corresponding to non-flat needles). This was attributed to absorption of a fraction of the transmitted light around the sample port edge due to the external position of the integrating sphere ports (Merzlyak et al. 2002). This causes the outer wall of the sphere to be a few millimetres away from the reflecting inner wall, and with the use of the sample holder the result is a longer distance, and presumably a stronger optical effect. Thinner holders (<1 mm) were bending when adjusted to firmly hold the Norway spruce needles, and therefore were not suited for this type of measurements. Overall, the minimum RMSE for measured reflectance and transmittance was 1% and 2% for flat needles, and 1% and 4% for non-flat needles, respectively. These results corresponded to an integrating sphere configuration that was based on the original *Mesarch's* approach and further updated by adding a holder during the reference signal measurements.

Secondly, we evaluated the effect of the multiple scattering between needles, which is influenced by the shape of the needle cross-section and the distance between needles. This was assessed at two steps of our measuring method, both of which provide the inputs to *Mesarch's* GF correction formulae, where this multiple scattering is not explicitly considered: the sample scanning (required for the GF estimation) and the sample optical measurements. In addition, we compared the signal after *Mesarch's* GF correction to the corresponding broad-leaf reference signal. Results showed that:

- i. **Needle cross-section** affects the signal, especially in needles with a rhomboidal cross-section. First, it makes rhomboidal needles look optically thinner during digital scanning than they are in reality (step 1). Optimizing scanning and processing settings cannot fully compensate for

this effect (RMSE=10% after optimization). Conversely, optimization for flat and squared needles reduces the error to an average value of 2-3%. Secondly, it affects the measured optical signal (step 2), for which the relative error increased from flat- to squared- to rhomboidal-needle samples for a fixed distance between needles, especially for transmittance measurements. With no multiple scattering, similar results should appear for flat and squared needle cross-section samples since both have the same gap fraction set (same needle thickness, same needle area projection). Third, the cross-section affects the signal after GF correction, where errors are higher for samples with a non-flat cross-section, especially in transmittance mode. *Mesarch's* formula overcorrects the transmittance of flat needles (method inherent error, Mesarch et al. (1999)). Despite this, the GF corrected transmittance of non-flat needles is overestimated, suggesting that multiple scattering effects increase the signal beyond this overcorrection. Using the sample holder, which caused a decrease of the transmittance signal, compensates partially for this effect.

- ii. ***Distance between needles:*** in general, lowest errors occurred for the smallest distance, i.e. half the width of a needle, while increasing the distance increased the gap effect at the expense of the quality of the signal from the needle elements. The exception was found for rhomboidal needles for which errors were higher at the smallest distance, especially in transmittance mode. In the latter case, the smallest distance was less than half the needle width, indicating that for rhomboidal needles less than half the needle width reinforces multiple scattering and causes bias in the measurements. This suggests that half the needle width might be the optimal distance between needles at which signal is still negligibly affected by multiple scattering induced by neighbour needles that are too close to one another. Conversely, the maximum distance (one and a half the needle width) is to be considered as too big (i.e. gap effect deteriorates needle signal quality). After GF correction, the negative effect observed for rhomboidal needles at the smallest distance disappeared, indicating lower sensitivity to this effect after the GF correction. Overall, gap distances tested in this study had a weaker effect than the cross-section, especially for optical transmittance measurements (average error variation of 3% compared to a variation of ~14% induced by the cross-section).

Finally, we tested the linear relationship between the non-GF-corrected signal and GF, which is the basis for *Mesarch's* GF-correction formulae. In case of rhomboidal cross-section needles the relationship was non-linear suggesting multiple interactions of the incoming light with sample needles, which is distorting the expected linear relationship otherwise observed for flat needles (Mesarch et al. 1999). For this reason, *Mesarch's* formulae, based on the assumption of a linear GF correction, are inaccurate in computing the OPs of non-flat needles

Overall, the effect of a non-flat cross-section appeared to have a greater influence than the gap distances tested in this study. The final error obtained after GF correction and after optimizing *Mesarch's* method is 1% in reflectance mode and 5-7% in transmittance mode if the needles are flat; 3-5% in reflectance and 9-12% in transmittance for squared cross-section needles; and 4-6% in reflectance and 9-17% in transmittance for rhomboidal cross-section needles. In general, more accurate OPs can be achieved when the distance between measured needles is about half the needle width. Finally, the results of this study pointed out that approaches designed to more comprehensively measure OPs of non-flat coniferous needle samples should take into account multiple scattering between the measured leaves as currently done in radiative transfer modelling.

6.1.3 Research question C: *p*-approach at shoot level

- C. Is it possible to compute shoot albedo (directional-spherical reflectance factor) through the *p*-theory approach by using only one structural parameter: the spherically averaged shoot silhouette to total needle area ratio (STAR)?

This research question was addressed in Chapter 4. The aim of this chapter was to test empirically the hypothesis that it is possible to upscale needle albedo to shoot albedo (directional-spherical reflectance factor) using only one structural parameter: the spherically averaged shoot silhouette to total needle area ratio (STAR). Testing this empirically is important since it represents fundamental underlying assumptions of the photon recollision probability *p* (i.e., first, that *p* can be defined at different hierarchical levels and second, that at shoot level *p* is linearly related to this measurable structural property described as STAR). This only has been tested theoretically (Smolander and Stenberg 2003, 2005).

Comparison between modelled and measured shoot albedos showed that the model for upscaling from needle to shoot spectral albedo using STAR performed well in the visible (VIS) and shortwave infrared (SWIR) regions (i.e. for shoot albedo values smaller than 0.5) but overestimated shoot spectral albedo slightly in the near infrared (NIR; i.e. shoot albedo values >0.5). The better performance of the model at VIS-SWIR was attributed to two main reasons: (a) better radiometric performance of the spectroradiometer at VIS and SWIR (1400–1800 nm) and thus better quality of spectral data; and (b) the enhanced sensitivity to model parameter errors in NIR. In addition, another reason could be the theoretically lower contribution of specular reflectance occurring in the SWIR, which decreased by 25% (0.03 at 2000 nm) when compared to the stable value shown in the VIS-NIR (about 0.04 in absolute reflectance units). That would mean more diffuse scattering taking place inside the needle in the SWIR than in the VIS-NIR and consequently a better performance of the photon recollision probability theory (which described diffuse scattering). This statement is, however, based on the wax refractive index from the PROSPECT leaf RT model, since this index drives leaf specular reflectance, but lacks sufficient empirical support (i.e. measurements of specular and diffuse components for the selected wavelength range).

In general, mismatch between model and measured shoot albedos is based both on the definition of photon recollision probability and on measurement uncertainties. First, the relationship between p and STAR is formulated for the photon recollision probability under absolutely diffuse illumination (i.e. all needle surfaces are uniformly irradiated) and diffuse (Lambertian) scattering. Neither condition is perfectly fulfilled in our experiment. Secondly, measurement related noise and stray light contributions (mainly from random noise of the spectroradiometer, stray light from equipment and inaccuracies from the Spectralon panel used in shoot signal normalization) resulted in a total uncertainty in shoot albedo of at least 5% (at twice the standard deviation level).

Finally, better fits were found for shoots with higher STAR, where a high STAR means a more even spatial distribution of photon–needle interactions than a shoot with a lower STAR (<0.15 , i.e. sparser shoots). Discrepancy between measured and predicted spectral albedos for sparser shoots could possibly result from the poor performance of the photon recollision probability theory (due to the uneven distribution of photon–needle interactions) or from a larger influence of the twigs (bark). This result implies

that the upscaling model tested in this paper performs the best in canopies with an even distribution of radiation.

Overall, the study showed that it is possible to scale from needle up to shoot spectral albedo using only the shoot structural characteristic defined by STAR with best results in the VIS and SWIR regions. As STAR is linearly related to p , it is possible to apply the upscaling model as part of RT models.

6.1.4 Research question D: *p*-approach at canopy level

- D. How different is the leaf chlorophyll content of a Norway spruce stand estimated from satellite imaging spectroscopy data using a simple p -theory based approach from the one estimated using a detailed and computationally more demanding 3D canopy RT model?

This research question was addressed in Chapter 5. The objective of this paper was to compare the performance of the canopy model PARAS (which presents a simple parameterization of canopy structure based on the photon recollision probability) to the canopy model DART (an RT model based on a detailed 3D structural description of a forest, which is computationally more demanding), when being employed in estimating coniferous needle-leaf chlorophyll content C_{ab} from satellite imaging spectroscopy data with a spatial resolution of about 20 m. The needle-leaf chlorophyll content (C_{ab}) of a Norway spruce stand (*Picea abies* /L./ Karst.) was estimated from a CHRIS-PROBA satellite image. First, top-of-canopy bidirectional reflectance factors (BRF), simulated by the leaf radiative transfer (RT) model PROSPECT coupled with the DART or PARAS canopy reflectance models, were used to calculate two optical indices, $ANCB_{670-720}$ and $ANMB_{670-720}$. Subsequently, empirical relationships established between the optical indices and the needle-leaf C_{ab} content were applied on the CHRIS-PROBA image of the study area to retrieve a map of C_{ab} estimates.

Results of the radiative transfer modelling revealed that the PARAS simulated BRF is more sensitive to predefined LAI parameters than the BRF simulated with DART in the selected wavelength range (670-720 nm). This sensitivity, which was observed especially for PARAS simulations with LAI lower than 7, can potentially be attributed to a higher impact of optical properties and geometry of woody elements on the canopy BRF. An uneven distribution of photon-needle interactions or a larger simulated contribution of the canopy woody elements can possibly result in an overestimation performance of the model (Chapter 4).

A systematically higher BRF between 670 and 720 nm simulated by PARAS led to a reduced performance of the statistical fitting between Cab and the chlorophyll sensitive optical indices based on the reflectance continuum removal. Exponential empirical relationships fitted using the ANMB₆₇₀₋₇₂₀ were more robust, especially for the DART model. ANCB₆₇₀₋₇₂₀ presented a lower performance, especially for PARAS, due to the sensitivity of the index to LAI variation (in particular LAI < 7). The difference between the performance of the indices can be attributed to their different mathematical definition (e.g., band used for the normalization).

An inter-comparison between Cab estimates of both RT models and optical indices showed a strong linear correlations ($R^2 = 1.0$), with a nearly perfect linear relationship between the PARAS and DART retrievals using the ANMB₆₇₀₋₇₂₀ index, although a bias was present (slope = 1.1, offset = 11 $\mu\text{g cm}^{-2}$). The relationship established between Cab estimates based on the ANCB₆₇₀₋₇₂₀ index was also linear, although the difference was increasing with increasing Cab values resulting in a steeper slope of the function.

The linear relationship shown for the Cab estimates of DART and PARAS using the ANMB₆₇₀₋₇₂₀ index suggests that the modelling of canopy RT by both models is similar and the systematic offset might be potentially caused by differences in the implementation of woody elements in each model or by a different parameterization of leaf optical properties. The specification of leaf reflectance and transmittance in DART is more detailed and specified per vertical crown level, whereas PARAS is using a single weighted average of the leaf scattering albedos. Since leaf OPs of DART are not being averaged, a seemingly small inaccuracy in parameterization of the PROSPECT model for the upper crown levels may potentially result in the systematic discrepancy.

Comparison of the Cab maps with the one produced by an artificial neural network applied to an airborne image of the studied forest stand acquired with an AISA Eagle sensor showed a better performance of PARAS retrievals with a RMSE = 2.7 $\mu\text{g cm}^{-2}$ for the ANCB₆₇₀₋₇₂₀ approach and a RMSE = 9.5 $\mu\text{g cm}^{-2}$ for the ANMB₆₇₀₋₇₂₀ approach. DART retrievals showed larger differences with a RMSE = 7.5 $\mu\text{g cm}^{-2}$ for the ANCB₆₇₀₋₇₂₀ approach and a RMSE = 23 $\mu\text{g cm}^{-2}$ for the ANMB₆₇₀₋₇₂₀ approach. Although better validation results were obtained for PARAS, DART empirical relationships were more robust. For most estimations the systematic RMSE was dominating over random errors, indicating that retrieval algorithms potentially can be further improved.

Therefore, a further analysis elaborating on the impact of parameterization differences in each model is recommended. Despite of this conclusion, the results indicate that for the spatial resolution studied here, the simpler RT model PARAS can be applied to retrieve plausible needle-leaf Cab estimates from satellite imaging spectroscopy data.

6.2 General conclusions

This thesis identified and addressed specific gaps in the modelling and interpretation of top of canopy reflectance from structurally complex coniferous forests. The main conclusions drawn from this work are:

- i. Quantifying errors and minimizing related uncertainties of techniques measuring OPs of narrow leaves is needed in order to improve the reliability of empirical spectral datasets used for validation and calibration of RS models.
- ii. Multiple scattering between non-flat needles has a non-negligible effect on the optical signal when measured using a standard spectroradiometer coupled to a single-beam integrating sphere and following the method suggested by Mesarch et al. (1999). Due to this, the assumed linear relationship between the measured sample signal and the sample gap fraction does not hold for transmittance measurements of non-flat needles. The approaches designed to measure OPs of non-flat coniferous needle samples should take into account multiple scattering caused by a non-flat cross-section shape of the needles as well as the effect of sample holder presence.
- iii. Scaling needle spectral albedo to the shoot level using the shoot structural characteristic defined by STAR is feasible for the VIS and SWIR spectral regions. However, the photon recollision probability scaling approach was less accurate for sparse shoots (STAR <0.15) with an uneven distribution of photon–needle interactions and a larger influence of the twig bark.
- iv. For the spatial resolution corresponding to CHRIS-PROBA (17 m), the simpler RT model PARAS can be applied to retrieve plausible needle-leaf Cab estimates from satellite imaging spectroscopy data with less intensive RT model parameterization and reduced computational power than when using a model like DART.

6.3 Reflection

This thesis contributes in closing scaling gaps identified in the interpretation of the remotely sensed optical signal reflected from coniferous canopies. *At needle level*, an experimental set-up optimizing established needle-leaf OPs measurement approaches by systematically minimizing their uncertainties was presented. Despite the technique optimization, non-negligible errors in the transmittance signal of non-flat coniferous needles remained. This suggested the need for including multiple scattering effects in the current correction algorithms presented by *Mesarch's* methods (Chapter 3). However, modification of the correction algorithms corresponding to this method is not straightforward due to the non-linear relationship between signal and gaps. Thus, a more extended dataset of empirical measurements is recommended previous to development of new algorithms. Due to the highly demanding nature of this type of optical measurements, in terms of time and manpower, only the minimum reliable number of samples and scenarios was presented in this thesis. Thus, only the optimization of measurement steps and quantification of the related errors was presented.

An optically stable material was used to ensure that measured reflectance and transmittance factors of the same material, either as artificial needles or as the corresponding broad-leaf reference, would result in similar material uncertainty (Chapter 3). This allowed the quantification of the errors related to the measuring methods, but implied that needles used for the analysis are an approximation of real needles. Real needles are never as regular as artificial ones (e.g., they have varying thickness and can be twisted), and surface characteristics as well as inner structure might influence some of the results (e.g., effect of specular reflection driven by wax at the real needle surface). Yet, before applying the method on real needles to analyze these effects, modification of correction algorithms is recommended.

Inherent angular properties (BRF) of the individual needles are not considered due to the nature of the measuring devices. Therefore, multiple scattering effects are averaged over all needles in the sample and the computed directional-hemispherical reflectance and transmittance factors are averaged values. In this sense our analysis on multiple scattering effects is limited, since no information about the needle scattering phase function can be extracted from these measurements and no separation of specular and diffuse reflectance component of each individual needle is considered. Also, comparing the signal of a set of silicon rhomboidal needles to a flat silicon broad-leaf-like reference is limited by the fact that they have a different

thickness and therefore the transmittance of the rhomboidal needle should not be identical to the one of the flat broad-leaf. The material properties are the same, but the thickness varies across the rhomboidal needles. Based on Beer's law, light transmission decreases exponentially with distance within a homogenous material. The integral of the transmission across the changing thickness would have to be equal to the integral across the same distance of a flat leaf in order to be directly comparable. The use of a set of rhomboidal needles with no gaps in between might be more appropriate as a reference in this situation. However, mean volumes of a sample of squared cross-section needles and a rhomboidal one are equivalent, thus absorption of a rhomboidal needle was assumed comparable to the absorption of a flat silicon broad-leaf one, especially at wavelengths with prevailing light scattering and low absorbance (in our case 500-1700 nm).

The effect of the sample holder was attributed to absorption in the NIR at the entrance of the sample port. Even without a holder, a systematic error in the measurement of transmittance was attributed to this absorption that caused incomplete collection of transmitted light when the sample is placed at some finite distance from the integrating surface (Merzlyak et al. 2002). Nevertheless, it was shown that this effect is not systematic (Gorton et al. 2010). Thus, further investigation will be required to determine the significance of this apparent absorptance.

Due to the limitations of the measuring methods based on the use of integrating spheres with external sample ports, for which only reflectance and transmittance factors can be measured, exploring other measuring alternatives, e.g., measurements of needles at an integrating sphere where the sample is measured inside the sphere, might present bigger potential for a more reliable measurement of scattering and absorption of needles. Nevertheless, this type of sphere is not yet really portable (Chapter 1) and feasibility of needle-leaf optical measurements using current commercial devices (e.g. integrating spheres for Lambda spectrophotometers, PerkinElmer, Inc.) first has to be tested. Since *Mesarch's* method is universal and systematic, developing correction algorithms that include the multiple scattering effects for this method might already allow delivering reliable needle-leaf spectra with enough accuracy for forest remote sensing applications.

At shoot level, it was demonstrated that it is possible to upscale needle to shoot spectral albedo using the relationship between the photon recollision probability (p) and the STAR structural parameter, specially in the VIS and SWIR part of the spectrum. Nevertheless, empirical measurements done in this

thesis are limited to one species (Scots pine), with samples collected from one specific stand, and shoot measurements done on a small number of shoots (10). In addition, the spectral-angular measurements were done only under one illumination angle. Increasing the number of illumination angles, the number of measured samples and the number of species will certainly provide a better proof of this studied relationship and will improve the understanding of shoot scattering properties.

At the top of canopy level, it was shown that for the spatial resolution studied here, PARAS-based estimations of needle-leaf Cab from CHRIS-PROBA data were closer to the validation dataset consisting of a Cab map produced by an artificial neural network (ANN) applied to an image of the studied stand acquired by the airborne AISA sensor. The AISA map was produced following Malenovský et al. (2013), whose results on the Cab estimation from AISA data for the studied area showed that the ANN approach had the best performance (lowest RMSE against ground truth data) when compared to the estimation based on optical indices. However, the airborne Cab map, even though being created at a high spatial resolution of 0.4 m and thus expected to be of a high accuracy, is used for validation by simple averaging of Cab estimates at 0.4 m pixel-size, which is essentially a linear mixing approach. Since the BRDF of a 17 m large CHRIS-PROBA pixel has a spectral character given by a non-linear reflectance mixture of heterogeneous sunlit and shaded surfaces, the resulting Cab estimate may not necessarily fully reassemble the Cab values retrieved and averaged at a high spatial resolution. In addition, the airborne Cab retrieval was carried out only for sunlit pixels of Norway spruce crowns (shaded pixels had a low signal-to-noise ratio that caused an underestimation of retrieved Cab (Malenovský et al. 2013)). Achieving this at the spatial resolution of 0.4 m is feasible, because a single spruce crown is always assembled from several pixels. However, the hypothesis assuming that these spectrally pure sunlit pixels, covering approximately half of the forest canopy, are representative enough to be compared with Cab estimates of a CHRIS-PROBA pixel, which is composed of several spruce crowns, has not been tested yet and would be important in order to improve validation of satellite estimates using airborne products.

6.4 Outlook

Although this thesis addresses specific problematic issues identified as gaps on the interpretation of the RS reflectance signal of coniferous canopies,

further analysis at the specific canopy levels investigated throughout this thesis (i.e. leaf, shoot and canopy) can contribute to expand this field of knowledge. Following this thesis, the following specific research directions have been identified for each canopy level:

At leaf level:

1. Investigation of the potential that integrating spheres with internal sample ports (e.g. integrating spheres for Lambda spectrophotometers, PerkinElmer, Inc.) have on the measurement of needle leaf optical properties might provide more accurate measuring methods in the long run than using single-beam spheres with external ports.
2. In addition, efforts towards the adaptation of available devices such as the spectrogoniophotometer, designed for measuring leaf bidirectional reflectance and transmittance distribution functions (Combes et al. 2007), to non-flat coniferous needles can contribute to improve our knowledge on the scattering phase function of this type of leaves and on the RT modelling in coniferous canopies.

At shoot level:

1. Measurements of more samples and of more coniferous species might improve the applicability of the upscaling approach.
2. Also, it would be interesting to investigate simple parameterizations of shoot scattering phase functions (Möttus et al. 2012).
3. In addition, measurements of clumped structural units at higher within-canopy scales, e.g. branches (as a clump of several shoots), using terrestrial LiDAR (Calders et al. 2013) devices might allow the reconstruction of “real” 3D representations of canopy structural units for which modelling RT might provide a better understanding of the multiple scattering processes driven by the spatial clumping and the opportunity to develop similar simple parameterizations.

At canopy level:

1. Further investigation on the impact of parameterization differences related to the needle optical properties and the implementation of woody elements in each model might contribute to a better Cab retrieval performance.
2. Comparison of Cab estimates at other spatial resolutions might improve the understanding on how the PARAS and DART models differ and what is the applicability of the simpler parameterization provided in PARAS when compared to more detailed models like DART.

3. Improving the validation approach of satellite products with airborne-image data of high spatial resolution. For example, some unmixing approach may be applied to the satellite Cab product pixels previous to the comparison with the validation dataset or maybe some sunlit crown delineation pre-processing may be applied; also using Cab values per crown instead of per pixel for the airborne image, where a crown corresponds to several pixels (i.e. using average Cab per crown), might improve the validation.
4. Use of other inversion approaches for the Cab estimations from both models, e.g., artificial neural networks as in Malenovský et al. (2013) or look-up tables (Darvishzadeh et al. 2008) might lead to better performances by avoiding the sensitivity to LAI changes shown by the optical index ANCB.

References

- Acem, Z., Parent, G., Monod, B., Jeandel, G., & Boulet, P. (2010). Experimental study in the infrared of the radiative properties of pine needles. *Experimental Thermal and Fluid Science*, *34*, 893-899
- ASD, I.S.U.M. (2008). Document 600660 Rev. A. Boulder, CO: ASD Inc.
- Banskota, A., Wynne, R.H., Thomas, V.A., Serbin, S.P., Kayastha, N., Gastellu-Etchegorry, J.P., & Townsend, P.A. (2013). Investigating the utility of wavelet transforms for inverting a 3-D radiative transfer model using hyperspectral data to retrieve forest LAI. *Remote Sensing*, *5*, 2639-2659
- Baranoski, G.V.G. (2006). Modeling the interaction of infrared radiation (750 to 2500 nm) with bifacial and unifacial plant leaves. *Remote Sensing of Environment*, *100*, 335-347
- Baranoski, G.V.G., & Eng, D. (2007). An investigation on sieve and detour effects affecting the interaction of collimated and diffuse infrared radiation (750 to 2500 nm) with plant leaves. *IEEE Transactions on Geoscience and Remote Sensing*, *45*, 2593-2599
- Baranoski, G.V.G., & Rokne, J.G. (2004). *Light Interaction With Plants: A Computer Graphics Perspective*. Chichester, U.K: Horwood
- Baret, F., & Buis, S. (2008). Estimating Canopy Characteristics from Remote Sensing Observations: Review of Methods and Associated Problems. In S. Liang (Ed.), *Advances in Land Remote Sensing* (pp. 173-201): Springer Netherlands
- Baret, F., Weiss, M., Lacaze, R., Camacho, F., Makhmara, H., Pacholczyk, P., & Smets, B. (2013). GEOV1: LAI and FAPAR essential climate variables and FCOVER global time series capitalizing over existing products. Part1: Principles of development and production. *Remote Sensing of Environment*, *137*, 299-309
- Blackburn, G.A. (2007). Hyperspectral remote sensing of plant pigments. *Journal of Experimental Botany*, *58*, 855-867
- Bonan, G.B. (2008). Forests and climate change: Forcings, feedbacks, and the climate benefits of forests. *Science*, *320*, 1444-1449
- Bousquet, L., Lachérade, S., Jacquemoud, S., & Moya, I. (2005). Leaf BRDF measurements and model for specular and diffuse components differentiation. *Remote Sensing of Environment*, *98*, 201-211
- Brodersen, C.R., & Vogelmann, T.C. (2010). Do changes in light direction affect absorption profiles in leaves? *Functional Plant Biology*, *37*, 403-412
- Calders, K., Lewis, P., Disney, M., Verbesselt, J., & Herold, M. (2013). Investigating assumptions of crown archetypes for modelling LiDAR returns. *Remote Sensing of Environment*, *134*, 39-49
- Cescatti, A. (1997). Modelling the radiative transfer in discontinuous canopies of asymmetric crowns. I. Model structure and algorithms. *Ecological Modelling*, *101*, 263-274
- Chen, J.M. (1996). Optically-based methods for measuring seasonal variation of leaf area index in boreal conifer stands. *Agricultural and Forest Meteorology*, *80*, 135-163
- Chen, J.M., & Black, T.A. (1992). Defining leaf area index for non-flat leaves. *Plant, Cell & Environment*, *15*, 421-429
- Chen, J.M., Menges, C.H., & Leblanc, S.G. (2005). Global mapping of foliage clumping index using multi-angular satellite data. *Remote Sensing of Environment*, *97*, 447-457
- Chen, J.M., Mo, G., Pisek, J., Liu, J., Deng, F., Ishizawa, M., & Chan, D. (2012). Effects of foliage clumping on the estimation of global terrestrial gross primary productivity. *Global Biogeochemical Cycles*, *26*
- Chen, M., Schliep, M., Willows, R.D., Cai, Z.L., Neilan, B.A., & Scheer, H. (2010). A red-shifted chlorophyll. *Science*, *329*, 1318-1319
- Cheng, T., Rivard, B., & Sánchez-Azofeifa, A. (2011). Spectroscopic determination of leaf water content using continuous wavelet analysis. *Remote Sensing of Environment*, *115*, 659-670
- Claverie, M., Vermote, E.F., Weiss, M., Baret, F., Hagolle, O., & Demarez, V. (2013). Validation

- of coarse spatial resolution LAI and FAPAR time series over cropland in southwest France. *Remote Sensing of Environment*, 139, 216-230
- Clevers, J.G.P.W., Kooistra, L., & Schaepman, M.E. (2008). Using spectral information from the NIR water absorption features for the retrieval of canopy water content. *International Journal of Applied Earth Observation and Geoinformation*, 10, 388-397
- Colombo, R., Meroni, M., Marchesi, A., Busetto, L., Rossini, M., Giardino, C., & Panigada, C. (2008). Estimation of leaf and canopy water content in poplar plantations by means of hyperspectral indices and inverse modeling. *Remote Sensing of Environment*, 112, 1820-1834
- Combal, B., Baret, F., Weiss, M., Trubuil, A., Macé, D., Pragnère, A., Myneni, R., Knyazikhin, Y., & Wang, L. (2003). Retrieval of canopy biophysical variables from bidirectional reflectance using prior information to solve the ill-posed inverse problem. *Remote Sensing of Environment*, 84, 1-15
- Combes, D., Bousquet, L., Jacquemoud, S., Sinoquet, H., Varlet-Grancher, C., & Moya, I. (2007). A new spectrogoniophotometer to measure leaf spectral and directional optical properties. *Remote Sensing of Environment*, 109, 107-117
- Croft, H., Chen, J.M., Zhang, Y., & Simic, A. (2013). Modelling leaf chlorophyll content in broadleaf and needle leaf canopies from ground, CASI, Landsat TM 5 and MERIS reflectance data. *Remote Sensing of Environment*, 133, 128-140
- Cutter, M.A., Lobb, D.R., & Cockshott, R.A. (2000). Compact High Resolution Imaging Spectrometer (CHRIS). *Acta Astronautica*, 46, 263-268
- Dangel, S., Verstraete, M.M., Schopfer, J., Kneubuehler, M., Schaepman, M., & Itten, K.I. (2005). Toward a direct comparison of field and laboratory goniometer measurements. *IEEE Transactions on Geoscience and Remote Sensing*, 43, 2666-2675
- Darvishzadeh, R., Skidmore, A., Schlerf, M., & Atzberger, C. (2008). Inversion of a radiative transfer model for estimating vegetation LAI and chlorophyll in a heterogeneous grassland. *Remote Sensing of Environment*, 112, 2592-2604
- Daughtry, C.S.T., Biehl, L.L., & Ranson, K.J. (1989). A new technique to measure the spectral properties of conifer needles. *Remote Sensing of Environment*, 27, 81-91
- Dawson, T.P., Curran, P.J., & Plummer, S.E. (1998). LIBERTY - Modeling the effects of Leaf Biochemical Concentration on Reflectance Spectra. *Remote Sensing of Environment*, 65, 50-60
- Demarez, V., & Gastellu-Etchegorry, J.P. (2000). A modeling approach for studying forest chlorophyll content. *Remote Sensing of Environment*, 71, 226-238
- Di Guardo, A., Zaccara, S., Cerabolini, B., Acciarri, M., Terzaghi, G., & Calamari, D. (2003). Conifer needles as passive biomonitors of the spatial and temporal distribution of DDT from a point source. *Chemosphere*, 52, 789-797
- Di Vittorio, A.V. (2009). Enhancing a leaf radiative transfer model to estimate concentrations and in vivo specific absorption coefficients of total carotenoids and chlorophylls a and b from single-needle reflectance and transmittance. *Remote Sensing of Environment*, 113, 1948-1966
- Disney, M., Lewis, P., & Saich, P. (2006). 3D modelling of forest canopy structure for remote sensing simulations in the optical and microwave domains. *Remote Sensing of Environment*, 100, 114-132
- Eng, D., & Baranoski, G.V.G. (2007). The application of photoacoustic absorption spectral data to the modeling of leaf optical properties in the visible range. *IEEE Transactions on Geoscience and Remote Sensing*, 45, 4077-4086
- FAO (2010). Global Forest Resources Assessment 2010: Main Report (p. 378). Rome: Food and Agriculture Organization of the United Nations
- Feret, J., Francois, C., Asner, G., Gitelson, A., Martin, R., Bidet, L., Ustin, S., Lemaire, G., & Jacquemoud, S. (2008). PROSPECT-4 and 5: Advances in the leaf optical properties model separating photosynthetic pigments. *Remote Sensing of Environment*, 112, 3030-3043
- Gamon, J.A., Peñuelas, J., & Field, C.B. (1992). A narrow-waveband spectral index that tracks diurnal changes in photosynthetic efficiency. *Remote Sensing of Environment*, 41, 35-44
- Gastellu-Etchegorry, J.P., Martin, E., & Gascon, F. (2004). DART: A 3D model for simulating satellite images and studying surface radiation budget. *International Journal of Remote Sensing*, 25, 73-96
- Goel, N.S. (1988). Models of vegetation canopy reflectance and their use in estimation of

- biophysical parameters from reflectance data. *Remote Sensing Reviews*, 4, 1-221
- Gorton, H.L., Brodersen, C.R., Williams, W.E., & Vogelmann, T.C. (2010). Measurement of the optical properties of leaves under diffuse light. *Photochemistry and Photobiology*, 86, 1076-1083
- Grant, L. (1987). Diffuse and specular characteristics of leaf reflectance. *Remote Sensing of Environment*, 22, 309-322
- Haboudane, D., Miller, J.R., Tremblay, N., Zarco-Tejada, P.J., & Dextraze, L. (2002). Integrated narrow-band vegetation indices for prediction of crop chlorophyll content for application to precision agriculture. *Remote Sensing of Environment*, 81, 416-426
- Hanrahan, P., & Krueger, W. (1993). Reflection from layered surface due to subsurface scattering. In (pp. 165-174). Anaheim, CA, USA: Publ by ACM
- Hansen, M.C., Potapov, P.V., Moore, R., Hancher, M., Turubanova, S.A., Tyukavina, A., Thau, D., Stehman, S.V., Goetz, S.J., Loveland, T.R., Kommareddy, A., Egorov, A., Chini, L., Justice, C.O., & Townshend, J.R.G. (2013). High-resolution global maps of 21st-century forest cover change. *Science*, 342, 850-853
- Hansen, M.C., Stehman, S.V., & Potapov, P.V. (2010). Quantification of global gross forest cover loss. *Proceedings of the National Academy of Sciences of the United States of America*, 107, 8650-8655
- Hansen, M.C., Stehman, S.V., Potapov, P.V., Loveland, T.R., Townshend, J.R.G., DeFries, R.S., Pittman, K.W., Arunarwati, B., Stolle, F., Steiminger, M.K., Carroll, M., & DiMiceli, C. (2008). Humid tropical forest clearing from 2000 to 2005 quantified by using multitemporal and multiresolution remotely sensed data. *Proceedings of the National Academy of Sciences of the United States of America*, 105, 9439-9444
- Harron, J. (2000). Optical properties of phytoelements in conifers
- Harron, J.W., & Miller, J.R. (1995). An alternate methodology for reflectance and transmittance measurements of conifer needles. In *Proc. Canadian Remote. Sens. Symposium*, 2, 654-661
- Heiskanen, J., Rautiainen, M., Korhonen, L., Mõttus, M., & Stenberg, P. (2011). Retrieval of boreal forest LAI using a forest reflectance model and empirical regressions. *International Journal of Applied Earth Observation and Geoinformation*, 13, 595-606
- Hernandez-Clemente, R., Navarro-Cerrillo, R.M., Suárez, L., Morales, F., & Zarco-Tejada, P.J. (2011). Assessing structural effects on PRI for stress detection in conifer forests. *Remote Sensing of Environment*, 115, 2360-2375
- Hernández-Clemente, R., Navarro-Cerrillo, R.M., & Zarco-Tejada, P.J. (2012). Carotenoid content estimation in a heterogeneous conifer forest using narrow-band indices and PROSPECT+DART simulations. *Remote Sensing of Environment*, 127, 298-315
- Hilker, T., Coops, N.C., Hall, F.G., Andrew Black, T., Chen, B., Krishnan, P., Wulder, M.A., Seilers, P.J., Middleton, E.M., & Huemmrich, K.F. (2008). A modeling approach for upscaling gross ecosystem production to the landscape scale using remote sensing data. *Journal of Geophysical Research G: Biogeosciences*, 113
- Homolová, L., Lukeš, P., Malenovský, Z., Lhotakova, Z., Kaplan, V., & Hanuš, J. (2013). Measurement methods and variability assessment of the Norway spruce total leaf area: Implications for remote sensing. *Trees - Structure and Function*, 27, 111-121
- Hosgood, B., Jacquemoud, S., Andreoli, G., Verdebout, J., Pedrini, G., & Schmuck, G. (1995). Leaf optical properties experiment 93 (LOPEX93). Ispra, Italy: Joint Research Center, European Commission
- Huang, D., Knyazikhin, Y., Dickinson, R.E., Rautiainen, M., Stenberg, P., Disney, M., Lewis, P., Cescatti, A., Tian, Y., Verhoef, W., Martonchik, J.V., & Myneni, R.B. (2007). Canopy spectral invariants for remote sensing and model applications. *Remote Sensing of Environment*, 106, 106-122
- Huang, J.F., & Blackburn, G.A. (2011). Optimizing predictive models for leaf chlorophyll concentration based on continuous wavelet analysis of hyperspectral data. *International Journal of Remote Sensing*, 32, 9375-9396
- IPCC (2007). Climate Change 2007: The Physical Science Basis, Contribution of Working Group I to the Fourth Assessment Report of the Intergovernmental Panel on Climate Change In S. Solomon, D. Qin, M. Manning, Z. Chen, M. Marquis, K.B. Averyt, M. Tignor, & H.L. Miller (Eds.) (p. 996). Cambridge University Press. Cambridge, UK and New York, NY, USA
- Jacquemoud, S., & Baret, F. (1990). PROSPECT: A model of leaf optical properties spectra. *Remote Sensing of Environment*, 34, 75-91

- Jacquemoud, S., & Ustin, S.L. (2001). Leaf optical properties: A state of the art. *Proc. 8th Int. Symp. Phys. Meas. & Signatures Remote Sens.*, 223-332
- Jordan, D.N., & Smith, W.K. (1993). Simulated influence of leaf geometry on sunlight interception and photosynthesis in conifer needles. *Tree Physiology*, 13, 29-39
- Knyazikhin, Y., Martonchik, J.V., Myneni, R.B., Diner, D.J., & Running, S.W. (1998). Synergistic algorithm for estimating vegetation canopy leaf area index and fraction of absorbed photosynthetically active radiation from MODIS and MISR data. *Journal of Geophysical Research D: Atmospheres*, 103, 32257-32275
- Knyazikhin, Y., Schull, M.A., Stenberg, P., Möttus, M., Rautiainen, M., Yang, Y., Marshak, A., Carmona, P.L., Kaufmann, R.K., Lewis, P., Disney, M.I., Vanderbilt, V., Davis, A.B., Baret, F., Jacquemoud, S., Lyapustin, A., & Myneni, R.B. (2013). Hyperspectral remote sensing of foliar nitrogen content. *Proceedings of the National Academy of Sciences of the United States of America*, 110, 811-812+E185-E192
- Knyazikhin, Y., Schull, M.A., Xu, L., Myneni, R.B., & Samanta, A. (2011). Canopy spectral invariants. Part I: A new concept in remote sensing of vegetation. *Journal of Quantitative Spectroscopy and Radiative Transfer*, 112, 727-735
- Kuusk, A., Kuusk, J., & Lang, M. (2009). A dataset for the validation of reflectance models. *Remote Sensing of Environment*, 113, 889-892
- Kuusk, A., & Nilson, T. (2000). A directional multispectral forest reflectance model. *Remote Sensing of Environment*, 72, 244-252
- Kuusk, A., Nilson, T., Kuusk, J., & Lang, M. (2010). Reflectance spectra of RAMI forest stands in Estonia: Simulations and measurements. *Remote Sensing of Environment*, 114, 2962-2969
- Kuusk, A., Nilson, T., Paas, M., Lang, M., & Kuusk, J. (2008). Validation of the forest radiative transfer model FRT. *Remote Sensing of Environment*, 112, 51-58
- Labsphere Application Note 01: Quantitation of single beam substitution correction in reflectance spectroscopy accessories, Labsphere, Inc., North Sutton, NH. [Online]. Available: <http://www.labsphere.com>. Accessed 27 January 2011.
- Lang, A.R.G. (1991). Application of some of Cauchy's theorems to estimation of surface areas of leaves, needles and branches of plants, and light transmittance. *Agricultural and Forest Meteorology*, 55, 191-212
- Laurent, V.C.E., Verhoef, W., Clevers, J.G.P.W., & Schaepman, M.E. (2011a). Estimating forest variables from top-of-atmosphere radiance satellite measurements using coupled radiative transfer models. *Remote Sensing of Environment*, 115, 1043-1052
- Laurent, V.C.E., Verhoef, W., Clevers, J.G.P.W., & Schaepman, M.E. (2011b). Inversion of a coupled canopy-atmosphere model using multi-angular top-of-atmosphere radiance data: A forest case study. *Remote Sensing of Environment*, 115, 2603-2612
- Le Maire, G., François, C., & Dufrène, E. (2004). Towards universal broad leaf chlorophyll indices using PROSPECT simulated database and hyperspectral reflectance measurements. *Remote Sensing of Environment*, 89, 1-28
- Lewis, P., & Disney, M. (2007). Spectral invariants and scattering across multiple scales from within-leaf to canopy. *Remote Sensing of Environment*, 109, 196-206
- Liang, S. (2004). *Quantitative Remote Sensing of Land Surfaces*. Hoboken, NJ: John Wiley & Sons, Inc.
- Lichtenthaler, H.K. (1987). Chlorophylls and carotenoids: Pigments of photosynthetic biomembranes. *Methods in Enzymology*, 148, 350-382
- Lukeš, P., Rautiainen, M., Stenberg, P., & Malenovský, Z. (2011). Empirical test of the spectral invariants theory using imaging spectroscopy data from a coniferous forest. *International Journal of Applied Earth Observation and Geoinformation*, 13, 668-675
- Main-Knom, M., Cohen, W.B., Kennedy, R.E., Grodzki, W., Pflugmacher, D., Griffiths, P., & Hostert, P. (2013). Monitoring coniferous forest biomass change using a Landsat trajectory-based approach. *Remote Sensing of Environment*, 139, 277-290
- Malenovský, Z., Albrechtová, J., Lhotáková, Z., Zurita-Milla, R., Clevers, J.G.P.W., Schaepman, M.E., & Cudlín, P. (2006a). Applicability of the PROSPECT model for Norway spruce needles. *International Journal of Remote Sensing*, 27, 5315-5340
- Malenovský, Z., Homolová, L., Zurita-Milla, R., Lukeš, P., Kaplan, V., Hanuš, J., Gastellu-Etchegorry, J.P., & Schaepman, M.E. (2013). Retrieval of spruce leaf chlorophyll content from airborne image data using continuum

- removal and radiative transfer. *Remote Sensing of Environment*, 131, 85-102
- Malenovský, Z., Martin, E., Homolová, L., Gastellu-Etchegorry, J.P., Zurita-Milla, R., Schaepman, M.E., Pokorný, R., Clevers, J.G.P.W., & Cudlín, P. (2008). Influence of woody elements of a Norway spruce canopy on nadir reflectance simulated by the DART model at very high spatial resolution. *Remote Sensing of Environment*, 112, 1-18
- Malenovský, Z., Ufer, C.M., Clevers, J.G.P.W., Schaepman, M.E., Albrechtová, J., & Cudlín, P. (2006b). A new hyperspectral index for chlorophyll estimation of a forest canopy: Area under curve Normalized to Maximal Band depth between 650-725 nm. In (pp. 161-172): EARSeL eProceedings
- Manninen, T., & Stenberg, P. (2009). Simulation of the effect of snow covered forest floor on the total forest albedo. *Agricultural and Forest Meteorology*, 149, 303-319
- Marshak, A.L. (1989). The effect of the hot spot on the transport equation in plant canopies. *Journal of Quantitative Spectroscopy and Radiative Transfer*, 42, 615-630
- Medlyn, B.E. (1998). Physiological basis of the light use efficiency model. *Tree Physiology*, 18, 167-176
- Melillo, J.M., McGuire, A.D., Kicklighter, D.W., Moore III, B., Vorosmarty, C.J., & Schloss, A.L. (1993). Global climate change and terrestrial net primary production. *Nature*, 363, 234-240
- Merzlyak, M.N., Chivkunova, O.B., Melø, T.B., & Naqvi, K.R. (2002). Does a leaf absorb radiation in the near infrared (780-900 nm) region? A new approach to quantifying optical reflection, absorption and transmission of leaves. *Photosynthesis Research*, 72, 263-270
- Mesarch, M.A., Walter-Shea, E.A., Asner, G.P., Middleton, E.M., & Chan, S.S. (1999). A revised measurement methodology for conifer needles spectral optical properties: Evaluating the influence of gaps between elements. *Remote Sensing of Environment*, 68, 177-192
- Middleton, E.M., Chan, S.S., Mesarch, M.A., & Walter-Shea, E.A. (1996). Revised measurement methodology for spectral optical properties of conifer needles, 2, 1005-1009
- Middleton, E.M., Chan, S.S., Rusin, R.J., & Mitchell, S.K. (1997a). Optical properties of black spruce and jack pine needles at BOREAS sites in Saskatchewan, Canada. *Canadian Journal of Remote Sensing*, 23, 108-119
- Middleton, E.M., Sullivan, J.H., Bovard, B.D., Deluca, A.J., Chan, S.S., & Cannon, T.A. (1997b). Seasonal variability in foliar characteristics and physiology for boreal forest species at the five Saskatchewan tower sites during the 1994 Boreal Ecosystem-Atmosphere Study. *Journal of Geophysical Research D: Atmospheres*, 102, 28831-28844
- Middleton, E.M., Walter-Shea, E.A., Mesarch, M.A., Chan, S.S., & Rusin, R.J. (1998). Optical Properties of Canopy Elements in Black Spruce, Jack Pine and Aspen Stands in Saskatchewan, Canada. *Canadian Journal of Remote Sensing*, 24, 169-186
- Moorthy, I., Miller, J., & Noland, T. (2008). Estimating chlorophyll concentration in conifer needles with hyperspectral data: An assessment at the needle and canopy level. *Remote Sensing of Environment*, 112, 2824-2838
- Moorthy, I., Miller, J.R., Zarco-Tejada, P.J., & Noland, T.L. (2003). Needle Chlorophyll Content Estimation: A Comparative Study of PROSPECT and LIBERTY. In, *International Geoscience and Remote Sensing Symposium (IGARSS)* (pp. 1676-1678)
- Möttus, M. (2007). Photon recollision probability in discrete crown canopies. *Remote Sensing of Environment*, 110, 176-185
- Möttus, M., & Rautiainen, M. (2013). Scaling PRI between coniferous canopy structures. *IEEE Journal of Selected Topics in Applied Earth Observations and Remote Sensing*, 6, 708-714
- Möttus, M., Rautiainen, M., & Schaepman, M.E. (2012). Shoot scattering phase function for Scots pine and its effect on canopy reflectance. *Agricultural and Forest Meteorology*, 154-155, X67-74
- Möttus, M., & Stenberg, P. (2008). A simple parameterization of canopy reflectance using photon recollision probability. *Remote Sensing of Environment*, 112, 1545-1551
- Myneni, R.B., Hoffman, S., Knyazikhin, Y., Privette, J.L., Glassy, J., Tian, Y., Wang, Y., Song, X., Zhang, Y., Smith, G.R., Lotsch, A., Friedl, M., Morisette, J.T., Votava, P., Nemani, R.R., & Running, S.W. (2002). Global products of vegetation leaf area and fraction absorbed PAR from year one of MODIS data. *Remote Sensing of Environment*, 83, 214-231
- Myneni, R.B., Maggion, S., Iaquina, J., Privette, J.L., Gobron, N., Pinty, B., Kimes, D.S., Verstraete, M.M., & Williams, D.L. (1995). Optical remote sensing of vegetation:

- Modeling, caveats, and algorithms. *Remote Sensing of Environment*, 51, 169-188
- Myneni, R.B., & Ross, J. (1991). *Photon-vegetation interactions : applications in optical remote sensing and plant ecology*. Berlin: Springer-Verlag
- Nicodemus, F.E. (1965). Directional Reflectance and Emissivity of an Opaque Surface. *Applied Optics*, 4, 767-773
- Niinemets, U., Ellsworth, D.S., Lukjanova, A., & Tobias, M. (2001). Site fertility and the morphological and photosynthetic acclimation of *Pinus sylvestris* needles to light. *Tree Physiology*, 21, 1231-1244
- Nilson, T. (1971). A theoretical analysis of the frequency of gaps in plant stands. *Agricultural Meteorology*, 8, 25-38
- Nilson, T. (1999). Inversion of gap frequency data in forest stands. *Agricultural and Forest Meteorology*, 98-99, 437-448
- Nilson, T., & Ross, J. (1997). Modeling radiative transfer through forest canopies: implications for canopy photosynthesis and remote sensing. In H.L. Gholz, K. Nakane, & H. Shimoda (Eds.), *The use of remote sensing in the modeling of forest productivity* (pp. 23-60). Dordrecht, The Netherlands: Kluwer Academic Publishing
- Nilsson, A.M., Jonsson, A., Jonsson, J.C., & Roos, A. (2011). Method for more accurate transmittance measurements of low-angle scattering samples using an integrating sphere with an entry port beam diffuser. *Appl. Opt.*, 50, 999-1006
- Noble, S.D., & Crowe, T.G. (2007). Sample holder and methodology for measuring the reflectance and transmittance of narrow-leaf samples. *Applied Optics*, 46, 4968-4976
- Norman, J.M., & Jarvis, P.G. (1975). Photosynthesis in Sitka Spruce (*Picea sitchensis* (Bong.) Carr.): V. Radiation Penetration Theory and a Test Case. *Journal of Applied Ecology*, 12, 839-878
- Oker-blom, P., & Kellomaki, S. (1983). Effect of grouping of foliage on the within-stand and within-crown light regime: Comparison of random and grouping canopy models. *Agricultural Meteorology*, 28, 143-155
- Oker-Blom, P., & Smolander, H. (1988). The ratio of shoot silhouette area to total needle area in Scots pine. *Forest Science*, 34, 894-906
- Panferov, O., Knyazikhin, Y., Myneni, R.B., Szarzynski, J., Engwald, S., Schnitzler, K.G., & Gravenhorst, G. (2001). The role of canopy structure in the spectral variation of transmission and absorption of solar radiation in vegetation canopies. *IEEE Transactions on Geoscience and Remote Sensing*, 39, 241-253
- Pinty, B., & Verstraete, M.M. (1992). On the design and validation of surface bidirectional reflectance and albedo models. *Remote Sensing of Environment*, 41, 155-167
- Pisek, J., Sonnentag, O., Richardson, A.D., & Möttus, M. (2013). Is the spherical leaf inclination angle distribution a valid assumption for temperate and boreal broadleaf tree species? *Agricultural and Forest Meteorology*, 169, 186-194
- Pokorný, R., & Marek, M.V. (2000). Test of accuracy of LAI estimation by LAI-2000 under artificially changed leaf to wood area proportions. *Biologia Plantarum*, 43, 537-544
- Pokorný, R., & Tomášková, I. (2007). Allometric relationships for surface area and dry mass of young Norway spruce aboveground organs. *Journal of Forest Science*, 53, 548-554
- Pokorný, R., Tomášková, I., & Havrankova, K. (2008). Temporal variation and efficiency of leaf area index in young mountain Norway spruce stand. *European Journal of Forest Research*, 127, 359-367
- Rabinowitch, E.I. (1951). *Photosynthesis and Related Processes, Vol. II. Part I. Spectroscopy and Fluorescence of Photosynthetic Pigments*. New York: Interscience
- Ramsey III, E.W., & Rangoonwala, A. (2004). Remote sensing and the optical properties of the narrow cylindrical leaves of *Juncus roemerianus*. *IEEE Transactions on Geoscience and Remote Sensing*, 42, 1064-1075
- Rautiainen, M., Möttus, M., & Stenberg, P. (2009). On the relationship of canopy LAI and photon recollision probability in boreal forests. *Remote Sensing of Environment*, 113, 458-461
- Rautiainen, M., Möttus, M., Yáñez-Rausell, L., Homolová, L., Malenovský, Z., & Schaepman, M.E. (2012). A note on upscaling coniferous needle spectra to shoot spectral albedo. *Remote Sensing of Environment*, 117, 469-474
- Rautiainen, M., & Stenberg, P. (2005). Application of photon recollision probability in coniferous canopy reflectance simulations. *Remote Sensing of Environment*, 96, 98-107
- Rautiainen, M., Stenberg, P., & Nilson, T. (2005). Estimating canopy cover in scots pine stands. *Silva Fennica*, 39, 137-142

- Rautiainen, M., Stenberg, P., Nilson, T., & Kuusk, A. (2004). The effect of crown shape on the reflectance of coniferous stands. *Remote Sensing of Environment*, 89, 41-52
- Rautiainen, M., Suomalainen, J., Möttöus, M., Stenberg, P., Voipio, P., Peltoniemi, J., & Manninen, T. (2007). Coupling forest canopy and understory reflectance in the Arctic latitudes of Finland. *Remote Sensing of Environment*, 110, 332-343
- Richter, T., & Fukshansky, L. (1996a). Optics of a bifacial leaf: 1. A novel combined procedure for deriving the optical parameters. *Photochemistry and Photobiology*, 63, 507-516
- Richter, T., & Fukshansky, L. (1996b). Optics of a bifacial leaf: 2. Light regime as affected by the leaf structure and the light source. *Photochemistry and Photobiology*, 63, 517-527
- Rochdi, N., Fernandes, R., & Chelle, M. (2006). An assessment of needles clumping within shoots when modeling radiative transfer within homogeneous canopies. *Remote Sensing of Environment*, 102, 116-134
- Ross, J. (1981). *The Radiation Regime and Architecture of Plant Stands*. The Hague: Junk Publishers
- Ross, J., Meinander, O., & Sulev, M. (1994). Spectral scattering properties of Scots pine shoots. In *International Geoscience and Remote Sensing Symposium (IGARSS)* (pp. 1451-1454). Pasadena, CA, USA: IEEE
- Sabine, C.L. (2004). *The Global Carbon Cycle: Integrating Humans, Climate, and the Natural World*. Washington, DC: C. B. Field, M. R. Raupach, Eds, Island Press
- Schaepman, M.E., Ustin, S.L., Plaza, A.J., Painter, T.H., Verrelst, J., & Liang, S. (2009). Earth system science related imaging spectroscopy-An assessment. *Remote Sensing of Environment*, 113, S123-S137
- Schaepman-Strub, G., Schaepman, M.E., Painter, T.H., Dangel, S., & Martonchik, J.V. (2006). Reflectance quantities in optical remote sensing-definitions and case studies. *Remote Sensing of Environment*, 103, 27-42
- Sexton, J.O., Song, X.-P., Feng, M., Noojipady, P., Anand, A., Huang, C., Kim, D.-H., Collins, K.M., Channan, S., DiMiceli, C., & Townshend, J.R. (2013). Global, 30-m resolution continuous fields of tree cover: Landsat-based rescaling of MODIS vegetation continuous fields with lidar-based estimates of error. *International Journal of Digital Earth*, 6, 427-448
- Smolander, S., & Stenberg, P. (2003). A method to account for shoot scale clumping in coniferous canopy reflectance models. *Remote Sensing of Environment*, 88, 363-373
- Smolander, S., & Stenberg, P. (2005). Simple parameterizations of the radiation budget of uniform broadleaved and coniferous canopies. *Remote Sensing of Environment*, 94, 355-363
- Sprugel, D.G., Brooks, J.R., & Hinckley, T.M. (1996). Effects of light on shoot geometry and needle morphology in *Abies amabilis*. *Tree Physiology*, 16, 91-98
- Stenberg, P. (1996a). Correcting LAI-2000 estimates for the clumping of needles in shoots of conifers. *Agricultural and Forest Meteorology*, 79, 1-8
- Stenberg, P. (1996b). Simulations of the effects of shoot structure and orientation on vertical gradients in intercepted light by conifer canopies. *Tree Physiology*, 16, 99-108
- Stenberg, P. (2006). A note on the G-function for needle leaf canopies. *Agricultural and Forest Meteorology*, 136, 76-79
- Stenberg, P., Linder, S., & Smolander, H. (1995). Variation in the ratio of shoot silhouette area to needle area in fertilized and unfertilized Norway spruce trees. *Tree Physiology*, 15, 705-712
- Stenberg, P., Linder, S., Smolander, H., & Flower-Ellis, J. (1994). Performance of the LAI-2000 plant canopy analyzer in estimating leaf area index of some Scots pine stands. *Tree Physiology*, 14, 981-995
- Stenberg, P., Lukeš, P., Rautiainen, M., & Manninen, T. (2013). A new approach for simulating forest albedo based on spectral invariants. *Remote Sensing of Environment*, 137, 12-16
- Stenberg, P., Möttöus, M., & Rautiainen, M. (2008). Modeling the Spectral Signature of Forests: Application of Remote Sensing Models to Coniferous Canopies. In S. Liang (Ed.), *Advances in Land Remote Sensing* (pp. 147-171): Springer Netherlands
- Stenberg, P., Palmroth, S., Bond, B.J., Sprugel, D.G., & Smolander, H. (2001). Shoot structure and photosynthetic efficiency along the light gradient in a Scots pine canopy. *Tree Physiology*, 21, 805-814
- Suárez, L., Hueni, A., Kneubuehler, M., Schaepman, M.E., D'Odorico, P., & Schwarz, C. (2011). D 5.5 Calibration final report. In *Hyper-I-Net Deliverables Report. Project Mrtm-Ct-2006-035927* (p. 30)

- Tirén, L. (1926). Om barrytans storlek hos tallbestånd. *Medd. Statens Skogsförskningsinst.*, 23, 295–336
- Ustin, S.L., Gitelson, A.A., Jacquemoud, S., Schaepman, M., Asner, G.P., Gamon, J.A., & Zarco-Tejada, P. (2009). Retrieval of foliar information about plant pigment systems from high resolution spectroscopy. *Remote Sensing of Environment*, 113, S67-S77
- Ustin, S.L., Jacquemoud, S., & Govaerts, Y. (2001). Simulation of photon transport in a three-dimensional leaf: Implications for photosynthesis. *Plant, Cell and Environment*, 24, 1095-1103
- Verrelst, J., Schaepman, M.E., Koetz, B., & Kneubühler, M. (2008). Angular sensitivity analysis of vegetation indices derived from CHRIS/PROBA data. *Remote Sensing of Environment*, 112, 2341-2353
- Vogelmann, T.C. (1993). Plant tissue optics. *Annual Review of Plant Physiology and Plant Molecular Biology*, 44, 231-251
- Watson, D.J. (1947). Comparative physiological studies on the growth of field crops: I. Variation in net assimilation rate and leaf area between species and varieties, and within and between years. *Annals of Botany*, 11, 41-76
- Widłowski, J.L., Taberner, M., Pinty, B., Bruniquel-Pinel, V., Disney, M., Fernandes, R., Gastellu-Etchegorry, J.P., Gobron, N., Kuusk, A., Lavergne, T., Leblanc, S., Lewis, P.E., Martin, E., Möttus, M., North, P.R.J., Qin, W., Robustelli, M., Rochdi, N., Ruiloba, R., Soler, C., Thompson, R., Verhoef, W., Verstraete, M.M., & Xie, D. (2007). Third Radiation Transfer Model Intercomparison (RAMI) exercise: Documenting progress in canopy reflectance models. *Journal of Geophysical Research D: Atmospheres*, 112
- Willmott, C.J. (1981). On the validation of models. *Physical Geography*, 2, 184-194
- Woolley, J.T. (1971). Reflectance and Transmittance of Light by Leaves. *Plant Physiology*, 47, 656-662
- Woolley, J.T. (1973). Change of leaf dimensions and air volume with change in water content. *Plant Physiology*, 41, 815–816
- Wright, P., Bergin, M., Dibb, J., Lefer, B., Domine, F., Carman, T., Carmagnola, C., Dumont, M., Courville, Z., Schaaf, C., & Wang, Z. (2014). Comparing MODIS daily snow albedo to spectral albedo field measurements in Central Greenland. *Remote Sensing of Environment*, 140, 118-129
- Yáñez-Rausell, L., Malenovský, Z., Clevers, J.G.P.W., & Schaepman, M.E. (2014a). Minimizing Measurement Uncertainties of Coniferous Needle-Leaf Optical Properties, Part II: Experimental set-up and error analysis. *IEEE Journal of Selected Topics in Applied Earth Observation and Remote Sensing*, 7, 406-420
- Yáñez-Rausell, L., Schaepman, M.E., Clevers, J.G.P.W., & Malenovský, Z. (2014b). Minimizing Measurement Uncertainties of Coniferous Needle-Leaf Optical Properties, Part I: Methodological Review. *IEEE Journal of Selected Topics in Applied Earth Observation and Remote Sensing*, 7, 399-405
- Zarco-Tejada, P.J., Gonzalez-Dugo, V., Williams, L.E., Suarez, L., Berni, J.A.J., Goldammer, D., & Fereres, E. (2013). A PRI-based water stress index combining structural and chlorophyll effects: Assessment using diurnal narrow-band airborne imagery and the CWSI thermal index. *Remote Sensing of Environment*, 138, 38-50
- Zarco-Tejada, P.J., Miller, J.R., Harron, J., Hu, B., Noland, T.L., Goel, N., Mohammed, G.H., & Sampson, P. (2004). Needle chlorophyll content estimation through model inversion using hyperspectral data from boreal conifer forest canopies. *Remote Sensing of Environment*, 89, 189-199
- Zhang, Y., Chen, J.M., Miller, J.R., & Noland, T.L. (2008a). Leaf chlorophyll content retrieval from airborne hyperspectral remote sensing imagery. *Remote Sensing of Environment*, 112, 3234-3247
- Zhang, Y., Chen, J.M., Miller, J.R., & Noland, T.L. (2008b). Retrieving chlorophyll content in conifer needles from hyperspectral measurements. *Canadian Journal of Remote Sensing*, 34, 296-310
- Zhu, Z., Bi, J., Pan, Y., Ganguly, S., Anav, A., Xu, L., Samanta, A., Piao, S., Nemani, R.R., & Myneni, R.B. (2013). Global data sets of vegetation leaf area index (LAI)3g and fraction of photosynthetically active radiation (FPAR)3g derived from global inventory modeling and mapping studies (GIMMS) normalized difference vegetation index (NDVI3G) for the period 1981 to 2011. *Remote Sensing*, 5, 927-948

Summary

Coniferous forests are important in the regulation of the Earth's climate and thus continuous monitoring of these ecosystems is crucial to better understand potential responses to climate change. Optical remote sensing (RS) provides powerful methods for the estimation of essential climate variables and for global forest monitoring. However, coniferous forests represent challenging targets for RS methods, mainly due to structural features specific for coniferous trees (e.g. narrow needle leaves, shoot clumping) whose effects on the RS signal are not yet known or not yet fully understood.

Recognizing the need for a better adaptation of RS methods to such spatially heterogeneous and structurally complex canopies, this thesis contributes to improving the interpretation of the remotely sensed optical signal reflected from coniferous stands by focusing on specific knowledge gaps identified in the RS methods at different scales of the coniferous canopies. In addition, it explores the application of approaches that simplify the way the structural complexity of such an environment is tackled when using canopy-level radiative transfer approaches. Three main levels based on the identified gaps were defined for the analysis: (needle) leaf level (chapter 2 and 3); shoot level (chapter 4) and canopy level (chapter 5).

At leaf level this thesis contributes to minimizing the uncertainties and errors related to leaf optical measuring methods adapted for needle leaves. Although optical properties of coniferous leaves are extensively used in RS approaches (i.e. as input or as validation data), there is only a limited number of techniques available for measuring coniferous leaves. The first focus of this thesis was to review the shortcomings and uncertainties of such methods in order to identify application limits and potential improvements (chapter 2). A review showed that a more standardized measuring protocol was needed, for which measurement uncertainties and errors had to be identified, quantified and preferably removed or minimized. Thus, an experimental set-up improving the original method of Mesarch et al. (1999) was presented (chapter 3), which focused on analyzing uncertainties caused by the presence of the sample holder and by the multiple scattering triggered by both the shape of the specific needle cross-section, and the distance between the needles composing a sample. Results showed that both the sample holder and the multiple scattering, triggered specially by the shape of the non-flat cross section of the

coniferous needle-leaves, had a non-negligible effect on the optical signal when measured using a standard spectroradiometer coupled to a single-beam integrating sphere and following the method suggested by *Mesarch*. Thus, approaches designed to measure optical properties of non-flat coniferous needle samples more comprehensively should take into account these effects in their current signal correction algorithms.

Needle clumping into shoots quickly transforms the optical signal making the description of the canopy radiative transfer a complex task and encouraging the search for simplified yet robust approaches. Thus, subsequent steps in this thesis focus on one such simplified approach, known as the recollision probability theory (“p-theory”), applied at two hierarchical levels, i.e., shoots (Chapter 4) and the whole canopy (Chapter 5). *At shoot level*, an empirical verification of the relationship between the photon recollision probability and a structural parameter called STAR was investigated. The approach allows upscaling needle albedo to shoot albedo and was previously theoretically tested only (chapter 4). For this analysis empirical optical measurements of Scots pine needles and shoots were used. Results showed that the approach works well for the VIS and SWIR spectral regions. However, it was less accurate for the NIR and also for sparse shoots (STAR <0.15) with an uneven distribution of photon–needle interactions and a larger influence of the twig bark.

Finally, accurate modelling of the reflectance signal at *canopy level* for coniferous canopies requires realistic representations of the forest stands, which in general implies a large number of input parameters and computationally demanding algorithms. Radiative transfer modelling based on the photon recollision probability offers an alternative for a simplified definition of the forest canopy structure. The performance of such approach for estimation of the leaf chlorophyll content from satellite imaging spectroscopy data acquired by the CHRIS-PROBA sensor was investigated. The approach was compared to a computationally more demanding one based on a detailed 3D structural description of a forest (chapter 5). For this purpose two canopy models, PARAS and DART, representing the first and second approach respectively, were used. Top-of-canopy bidirectional reflectance factors (BRF) were simulated for both models and used to calculate two optical indices, ANCB_{670–720} and ANMB_{670–720}. Subsequently, the empirical relationships established between the optical indices and the needle-leaf chlorophyll content (Cab) were applied to the CHRIS-PROBA image of a Norway spruce forest stand to retrieve a map of Cab estimates. Results

showed that for the spatial resolution of CHRIS-PROBA (17 m), the simpler model PARAS can be applied to retrieve plausible needle-leaf Cab estimates from satellite imaging spectroscopy data with less intensive model parameterization and reduced computational power than when using a model like DART. The $ANMB_{670-720}$ optical index was more robust and resulted in a linear relationship between the Cab estimated by both models. This relationship showed, however, a systematic offset that is potentially caused by differences in the implementation of woody elements in each model or by a different parameterization of leaf optical properties. Thus, further investigation on the impact of parameterization differences related to the needle optical properties and the implementation of woody elements in such a model is recommended.

Samenvatting

Naaldbossen zijn belangrijk in de regulatie van het klimaat op aarde en dus is continue monitoring van deze ecosystemen van cruciaal belang om mogelijke reacties op klimaatverandering beter te begrijpen. Optische remote sensing (RS) biedt krachtige methoden voor de schatting van essentiële klimaatvariabelen en voor wereldwijde bosmonitoring. Echter, naaldbossen zijn uitdagende objecten voor RS methoden, voornamelijk als gevolg van structurele kenmerken die specifiek zijn voor naaldbomen (bijv. smalle naalden, clustering binnen loten) waarvan de gevolgen voor het RS-sigitaal nog niet bekend of nog niet volledig begrepen zijn.

Door erkenning van de noodzaak voor een betere aanpassing van RS methoden aan dergelijke ruimtelijk heterogene en structureel complexe vegetatie, draagt dit proefschrift bij aan verbetering van de interpretatie van het optisch RS signaal dat gereflecteerd wordt door opstanden van naaldbomen door middel van het focussen op specifieke kenmerken geïdentificeerd in de RS methoden op verschillende schaalniveaus van de naaldbomen. Bovendien onderzoekt het de toepassing van methoden ter vereenvoudiging van de manier waarop de structurele complexiteit van een dergelijke omgeving wordt aangepakt bij het gebruik van stralingsinteractiemodellen op plantniveau. Drie niveaus werden gedefinieerd voor verdere analyse op basis van de vastgestelde lacunes: (naald-) blad-niveau (hoofdstuk 2 en 3); loot-niveau (hoofdstuk 4) en vegetatie-niveau (hoofdstuk 5).

Op *blad-niveau* draagt dit proefschrift bij aan het minimaliseren van de onzekerheden en fouten door optische meetmethoden voor bladeren aan te passen voor naalden. Hoewel optische eigenschappen van naalden veel worden gebruikt in RS benaderingen (als input of als validatie gegevens), is er slechts een beperkt aantal technieken voor het meten van naalden beschikbaar. Dit proefschrift richt zich in eerste instantie op een review van de tekortkomingen en onzekerheden van dergelijke methoden om de beperkingen voor toepassing en mogelijke verbeteringen te identificeren (hoofdstuk 2). Een review toonde aan dat een meer gestandaardiseerd meetprotocol nodig was, waarvoor meetonzekerheden en -fouten moesten worden geïdentificeerd, gekwantificeerd en bij voorkeur verwijderd of geminimaliseerd. Daarvoor

werd een experimentele opzet gepresenteerd die de oorspronkelijke methode van Mesarch et al. (1999) verbeterde (hoofdstuk 3). Deze opzet was gericht op het analyseren van onzekerheden veroorzaakt door de aanwezigheid van de monsterhouder en de meervoudige verstrooiing veroorzaakt door zowel de vorm van de specifieke naalddoorsnede als de onderlinge afstand tussen de naalden die een monster vormen. De resultaten toonden aan dat zowel de monsterhouder als de meervoudige verstrooiing, speciaal teweeggebracht door de vorm van de niet-vlakke dwarsdoorsnede van de naalden, een niet te verwaarlozen effect had op het optische signaal gemeten met een standaard spectroradiometer gekoppeld aan een laboratorium integrerende bol volgens de methode voorgesteld door Mesarch. Daarom moeten benaderingen, ontwikkeld om optische eigenschappen van monsters met niet-vlakke naalden te meten, beter rekening houden met deze effecten in hun huidige algoritmes voor signaalcorrectie.

Het clusteren van naalden in loten verandert het optische signaal waardoor de beschrijving van de stralingsinteractie in de vegetatie een complexe taak wordt en het onderzoek naar vereenvoudigde maar robuuste benaderingen bevordert. Volgende stappen in dit proefschrift richtten zich vervolgens op een dergelijke vereenvoudigde aanpak, bekend als de zogenaamde “recollision probability theory” (p-theorie), toegepast op twee hiërarchische niveaus: loten (hoofdstuk 4) en de hele vegetatie (hoofdstuk 5). Op *loot-niveau* is een empirische relatie tussen de “photon recollision probability” en een structurele parameter genaamd STAR onderzocht. De aanpak maakt opschaling van naald-albedo naar loot-albedo mogelijk en was tot dusverre alleen theoretisch getest (hoofdstuk 4). Voor deze analyse zijn empirische optische metingen van grove den naalden en loten gebruikt. Resultaten toonden aan dat de aanpak goed werkt voor de VIS en SWIR spectrale gebieden. Het was echter minder nauwkeurig voor het NIR en ook voor ijle loten ($STAR < 0,15$) met een ongelijke verdeling van foton-naald interacties en een grotere invloed van de schors van takken.

Tenslotte vereist nauwkeurige modellering van het reflectiesignaal op *vegetatie-niveau* voor naaldbomen een realistische weergave van de bosopstanden, hetgeen over het algemeen een groot aantal inputparameters en krachtige algoritmen impliceert. Modellering van de stralingsinteractie gebaseerd op de “photon recollision probability” biedt een alternatief met een vereenvoudigde definitie van de structuur van bosopstanden. Het succes van een dergelijke aanpak voor de schatting van het chlorofylgehalte van naalden met behulp van beeldvormende spectroscopie vanuit satellieten

verkregen is onderzocht met de CHRIS-PROBA sensor. Deze aanpak is vergeleken met een aanpak op basis van een gedetailleerde 3D structurele beschrijving van een bos die veel meer rekenkracht vergt (hoofdstuk 5). Hiervoor werden twee reflectiemodellen, PARAS en DART, gebruikt die respectievelijk de eerste en de tweede benadering vertegenwoordigen. Top van de vegetatie (TOC) bidirectionele reflectiefactoren (BRF) werden gesimuleerd voor beide modellen en gebruikt om twee optische indices, $ANCB_{670-720}$ en $ANMB_{670-720}$, te berekenen. Vervolgens werden de empirische relaties gevonden tussen de optische indices en het chlorofylgehalte (Cab) van naalden toegepast op het CHRIS-PROBA beeld van een fijnspar opstand om een kaart met Cab schattingen af te leiden. Resultaten toonden aan dat voor de ruimtelijke resolutie van CHRIS-PROBA (17 m), het eenvoudigere model PARAS kan worden toegepast om aanvaardbare Cab schattingen voor naalden uit beeldvormende spectroscopische satellietgegevens af te leiden met een minder intensieve modelparametrisatie en minder rekenkracht dan bij gebruik van een model zoals DART. De $ANMB_{670-720}$ optische index was robuuster en resulteerde in een lineaire relatie tussen de Cab geschat door beide modellen. Deze relatie vertoonde echter een systematische offset die mogelijk wordt veroorzaakt door verschillen in de implementatie van houtige elementen in elk model of door een andere parametrisering van optische eigenschappen van naalden. Daarom wordt verder onderzoek naar het effect van parametrisatieverschillen met betrekking tot de optische eigenschappen van naalden en de implementatie van houtige elementen in een dergelijk model aanbevolen.

Resumen

Ante la importancia de los bosques de coníferas en la regulación del clima, resulta crucial una continua monitorización de los mismos para entender posibles respuestas al cambio climático. En ese sentido, la teledetección óptica (en inglés *remote sensing*, RS) se muestra como una útil herramienta para la estimación de las variables climáticas esenciales y para la supervisión de las masas forestales mundiales.

Sin embargo, los bosques de coníferas representan un desafío para los métodos de RS, principalmente debido a las características estructurales específicas de los árboles de coníferas –las hojas aciculares y la agrupación de estas en brotes (en inglés *shoots*), cuyos efectos sobre la señal RS aún no se entienden completamente o bien se desconocen.

Pese a la necesidad de lograr una mejor adaptación de los métodos de RS aplicados a los bosques de coníferas, los cuales son espacialmente heterogéneos y estructuralmente complejos, esta tesis contribuye a mejorar la interpretación de la señal óptica de teledetección reflejada desde este tipo de cubiertas forestales, centrándose en lagunas de conocimiento específicas identificadas en los métodos de RS a diferentes escalas de dichas cubiertas. Asimismo, explora la aplicación de estrategias que simplifican la forma en que se aborda la complejidad estructural de tales ambientes dentro del uso de la transferencia radiativa a nivel de copa.

En base a las lagunas identificadas, fueron definidos para el análisis tres niveles principales: nivel de hoja o acícula (capítulos 2 y 3), nivel de brote (capítulo 4) y nivel de cubierta (capítulo 5).

Al *nivel de la hoja* esta tesis contribuye a minimizar las incertidumbres y errores relacionados con los métodos de medición de las propiedades ópticas de las hojas adaptados a hojas aciculares. Aunque las propiedades ópticas de las acículas se utilizan ampliamente en las estrategias de RS (es decir, como *input* o como datos de validación), sólo existe un número limitado de técnicas disponibles para la medición de acículas de coníferas. Por ello, el primer objetivo de esta tesis ha sido revisar las deficiencias e incertidumbres de estos métodos con el fin de identificar los límites de aplicación y las mejoras potenciales (capítulo 2).

Dicha revisión mostró que era necesario un protocolo de medición más estandarizado, para el cual las incertidumbres de medición y los errores tenían que ser identificados, cuantificados y preferiblemente eliminados o minimizados. De acuerdo con estas premisas, se presentó un protocolo experimental (capítulo 3) basado en el método original de Mesarch *et al.* (1999), el cual se centró en el análisis de las incertidumbres causadas por la presencia del soporte de la muestra y por la dispersión múltiple de los fotones provocada tanto por la forma de la sección transversal de la acícula, como por la distancia entre las acículas que componen una muestra.

Los resultados mostraron que tanto el soporte de la muestra como la dispersión múltiple –especialmente la inducida por la sección transversal no plana de las hojas aciculares– tenían un efecto no desdeñable sobre la señal óptica cuando para la medición se utiliza un espectrorradiómetro estándar acoplado a una esfera de integración y se sigue el método sugerido por Mesarch. Por lo tanto, a la hora de corregir la señal óptica de las muestras analizadas, los métodos adaptados a medir las propiedades ópticas de hojas aciculares no planas han de incorporar estos efectos en sus algoritmos.

La agrupación de acículas en brotes transforma rápidamente la señal óptica, lo que conlleva una descripción de la transferencia radiativa de la cubierta forestal muy compleja. Esta situación fomenta la búsqueda de métodos que pese a su rigor presenten una mayor simplicidad. En esta línea, los pasos subsiguientes en esta tesis se centraron en una de dichas estrategias simplificadas –conocida como la teoría de la probabilidad de recesión («*p - theory*»)– aplicadas a dos niveles jerárquicos: el nivel de brote (capítulo 4) y el nivel de cubierta forestal (capítulo 5).

Al *nivel de brote*, se investigó una verificación empírica de la relación entre la probabilidad de recesión y un parámetro estructural llamado STAR. Este método permite determinar el albedo del brote a partir del albedo de la acícula y ha sido únicamente probado a nivel teórico (capítulo 4). Para este análisis se utilizaron las mediciones ópticas empíricas de acículas y brotes de pino silvestre. Los resultados mostraron que el método funciona bien para las regiones espectrales correspondientes al rango del visible (VIS) y del infrarrojo de onda corta (SWIR). Sin embargo, fue menos preciso para el infrarrojo cercano (NIR), así como para brotes con acículas dispersas ($STAR < 0,15$), en los que existe una distribución de las interacciones fotón-acículas desigual y una mayor influencia de la corteza del tallo.

Por último, un modelo preciso de la señal de reflectancia procedente de bosques de coníferas al *nivel de cubierta* requiere representaciones realistas de

la masa forestal objeto de estudio, lo que en general implica un gran número de parámetros de entrada y algoritmos de alta exigencia computacional. Los modelos de transferencia radiativa basados en la probabilidad de recoliación de los fotones ofrecen una alternativa para una definición simplificada de la estructura de la cubierta forestal. Se investigó la actuación de esos modelos a la hora de estimar el contenido de clorofila de las hojas a partir de imágenes hiperespectrales de satélite adquiridas por el sensor CHRIS- PROBA.

Este método se comparó con otro computacionalmente más exigente basado en una descripción tridimensional detallada de la estructura del bosque (capítulo 5). A estos efectos, se utilizaron dos modelos de cubierta, PARAS y DART, que representan el primer y segundo método, respectivamente. Se simularon los factores de reflectancia bidireccional de cubierta (BRF) para ambos modelos y se utilizaron para calcular dos índices ópticos, ANCB₆₇₀₋₇₂₀ y ANMB₆₇₀₋₇₂₀. Posteriormente, las relaciones empíricas establecidas entre los índices ópticos y el contenido de clorofila de hojas aciculares (Cab) fueron aplicadas a la imagen CHRIS- PROBA de un bosque de *Picea abies* para generar un mapa de contenido de clorofila.

Los resultados mostraron que para la resolución espacial de CHRIS- PROBA (17 m), el modelo más simple PARAS se puede utilizar para la estimación del contenido de clorofila en acículas a partir de imágenes hiperespectrales de satélite. Esto supone una parametrización del modelo más sencilla y una menor demanda computacional que cuando se utiliza un modelo como DART.

El índice óptico ANMB₆₇₀₋₇₂₀ resultó ser más riguroso y dio lugar a una relación lineal con la Cab estimada por ambos modelos. Esta relación presentó, sin embargo, una desviación sistemática potencialmente causada por las diferencias en la implementación del efecto de los elementos leñosos en cada modelo o por una parametrización diferente de las propiedades ópticas de las hojas. Por lo tanto, se recomienda una mayor investigación sobre el impacto de las diferencias de parametrización relacionadas con las propiedades ópticas de las acículas y la implementación de los elementos leñosos en dicho modelo.

Acknowledgements

Many people contributed to the successful completion of my PhD thesis. To all of them, I am deeply grateful. First of all I wish to thank my supervisors, each of which contributed in a different and complementary way to make the fulfilment of this project possible. Thanks to Prof. Michael Schaepman and Jan Clevers for giving me this opportunity, for their support and patience, for sharing their experience and showing me how to navigate in the turbulent waters of a PhD, always reminding me the way to the objective and helping me not to lose track of the right direction.

I am sincerely grateful to my daily supervisor, Zbyněk Malenovský, who was always there for me, and whose enthusiasm and patience played a major role on the completion of this work. This PhD thesis is certainly the output of many shared hours of discussions and effort, and would have never been possible without his unlimited availability and support.

The Hyper-spectral Imaging Network (HYPER-I-NET), an FP6 Marie Curie Research Training Network of the European Commission, funded most of this work. I wish to thank the network coordinator Prof. Antonio Plaza (University of Extremadura) and all the members for the valuable scientific and personal experience acquired through my participation in the network.

I wish to thank also my co-authors, Miina Rautiainen and Matti Möttöus. (University of Helsinki), who provided a significant contribution to parts of this thesis and to other scientific discussions that helped me to better understand my work. Thanks also to Petr Lukeš, for his contribution and especially for the shared efforts put on the preparation of the field campaign in the Šumava National Park (Czech Republic) and for the never-ending hours we spent in České Budějovice in the lab measuring our “favourite” needle-leaf optical properties. Many thanks to the rest of the team from Czech Academy that contributed to a successful campaign: Pavel Cudlín, Franta Havlicek, Jan Hanuš, Věros Kaplan, František Zemek, Zuzana Lhotáková and Dan Kováč.

Special thanks also to Lucie Homolová for her valuable teachings on patience on the field of needle optical properties measurements, during our field campaign in the French Alps. This helped me a lot throughout my work with these small elements.

This PhD was the result of several years and places experiences between CGI at Wageningen University (The Netherlands), the Academy of Sciences in

Brno (Czech Republic) and RSL at University of Zurich (Switzerland). I wish to thank all my colleagues and friends in the three locations for the scientific and moral support and for all the shared moments in and outside the office walls: you are a fantastic lot that made this life experience worthy.

In Wageningen, special thanks to Raul, Silvia, Jochem, Roberto, Daniel, Daniela, Rogier, Gerd, Laure, Paulina, Malú, Mónica, Lily, Erica, Danuta, Natalia, Matthijs, Johan and Rink. In Brno, thanks (again) to the remote-sensors Honza, Věros and Franta and special thanks to my housemates and guides on the Czech culture immersion: Lenka, Lucka and Opi. In Zürich, so many grateful thoughts to so many people: Andrés, Livia, Parviz, Reik, Bernardo, Lola, Michi, George, A-K, Somi, Glenda, Arzu, Chris, Marc, Hossein, Santi, Irene. My deep gratitude to the fantastic four PhD “warriors”: Petra, Lucie, Valérie and Titia. Your company have certainly enlightened this not-always-easy path.

From the Spanish side, others, not yet in the list, who never let me walk alone during these years despite the distance: María and Mónica, Álvaro, Enrique, Pepo, Mónica, Guille and Jabi. Thank you all.

Finally, I wish to thank my family, especially my parents Paco and Margarita and my sister Ana, for their unconditional support, confidence and love. The pursuit of this PhD would have never been possible without them. Thanks also to my grandparents, Juan, Julia, Pepe and Margarita, for being the first passing through the taste for education and knowledge. Last but not least, my deepest gratefulness goes to my beloved husband, Regis, for expanding my view on what science means and for being always the bright side of life. Thank you.

Lucía
Rio de Janeiro, 13-12-2013

List of publications

Peer reviewed journals

- Yáñez-Rausell, L.**, Schaepman, M.E., Clevers, J.G.P.W., & Malenovský, Z. (2014). Minimizing measurement uncertainties of coniferous needle-leaf optical properties, part I: methodological review. *IEEE Journal of Selected Topics in Applied Earth Observations and Remote Sensing*, 7, 399-405
- Yáñez-Rausell, L.**, Malenovský, Z., Clevers, J.G.P.W., & Schaepman, M.E., (2014). Minimizing measurement uncertainties of coniferous needle-leaf optical properties, part II: experimental set-up and error analysis. *IEEE Journal of Selected Topics in Applied Earth Observations and Remote Sensing*, 7, 406-420
- Rautiainen, M., Mottus, M., **Yáñez-Rausell, L.**, Homolová, L., Malenovský, Z., & Schaepman, M.E. (2012). A note on upscaling coniferous needle spectra to shoot spectral albedo. *Remote Sensing of Environment*, 117, 469-474
- Yáñez-Rausell, L.**, Malenovský, Z., Rautiainen, M., Clevers, J., Lukeš, P., Hanuš, J., & Schaepman, M.E., (In review). Estimation of spruce needle-leaf chlorophyll content based on DART and PARAS canopy reflectance models. *IEEE Journal of Selected Topics in Applied Earth Observations and Remote Sensing*

Other scientific publications

- Yanez Rausell, L.**, Malenovský, Z., & Schaepman, M.E. (2011). Influence of gap fraction on coniferous needle optical properties measurements. In: 9th Swiss Geoscience Meeting (SGM), Zurich, Switzerland, 11 - 13 November, 2011
- Yanez Rausell, L.**, Malenovský, Z., Clevers, J.G.P.W., & Schaepman, M.E. (2010). Performance of the PROSPECT leaf radiative transfer model version 4 for Norway spruce needles. In: Proceedings Hyperspectral 2010 Workshop (SP-683), Frascati, Italy, 17-19 March 2010

- Yanez, L.**, Homolová, L., Malenovský, Z., Clevers, J.G.P.W., & Schaepman, M.E. (2008). Geometrical and structural parametrization of forest canopy radiative transfer by LIDAR measurements. In: Intl. Archives of Photogrammetry, Remote Sensing and Spatial Information Sciences (ISPRS), Beijing, China, 3 - 11 July 2008
- Malenovský, Z., Homolová, L., Hanus, J., Kaplan, V., Dolansky, T., & **Yanez, L.** (2008). Structural parametrization of Norway spruce trees in radiative transfer of high spatial resolution. In: Proceedings 2nd workshop of the Nordic Network on Physically based remote sensing of forests (PHYSENSE), Helsinki, Finland, 3 - 4 June, 2008

Short biography

Lucía Yáñez Rausell was born in Madrid, Spain, on July 13th, 1979. She attended the neighbourhood primary and High School, *Real Colegio Nuestra Señora del Loreto*, in Madrid. In 1997 she entered the University and started her Forestry engineering degree, a six-years programme at the *ETSI de Montes in Universidad Politécnica de Madrid*.

In 2003, she got an Erasmus grant and went to Wageningen University (WUR) in the Netherlands. There she followed courses on geographic information systems and remote sensing and decided to extend her studies at WUR for one more year to get the credits required for fulfilling the MSc degree in Geo-information and Remote Sensing. In parallel, she was finishing her last year of Forestry Engineering studies in Madrid.

For her MSc. thesis at WUR she was awarded with a Spanish fellowship within the ‘Goya’ programme and stayed for a year (2005-2006) at the German Aerospace Center (DLR) in Oberpfaffenhofen, Munich (Germany). There, she worked with imaging spectroscopy and radiative transfer applied to inland waters monitoring. Peter Gege and Michael Schaepman supervised her MSc. thesis, titled “Investigation of the potential of hyperspectral sensors for bathymetry applications using airborne HyMap data from Lake Constance”.

In July 2006 and after defending her MSc thesis, Lucia went for a 4-month internship to CSIRO in Canberra (ACT, Australia) where she worked for Dr. A. Dekker at the Environmental Remote Sensing Group. Her internship project focused on analysis of water quality in Australian lakes using satellite imagery. After the internship period, she got a contract to work on mapping depth and benthic habitats of a remote coral reef using a semi-analytical inversion/optimization approach and Quickbird data. She worked there until July 2007.

In October 2007, Lucia joined the Hyper-spectral Imaging Network (HYPER-I-NET), an FP6 Marie Curie Research Training Network of the European Commission. Within the HYPER-I-NET project she got the opportunity to undertake her PhD at the Laboratory of Geo-information science and Remote Sensing at Wageningen University (The Netherlands). The outcome of this work is the present PhD thesis.

Besides the attended courses, international conferences, summer schools and field campaigns, during the course of these PhD years, Lucia moved along four countries: The Netherlands, Czech Republic, Switzerland and Brazil. This offered her the great opportunity to get familiar with different cultures and to get to experience working in different environments as well as meeting many people from all over the world.

Lucia’s current research interests are related to remote sensing of vegetation with emphasis on forest environments and physically based approaches.

PE&RC PhD Education Certificate

With the educational activities listed below the PhD candidate has complied with the educational requirements set by the C.T. de Wit Graduate School for Production Ecology and Resource Conservation (PE&RC) which comprises of a minimum total of 32 ECTS (= 22 weeks of activities)

Review of literature (5 ECTS)

- Review on physical remote sensing methods for forest environment

Writing of project proposal (4.5 ECTS)

- Using radiative transfer modelling to bridge scaling gaps in boreal forest (2008)

Post-graduate courses (6.4 ECTS)

- IDL programming; CGI, WUR (2008)
- Fire as a driver of system processes; PE&RC, WUR (2008)
- Advanced statistics; PE&RC, WUR (2008)
- Summer course in computational Geo-Ecology; Amsterdam Graduate School of Science, Vrije Universiteit Amsterdam (2009)

Laboratory training and working visits (4 ECTS)

- Remote sensing of alpine environments, training in field data collection; French National Centre for Scientific Research (CNRS) (2009)
- Training in needle leaf optical properties measurements and remote sensing field campaigns; preparation and participation; Academy of Science of Czech Republic (2009)

Competence strengthening / skills courses (2.7 ECTS)

- Information literacy; WUR Library (2007)
- PhD Competence assessment; WGS, WUR (2008)
- Techniques for writing and presenting a scientific paper; WGS, WUR (2008)
- Presentation skills; WGS, WUR (2009)

PE&RC Annual meetings, seminars and the PE&RC weekend (1.8 ECTS)

- PE&RC Weekend (2008)

- PE&RC Seminar day: farming futures in Sub-Saharan Africa (2008)
- PE&RC Day: expect the unexpected (2008)
- PE&RC Day: scaling from molecules to ecosystems (2008)

Discussion groups / local seminars / other scientific meetings (7.5 ECTS)

- 1st WIMEK Workshop on earth observation and crop growth modelling; CGI, WUR (2007)
- Discussion group Spatial Methods (SPAM) (2007-2009)
- Discussion group ecological theory and application (2007-2009)
- Sensing a changing world workshop; CGI, WUR (2008)
- Remote sensing of environment workshop; CGI, WUR (2009)
- Seminar remote sensing; Institute for Environmental studies, Vrije Universiteit Amsterdam (2009)

International symposia, workshops and conferences (7 ECTS)

- HYPER-I-Net Workshop; oral presentation; Wageningen, NL (2008)
- HYPER-I-Net Workshop; oral presentation; Munich, Germany (2009)
- Hyperspectral Workshop; poster presentation; ESRIN, Frascasti, Italy (2010)
- 9th Swiss Geoscience Meeting; poster presentation; Switzerland (2011)